Dynamic Stall on Vertical Axis Wind Turbine Blades

Thesis by

Reeve Dunne

In Partial Fulfillment of the Requirements

for the Degree of

Doctor of Philosophy

California Institute of Technology

Pasadena, California

2016

(Defended Aug 24, 2015)

Acknowledgments

I would like to first thank my advisor Beverley McKeon for working with and advising me over the past five years. It has been an honor to have spent this time in her group, and I have learned a great deal with her support. Furthermore I'd like to thank the rest of my committee: Tim Colonius, John Dabiri, and Melany Hunt, for reviewing this thesis and providing their insight on my work.

I would also like to thank Morteza Gharib and David Jeon for sharing and providing support for the facility used for this research, as well as Peter Schmid, without whose insight and experience with the dynamic mode decomposition much of this work would not have been possible. While performing this work, I have had the opportunity to collaborate with Hsieh-Chen Tsai, who provided another view of the challenges in this thesis. Additionally I benefited from discussions on vertical axis wind turbines with Daniel Araya, Matthias Kinzel, Julia Cossé and others.

It has been a privilege to work with the students and faculty of both mechanical engineering and GALCIT. I especially want to thank my first year advisor, Guillaume Blanquart, as well as my colleagues in the McKeon group, and everyone who started with me in 2010, notably Esteban Hufstedler for the many conversations we've had that have made their way into this thesis.

To my friends from Caltech to Tufts and from California to Colorado and Massachusetts, I can not thank you enough for your friendship and for listening to stories from my research. All the time I have spent at Caltech in the classroom, laboratory, or on the softball field, or outside biking, hiking, skiing, or sailing, you have made all these years unforgettable. Thank you to Kathleen Keough for her support for this thesis and beyond.

Finally thank you to my family: my mother Diane Dunne, Aunt and Uncle, Monk and Bob Ward. Without your tireless love and support none of this would have been possible.

This study was funded by the Gordon and Betty Moore Foundation through grant GBMF#2645 to the California Institute of Technology.

Abstract

In this study the dynamics of flow over the blades of vertical axis wind turbines was investigated using a simplified periodic motion to uncover the fundamental flow physics and provide insight into the design of more efficient turbines. Time-resolved, two-dimensional velocity measurements were made with particle image velocimetry on a wing undergoing pitching and surging motion to mimic the flow on a turbine blade in a non-rotating frame. Dynamic stall prior to maximum angle of attack and a leading edge vortex development were identified in the phase-averaged flow field and captured by a simple model with five modes, including the first two harmonics of the pitch/surge frequency identified using the dynamic mode decomposition. Analysis of these modes identified vortical structures corresponding to both frequencies that led the separation and reattachment processes, while their phase relationship determined the evolution of the flow.

Detailed analysis of the leading edge vortex found multiple regimes of vortex development coupled to the time-varying flow field on the airfoil. The vortex was shown to grow on the airfoil for four convection times, before shedding and causing dynamic stall in agreement with 'optimal' vortex formation theory. Vortex shedding from the trailing edge was identified from instantaneous velocity fields prior to separation. This shedding was found to be in agreement with classical Strouhal frequency scaling and was removed by phase averaging, which indicates that it is not exactly coupled to the phase of the airfoil motion.

The flow field over an airfoil undergoing solely pitch motion was shown to develop similarly to the pitch/surge motion; however, flow separation took place earlier, corresponding to the earlier formation of the leading edge vortex. A similar reduced-order model to the pitch/surge case was developed, with similar vortical structures leading separation and reattachment; however, the relative phase lead of the separation mode, corresponding to earlier separation, necessitated that a third frequency to be incorporated into the reattachment mode to provide a relative lag in reattachment.

Finally, the results are returned to the rotating frame and the effects of each flow phenomena on the turbine are estimated, suggesting kinematic criteria for the design of improved turbines.

Contents

List of Figures

Nomenclature

t	Time [s]
AR	Aspect ratio
α	Angle of attack [°]
θ	Turbine rotation angle [°]
Re_c	Chord Reynolds number ($\frac{Uc}{\nu}$)
U_∞	Windspeed [m s^{-1}]
U	Effective velocity/Freestream velocity relative to airfoil [m s^{-1}]
$\bar{U}$	Average velocity in experiment (tunnel velocity) [m s^{-1}]
χ	Vorticity [s^{-1}]
η	Tip speed ratio ($\frac{\omega R}{U_\infty}$)
ω	Turbine frequency [rad s^{-1}]
Ω	Pitch/surge frequency [rad s^{-1}]
R	Turbine radius [m]
Ro	Rossby number ($\frac{U_\infty}{2c\omega}$)
c	Chord length [cm]
th	Airfoil thickness [m]
ν	Kinematic viscosity [m^2 s^{-1}]
λ	Transformed DMD eigenvalues [rad s^{-1}]
k	Reduced frequency [$\frac{\Omega c}{2\bar{U}}$]
Γ_1	Vortex center criterion
Γ_2	Vortex boundary criterion
x,u	Streamwise coordinate [c], streamwise velocity [m s^{-1}]
y, v	Cross-stream coordinate [c], cross-stream velocity [m s^{-1}]
z, w	Spanwise coordinate [c], spanwise velocity [m s^{-1}]
x_l	Leading edge position [c]

u_Γ	Vortex circulation [m^2 s^{-1}]
x_v	Vortex x position [c]
$\Delta\alpha$	Pitch amplitude [°]
α_0	Mean angle of attack [°]
α_{ss}	Static stall angle [°]
$\hat{T}$	Formation time/airfoil convection time ($\hat{T} = \int \frac{U}{c} dt$)
F	Frequency [Hz]
St	Strouhal number [$\frac{Fc}{U}$]

subscript

i	Imaginary component
r	Real component
j	Variable index
$\pm$	Pitch up (+) and down (-)

List of Abbreviations

VAWT	Vertical axis wind turbine
HAWT	Horizontal axis wind turbine
DMD	Dynamic mode decomposition
LEV	Leading edge vortex
TEV	Trailing edge vortex
PIV	Particle image velocimetry
EPM	Equivalent planar motion

superscript

C	Computational
E	Experimental

Chapter 1

Introduction

1.1 Motivation

In 2014 the United States produced approximately 4.1 trillion kilowatt-hours of electricity. Sixty-seven percent of this electricity was generated using fossil fuels, predominantly coal and natural gas (US Energy Information Administration, 2015). This produced approximately 2000 metric tons of greenhouse gas emissions (Environmental Protection Agency, 2015). To curtail this greenhouse gas pollution and reduce the dependence on fossil fuels, more renewable energy sources are being utilized. Since 2012, wind energy has been the leading source of new generating capacity in the United States, producing 4.4% of the total production in 2014 (up from 3.6% in 2013) (American Wind Energy Association, 2013; US Energy Information Administration, 2015). Most of this energy is currently produced using large scale horizontal axis wind turbines (HAWTs) that can individually generate over three megawatts of electricity, with blade diameters up to 126m (Vestas, 2015). Individual HAWTs are very efficient, extracting nearly the theoretical Betz limit of 59% of the power of the wind (Vanek and Albright, 2008). The power output from wind farms however is limited by interference between the turbines. Due to this interference turbines must be separated by three to five turbine rotor diameters in the cross stream direction and six to ten diameters downstream to achieve an average of 90% of individual turbine efficiency (Hau, 2013). This restriction limits the power density (defined as power produced per unit of land area) to 2-3W m^{-2} (MacKay, 2009).

Smaller vertical axis wind turbines (VAWTs) with a rated capacity less than 20kW represent an alternative to HAWTs with fewer restrictions on their spacing. Whittlesey et al. (2010) proposed a tight configuration of VAWTs based on the fluid dynamics of fish schooling. They developed a potential flow model, indicating a potential increase in power density due to the decreased turbine spacing. Dabiri (2011) tested this idea, using arrays of six 1.2kW Windspire VAWTs only 10m tall

with a 1.2m diameter, and achieved power densities between 21 and 47W m^{-2}. They postulated that larger arrays could maintain up to 18W m^{-2}, even with the resulting decreased freestream velocity apparent to interior turbines in the larger array. Kinzel et al. (2012) measured the flow field within similar eighteen turbine arrays and demonstrated that flow velocity returned to 95% of upwind velocity within six diameters of a counter-rotating VAWT pair, significantly faster than from behind typical HAWTs. In addition to the lower spacing requirements, VAWTs have the advantages of an insensitivity to wind direction, quieter running conditions due to slower blade motion, and a typically simpler design, resulting in construction with fewer moving parts and a constant blade profile along the span (Greenblatt et al., 2013; Islam et al., 2007). While modern HAWTs can approach theoretical maximum efficiency, the aerodynamics of VAWTs are less well understood, and their individual efficiency suffers, such that even the best VAWT designs are $\geq 10\%$ less efficient than HAWTs (Hau, 2013). Furthermore, this increased aerodynamic complexity increases the dangers of fatigue loading, decreasing the reliability of VAWTs in the field, and causing sometimes catastrophic failure (Dabiri et al., 2015; Cossé, 2014).

This work studies an approximation of the flow experienced by an individual blade of a vertical axis wind turbine as a first step to understanding the complex fluid dynamics that limits the efficacy of current VAWT designs. The variation in flow conditions caused by the rotation of the turbine is decomposed into a time dependent angle of attack and velocity variation. This variation is reproduced in the lab by pitching and surging an airfoil sinusoidally at the same chord Reynolds number, phase, and reduced frequency as a representative VAWT blade introduced in section 1.2.1 in a water tunnel described in Chapter 2. A comparison of the turbine kinematics given by equation 1.1 to the sinusoidal pitch/surge motion used in the experiment is shown in figure 1.1.

$$\alpha = \tan^{-1}\left(\frac{\sin\theta}{\eta + \cos\theta}\right) \tag{1.1a}$$

$$U = U_\infty \sqrt{1 + 2\eta\cos\left(\theta(t)\right) + \eta^2} \tag{1.1b}$$

Pitching and surging motion can capture the angle of attack and velocity variation of the turbine; however, it neglects the the Coriolis effect due to the rotation of the turbine. The Coriolis force imposes a force on the flow to account for the curved path of the turbine blade. The relative importance of this Coriolis force in a VAWT can be measured using the ratio of inertial to rotational forces, the Rossby number ($Ro = \frac{U_\infty}{2*c*\omega}$). Using the definition of the tip speed ratio ($\eta = \frac{\omega R}{U_\infty}$) simplifies the Rossby number to be dependent only on the geometry and operating condition of

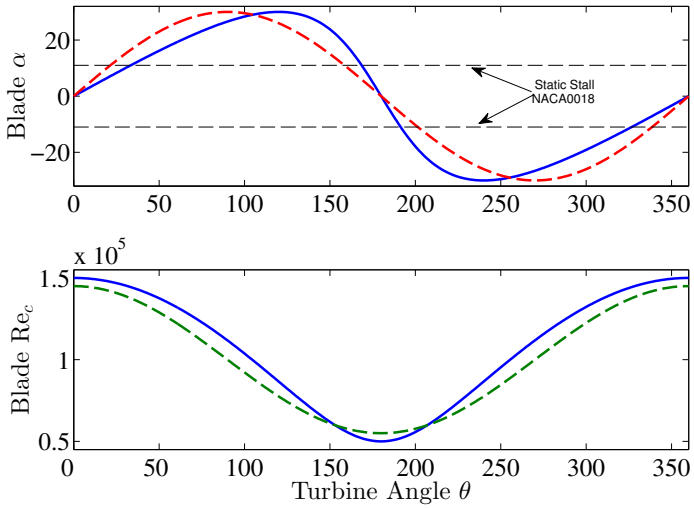

Figure 1.1: Periodic velocity and Reynolds number variation over typical VAWT blade, for $\eta = 2$, $U_\infty = 5\text{m s}^{-1}$, $c = 15\text{cm}$ (solid lines). Compared to test motion (dashed lines).

the turbine, $Ro = \frac{R}{2*c*\eta}$. For a standard industrial turbine at $\eta = 2$, $c = 15\text{cm}$ (Windspire, 2013) the Rossby number is order 1. The effect of the Coriolis force, discussed further in section 1.2.1 and Chapter 6, has been studied by Tsai and Colonius (2014), who demonstrated a similar flow development prior to flow separation with and without the Coriolis force at a much lower Reynolds number.

Unwrapping the rotating trajectory of the turbine blade into the linear pitch/surge reference frame allows for time-resolved velocity measurements to be made with particle image velocimetry (PIV) over the entire pitch/surge period at the expense of neglecting the Coriolis force caused by the rotating reference frame. In a phase-averaged realization of the flow, such time resolved measurements allow the development of structure to be analyzed, and also for time dependent analysis techniques, such as the dynamic mode decomposition discussed below, to be applied. Furthermore, a single experiment encompasses a large portion of the total airfoil motion and, therefore, non-phase-averaged behavior can be investigated. Additionally, removing the rotational component allows for the results developed for this motion to be extended to similar flows involving large dynamic angle of attack and velocity variation. Finally, the pitching and surging motion can be decoupled in these and similar experiments, opening the parameter space in such a way that the phase relationship between these motions can be investigated and potentially modified to develop a motion profile with improved flow characteristics.

1.2 Background

Numerous authors have performed both experimental and computational research on the flow over airfoils, including dynamic and static stall over a wide range of conditions such as Reynolds number, Mach number, airfoil shape, etc. A review of the most applicable work to vertical axis wind turbine flows, focusing on incompressible flow, over simple airfoils is summarized below to provide context for this work.

For the rest of the thesis, streamwise, cross-stream and spanwise directions are denoted by x, y and z, respectively, with associated velocities u, v, and w and spanwise vorticity

$$\chi = \frac{\partial v}{\partial x} - \frac{\partial u}{\partial y}. \tag{1.2}$$

1.2.1 Vertical axis wind turbines

The oldest designs of vertical axis wind turbines are driven purely by drag, similar to cup anemometers used to measure wind velocity. A schematic of a drag based VAWT is shown in figure 1.2. These designs are based on a drag differential between the advancing ($-90° < \theta < 90°$) and retreating ($90° < \theta < 270°$) blades and are limited to a tip speed ratio defined as the blade speed divided by the incoming windspeed, $\eta = \frac{\omega R}{U_\infty} < 1$, where R is the radius of the turbine, U_∞ is the free stream wind velocity, and ω the turbine rotation rate, since the blade velocity cannot exceed that of the wind pushing it. This tip speed ratio limitation decreases the turbine efficiency significantly (Hau, 2013).

Modern VAWTs, for example the 1.2kW Windspire used in experiments by Kinzel et al. (2012), however, are driven by lift and operate at tip speed ratios of between 2 and 3 (Windspire, 2013). Lift-based turbines provide torque to turn the turbine over the entire rotation cycle due to the projection of the lift vector in the direction of turbine rotation. For these turbines, with $\lambda > 1$ the projection of the lift vector always provides positive torque driving the turbine, while drag induces negative torge and slows the turbine down. The projection of lift is most effective at maximum angle of attack, i.e. more of the lift vector is in the direction of rotation. It has been shown, however, that due to the significant decrease in freestream velocity in the downstream half of the turbine ($180° < \theta < 360°$) as a result of the wake of upstream blades and turbine structure, considerable torque is only produced in the upstream half of the cycle ($0° < \theta < 180°$) (Islam et al., 2007). As such the work presented here will focus on the upstream part of the blade trajectory and will not explicitly investigate the effects of the wake on the downstream blades. Islam et al. (2007)

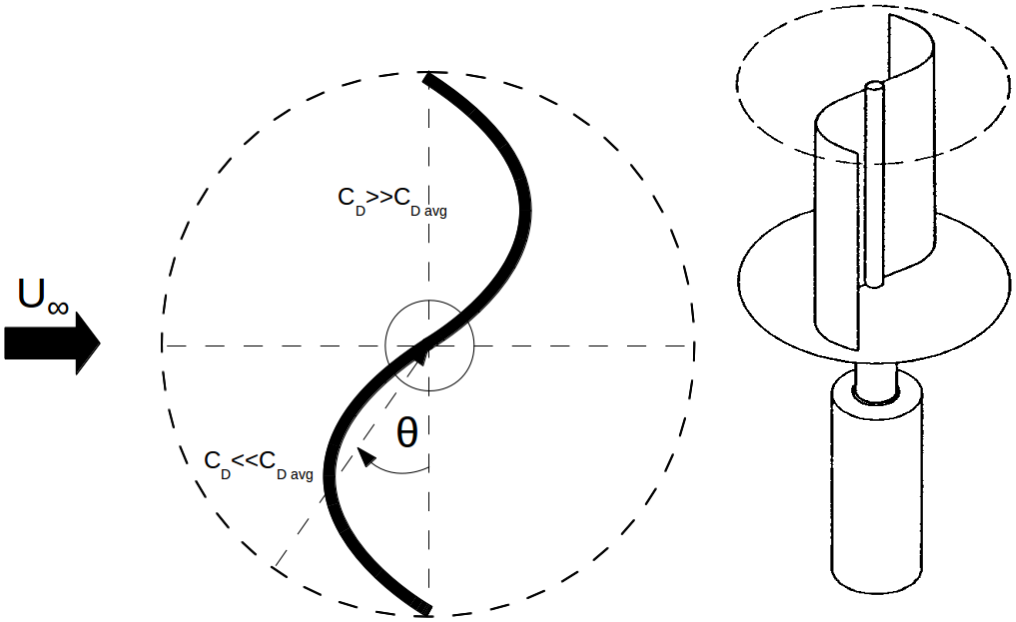

Figure 1.2: Top view schematic of typical drag based VAWT (left). Clockwise rotation is driven by drag coefficient discrepancy between advancing and receding blades. (Right) Isometric view of drag based Savonius turbine from Hau (2013).

investigated the effect of using different airfoils for small straight bladed VAWTs and concluded that due, partially to the difference in velocity in upstream and downstream halves of the turbine, thick, high lift, asymmetrical airfoils are often best suited for VAWTs. Furthermore, Beri and Yao (2011) found that using a cambered airfoil aided in the self-starting ability of the turbines, allowing the turbines to spin at a lower windspeed. A schematic of a typical lift based VAWT is shown in figure 1.3, demonstrating angle of attack α, effective velocity U, and the directions of the typical lift and drag vectors. Only these modern, lift-driven turbines are considered in this study.

Araya and Dabiri (2015) measured the wake of lift driven VAWTs over a range of tip speed ratios and Reynolds numbers. They performed experiments on turbines driven by the flow, with the tip speed ratio controlled by a brake, and/or driven by a motor. They found that the wake was affected most strongly by tip speed ratio η, while Reynolds number had a minor effect. Furthermore, they found that while the wake was changed when the tip speed ratio was driven beyond what it could achieve without a motor, if the tip speed ratio and Reynolds number were kept constant, there was no difference between a flow or motor driven turbine.

Due to the perpendicular incoming flow and turbine rotation axis, a single blade of a VAWT goes through a periodic change in angle of attack and relative velocity during the turbine cycle. At

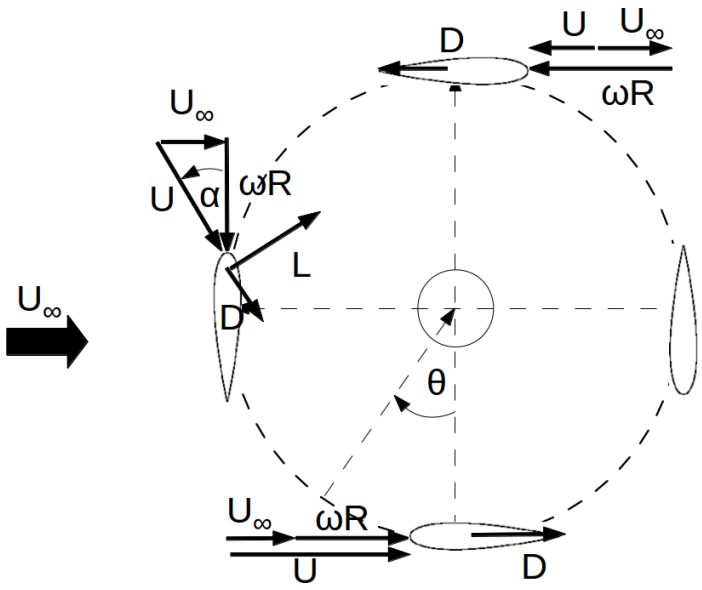

Figure 1.3: Top view of a typical VAWT. Wind speed U_∞, relative velocity U, blade velocity ωR, lift L and drag D, directions. Clockwise rotation is driven by lift on each blade. θ denotes angular location with zero corresponding to maximum relative U and $\alpha = 0°$.

low tip speed ratios this angle of attack variation drives the airfoil well above its static stall angle, resulting in dynamic stall on each blade twice per turbine cycle, once on each side of the blade (figure 1.1). In practical terms dynamic stall causes an abrupt drop in the lift of the blade, and therefore torque on the turbine, as well as potentially damaging unsteady loading on the generator and turbine structure (Greenblatt et al., 2013); error in predicting these dynamic loads can decrease VAWT lifetimes by a factor of up to 70 (Carr, 1988). In addition to dynamic stall, the blade also experiences attached and separated flow during different portions of the rotation cycle. Each of these regimes exerts different forces on the turbine and must be considered in the design of an efficient and robust VAWT.

1.2.2 Dynamic stall

In addition to vertical axis wind turbines, dynamic stall appears in many aspects of unsteady aerodynamics from helicopters to micro air vehicles. In biological and bio-inspired aerodynamics the increased lift production experienced during dynamic stall is critical in achieving flight (Rival et al., 2009), whereas in larger systems such as helicopters the lift variation causes undesirable loading conditions (Greenblatt and Wygnanski, 2001). In order to understand this phenomenon numerous authors have performed both experimental and computational research in dynamic and static stall over a wide range of conditions as well as made efforts to control stall. Here we provide a brief

review of only the most pertinent literature to vertical axis wind turbines.

Dynamic stall is understood to correspond to significant differences in the flow field and forces during pitch-up and pitch-down on an airfoil undergoing unsteady motion. During pitch up, there is significant stall-delay resulting in attached flow, and high lift well beyond the static stall angle α_{ss}. Additionally, during pitch up a leading edge, or dynamic stall vortex, is expected to develop, and subsequently shed from the airfoil, with an associated drop in lift. On pitch down there is a similar delay in the flow reattachment.

In a technical report for NASA, Carr et al. (1977) performed some of the first experiments on dynamic stall on NACA 0012 and other airfoils with a pitch amplitude of $\Delta\alpha \sim 10°$ and mean angle of attack ($\alpha_0 = 15°$). These experiments, performed at Reynolds numbers up to 2.5×10^6, used flow visualization to identify leading edge vortex (LEV) development, growth, and shedding. After sufficient time the LEV was shown to begin to move aft until it reached the airfoil trailing edge, when it was finally shed from the airfoil and convected downstream. Combining these visualizations with force measurements, they were able to show that pitching moment about the quarter-chord decreases substantially when the vortex moves aft, and, finally, when the vortex reaches the trailing edge and sheds the lift stops increasing with increasing angle of attack. These points are defined as 'moment stall' and 'lift stall', respectively, and in this dynamic case do not occur at the same angle of attack as they do on static airfoils.

Particle image velocimetry analysis at $Re = 9 \times 10^5$ was performed by Mulleners and Raffel (2012, 2013) on a cambered airfoil pitching $\Delta\alpha = 6 - 8°$ around a statically attached, but high angle of attack between $\alpha_0 = 18°$ and $\alpha_0 = 22°$ at reduced frequencies between $k = \frac{\omega c}{2\bar{U}} = 0.05 - 0.10$, where c is the airfoil chord, ω is the angular frequency, and $\bar{U}$ is the mean velocity. These experiments highlighted five stages of the flow corresponding to attached flow, stall development, stall onset, stall, and flow reattachment (Mulleners and Raffel, 2012) and identified a 'primary stall vortex' pinched off at the point of dynamic stall (Mulleners and Raffel, 2013). Furthermore, a distinction was made between light and deep dynamic stall, where light stall was characterized by a much smaller separation region. Mulleners and Raffel (2012) show that deep stall was caused when the dynamic stall vortex separated before maximum angle of attack, while light stall occurred when the vortex separated from the airfoil as a result of the change of pitch direction at the maximum angle of attack.

Similar pitching experiments on a flat plate at a lower Reynolds number between $Re = 5 \times 10^3$ and 2×10^4 performed by Baik et al. (2012) showed that the instantaneous angle of attack and

reduced frequency, k, determined flow evolution and that the LEV separation occurred later in the motion period, or at a higher angle of attack, with increased k in agreement with the results of Rival et al. (2009). They showed that leading edge vortex circulation tended to increase linearly with the phase of the airfoil motion, with a faster growth corresponding to a lower reduced frequency k. Baik and Bernal (2012) and Kang et al. (2013) performed experiments and computations on a SD7003 airfoil under similar conditions, demonstrating a phase delay of the dynamic separation on the airfoil when compared to the flat plate due to increased attachment over the smoothed leading edge. Furthermore, the unsteady lift peak was shown to be higher in the flat plate case, while the average lift was increased in the airfoil case due to the flow remaining attached up to a higher angle of attack.

Rival et al. (2009) found that a strong trailing edge vortex (TEV) appears when the LEV sheds and convects past the airfoil at the point of lift stall. The TEV was shown to cause a significant decrease in lift similar to the effects of a starting vortex. This lift deficit remained for a significant portion of the airfoil motion cycle (Rival et al., 2009; Panda and Zaman, 1994). In further work Prangemeier et al. (2010) tested different pitch motions at the bottom of a plunge motion to mitigate the effect of the trailing edge vortex TEV. Using a 'quick pitch' motion, they were able to reduce the TEV circulation by at least 60%.

Choi et al. (2015) investigated surging and plunging airfoils computationally at $Re = 500$ and experimentally at $Re = 5.7 \times 10^4$. In surging experiments they found attenuation or amplification of the unsteady forces, depending on the reduced frequency k of the motion. At $k = 0.7$ the LEV was shed while the airfoil was advancing, increasing the already high lift due to the higher velocity, thus amplifying the unsteady force component. In the $k = 1.2$ case the LEV was shed while the airfoil was retreating and as such, added to the relatively low lift during retreat, decreasing force variation.

In order to reduce the negative effects of dynamic stall; Heine et al. (2013) placed passive disturbance generators near the leading edge of an airfoil pitching $\Delta\alpha = 5°$ and $7°$ about $\alpha_0 = 13°$ and demonstrated a significant decrease in the lift drop after dynamic stall. PIV measurements were used to show that the perturbed airfoil exhibited a smoother stall from the trailing edge forward instead of the abrupt leading edge separation exhibited in classical dynamic stall. Greenblatt and Wygnanski (2001) and Greenblatt et al. (2001) used oscillatory and steady blowing on airfoils at the leading edge, and over a trailing edge flap at high Reynolds number ($Re \geq 3 \times 10^6$) under various unsteady motions. While steady blowing at the leading edge increased unsteadiness and made the lift decrease in stall significantly worse, oscillatory blowing and suction was shown to nearly elimi-

nate the leading edge vortex, removing lift hysteresis and mitigating trailing edge separation, thus increasing overall lift.

Müller-Vahl et al. (2015) used PIV and pressure measurements on a NACA-0018 airfoil pitched about the quarter-chord at $k = 0.074$ to investigate the effect of constant blowing near the leading edge and at half-chord. They found that with sufficient leading edge blowing, the dynamic stall vortex can be eliminated entirely, and separation can be prevented even up to $\alpha = 25°$. Karim and Acharya (1994) were able to eliminate the LEV on a NACA 0012 airfoil by using suction near the leading edge at specific points in the motion period to prevent reverse flow near the leading edge.

1.2.2.1 Dynamic stall on VAWTs

Dynamic stall on a representative one-bladed VAWT has been studied experimentally and computationally in the rotating frame at a limited number of angular positions at Reynolds numbers near operating conditions and tip speed ratios of 2, 3, and 4 by Simão Ferreira et al. (2007a,b, 2009, 2010). The growth of leading edge and trailing edge vorticity was analysed at several positions around the turbine cycle, and the total vortex circulation was shown to grow until the vortex was shed at the point of dynamic stall. Computations found the maximum tangential force on the turbine blade to occur at $\theta \sim 70°$ (Simão Ferreira et al., 2007a, 2010). Experiments performed by Buchner et al. (2015) on single bladed turbines, at a tip speed ratios between $1 \leq \eta \leq 5$ and dimensionless pitch rates $K_c = \frac{c}{2R}$, found that for a specific tip speed ratio, faster pitch rate resulted in less spatial growth of the LEV, resulting in weaker interaction between the leading and trailing edge vortices, and delaying LEV separation.

Direct numerical simulations were performed by Tsai and Colonius (2014) on VAWTs at low Reynolds numbers of less than 1500, using the immersed boundary method of Colonius and Taira (2008) and at tip speed ratios of $\eta = 2, 3$, and 4. They investigated the effect of the Coriolis force imposed by the rotating reference frame by performing computations in both the linear pitch/surge frame considered in this thesis, as well as the fully rotating frame, by adding a body force to the simulation. At a tip speed ratio $\lambda = 2$ the flow developed very similarly prior to separation with and without the Coriolis force, except for a slight phase lag in the forces on the blade in the linear pitch/surge motion. After separation a 'wake capturing' phenomenon was demonstrated in which the separated leading and trailing edge vortices appear to travel with the airfoil. This effect decreased lift after separation and during pitch down. The differences and similarities between flow in the linear and rotating frames will be discussed in more detail in Chapter 6.

Noting the efficacy of leading edge suction and trailing edge blowing, Untaroiu et al. (2011) used a slot running from near the leading edge to near the trailing edge of a VAWT blade to passively bleed air from leading to trailing edge. Experiments and simulation demonstrated a reduction in flow separation and increased circulatory lift. Greenblatt et al. (2013) were able to increase VAWT power output by 10% using feed-forward control with plasma discharge actuators to decrease the size of the dynamic stall vortex; however, they were not able to completely eliminate the vortex.

1.2.3 Leading edge vortex and lift force on accelerating bodies

Beckwith and Babinsky (2009) performed experiments on a flat plate at pre- and post-stall angles of attack of $\alpha = 5°$ and $\alpha = 15°$, respectively, accelerating to a Reynolds number of $Re = 6 \times 10^4$. In both cases they found a lift peak at the end of acceleration, as well as a second peak well above the steady state lift value for the $\alpha = 15°$ case. Experiments performed by Jones and Babinsky (2010) on rotating wings at $Re = 60,000$ showed significant unsteady lift increase during leading edge vorticity growth followed by a decrease below the steady value after the shedding of the leading edge vortex. Measuring the unsteady lift on a waving wing at many angles of attack between 5° and 45° (Jones and Babinsky, 2011) found a consistent increase in lift during acceleration, followed by a drop when acceleration is ceased for all angles of attack and at Reynolds numbers of $Re = 3 \times 10^4$ and 6×10^4. Additionally lift was shown to increase monotonically with angle of attack.

1.2.4 Vortex formation

In addition to the production of leading and trailing edge vortices associated with dynamic stall aiding in flapping flight (Rival et al., 2009), vortex rings have been identified as critical components of other unsteady periodic flow systems, such as those involved in jellyfish propulsion, and the flow around human heart valves (Dabiri, 2009). The physics behind this unsteady vortex formation process offers insight into the flow field development during dynamic stall on VAWT blades.

Gharib et al. (1998) analyzed the formation of vortex rings using a piston cylinder with different piston stroke to nozzle diameter ratios, and found that after a stroke ratio L/D ≈ 4, the vorticity in the ring saturated and began to convect away from the nozzle. L/D of four was proposed as the optimal 'formation number'; for shorter stroke ratios the vortex does not saturate and only leaves the nozzle at the end of the motion. Where as for longer motions a trailing jet was observed behind the initial vortex. Dabiri and Gharib (2005) extended this analysis to temporally variable diameters and velocities, definined the formation time as $\hat{T} = \int_0^T \frac{U}{D} dt$ (where $D = D(t)$ is the variable nozzle

diameter) and showed that vortex formation time remained consistent with the optimal formation time $\hat{T} \approx 4$. Experiments on flat plate oscillations (Milano and Gharib, 2005) and on accelerating flat plates (Ringuette et al., 2007) found optimal force production and vortex pinch-off at $\hat{T} \approx 4$. In a review, Dabiri (2009) showed that optimal vortex formation was a unifying principle in many biological systems.

On pitching and plunging flat plates, Baik et al. (2012) showed that for $k \leq 0.5$ the LEV circulation increased linearly up until vortex separation, corresponding to this optimal formation time, while at $k > 0.5$ the vortex was pinched off prematurely due the reversal of the airfoil motion. In experiments measuring various plunging motions at $k = 0.2 - 0.33$, Rival et al. (2009) also found that the formation of the leading edge vortex agreed with this optimal vortex formation time, and suggested that if the stroke motion could be altered such that the LEV saturated at the peak of the motion, the unsteady lift from LEV formation and dynamic stall could be used most effectively.

1.2.5 Vortex shedding

Vortex growth and shedding associated with the flow over bluff bodies and airfoils has been studied by many authors over a very large range of Reynolds numbers ($Re = 10^1 - 10^7$). The potential coupling of the resultant forces from this shedding with structural modes in a VAWT is a potential design concern due to observations of large structural oscillation and eventual failure (e.g. Blevins (1974); Bearman (1984)).

Roshko (1952) first proposed a fit for the Strouhal number based on cylinder diameter accurate for $Re_d = 300 - 10^4$ of

$$St_d = .212(1 - 21.2/Re_d) \tag{1.3}$$

Further work at higher Reynolds numbers and for multiple geometries (ovals, wedges, flat plates, etc) found that shedding was well described by a universal Strouhal number of $St \approx 0.18$ (Bearman, 1967; Roshko, 1961) based on the thickness of the wake. Joe et al. (2011) identified a similar Strouhal scaling based on cross-stream height $St = fc \sin\alpha / U_\infty \approx 0.2$ for separated flow over airfoils and flat plates at high angles of attack.

The effect of oscillating bluff bodies on the shedding frequency was discussed in a review by Bearman (1984). At frequencies close to the natural shedding frequency of the body, the vortex shedding was shown to lock on with the body motion, with shedding occurring when the motion reached its maximum amplitude. This phenomenon occurred with both forced bodies and unforced bodies where the motion was due to vortex induced vibration (Bearman, 1984).

Koochesfahani (1989) performed experiments on an NACA 0012 airfoil oscillating with an amplitude of $\Delta\alpha \geq 4^\circ$ around a mean angle of attack $\alpha_0 = 3^\circ$ at a Reynolds number of $Re = 12,000$, and reduced frequencies k between 0.8 and 10. At low reduced frequencies, $k < 1$ shedding occurred around the natural frequency for the stationary airfoil with a Strouhal number based on airfoil thickness $St_{th} \approx 0.33$. The vortices shed from the airfoil at the instantaneous, time varying position of the trailing edge then convected with the freestream resulting in a vortex street with a periodic wandering path. At higher frequencies $k \gtrsim 2$ vortices were shed with the opposite sense of rotation than the lower k case, corresponding to a jet flow from the airfoil, and thus provided thrust rather than drag (Koochesfahani, 1989). Similar experiments at lower reduced frequencies ($k = 0.1 - 0.4$) were performed by Jung and Park (2005), demonstrating a base Strouhal number based on airfoil thickness $St_{th} \approx 0.46$ at zero angle of attack dropping to $St_{th} \approx 0.3$ at $\alpha = 3^\circ$ as the wake thickened. In the case of the oscillating airfoil, the shedding frequency was shown to remain close to the $\alpha = 0^\circ$ value, especially at the higher k values when the wake had limited opportunity to develop given the short oscillation period.

1.3 Scope

The purpose of this work is to develop an understanding of how the flow phenomena discussed in section 1.2 interact on the blade of a vertical axis wind turbine. The decomposition of this flow into a linear frame provides unique insight into the physics of this flow, allowing each aspect of the flow physics to be investigated separately, then wrapped back together into the full flow field. Furthermore, the time resolved measurements permitted by this method facilitate the development of a simple reduced order model which is able to provide a new physical understanding of the dynamic stall process inherent in this flow. The instantaneous, non-phase-averaged, realizations of the unsteady flow highlight physical regimes not previously explored in the VAWT literature.

Chapter 2 describes the experimental setup and analytical techniques used to investigate this flow. In Chapter 3 the phase-averaged flow over the pitching and surging airfoil is presented. Isocontours of spanwise vorticity are shown to examine the evolution of separation and dynamic stall. A simplified model of the flow using only the first two harmonics of the pitch/surge motion is developed using dynamic mode decomposition and shown to capture the essential flow dynamics.

In Chapter 4 the inherent timesscales of dynamic stall, leading edge vortex development and vortex shedding in the VAWT model, are identified. The phase averaged flow field is further probed to isolate the leading edge vortex, and is compared to instantaneous realizations of the flow to

investigate vortex shedding.

In Chapter 5 the flow over airfoils undergoing solely pitch motion and surge motion at specific angles of attack is measured at the same reduced frequency as the combined pitch surge motion in Chapter 3. The combined pitch/surge flow is not expected to be a linear combination of these two effects; however, this decomposition provides insight into the the flow features associated each motion, as well as some indication of their mutual interaction.

Finally the results from linear measurements are wrapped back into the wind turbine frame in Chapter 6. Comparisons are made with two-dimensional direct numerical simulations performed by Tsai and Colonius (2014) in Dunne et al. (2015) to look further into the effect of the rotating frame, Reynolds number, and Coriolis forces.

Portions of this work have been published as Dunne and McKeon (2014), Dunne et al. (2015), and Dunne and McKeon (2015a,b).

Chapter 2

Approach

In this chapter, details of the experimental procedure for each type of experiment will be discussed. Particle image velocimetry (PIV) calculation parameters will be presented in detail, as well a description of any post processing of data. Additionally, mathematical data analysis techniques, such as spectral analysis and vortex identification techniques used in the following chapters, will be presented.

2.1 Experimental setup

2.1.1 Test facility

The goal of these experiments was to perform time-resolved measurements of a pitching and surging airfoil as a surrogate for the blade of a vertical axis wind turbine, as discussed in Chapter 1. In order to achieve realistic turbine blade Reynolds numbers and maintain slow enough flow and airfoil velocities for time resolved PIV, water was chosen as the working medium. Thus experiments were undertaken in the free surface water tunnel facility in the Graduate Aerospace Laboratories at the California Institute of Technology (GALCIT). A schematic of the tunnel adapted from Lehew (2012) and Bobba (2004) is shown in figure 2.1. The flow is recirculated with two pumps and passed through honeycomb and three screens before a 6:1 contraction, preceding the 1.5m long by 1m wide plexiglass test section. This flow conditioning resulted in a turbulence intensity $\sqrt{\overline{(u-\bar{U})^2}} \leq 0.1\%$ (Lehew, 2012) in the test section. In the following experiments the flow depth was maintained at 46cm $\pm$1cm for all experiments and the facility was run at a pump frequency of 30Hz, resulting in a freestream velocity $\bar{U} = 50\text{cm s}^{-1}$.

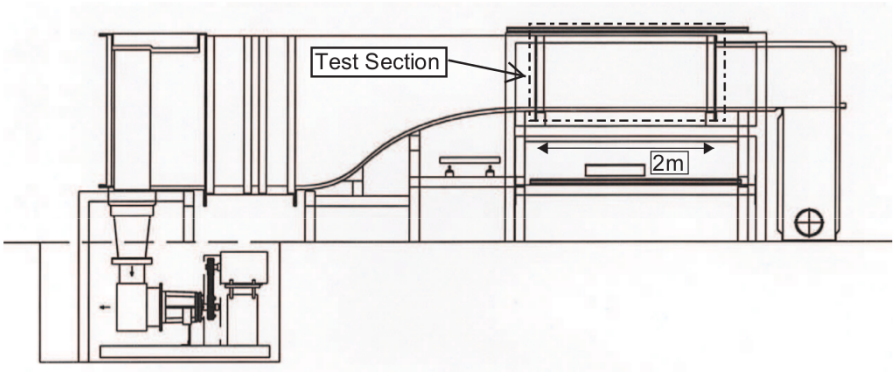

Figure 2.1: Tunnel schematic (Lehew, 2012)

2.1.2 Airfoil

A 200mm chord NACA 0018 airfoil was 3D-printed by Solid Concepts Inc. out of acrylonitrile butadiene styrene plastic with fused deposition modeling, painted black, and sanded smooth to minimize reflection from the PIV laser. The symmetrical NACA 0018 was chosen such that the flow on both pressure and suction side of the airfoil could be investigated in a single cycle while illuminating only one side of the airfoil. It is thick enough to be easily mounted in the water tunnel with negligible deflection along the span during high load. The NACA 0018 airfoil lift behavior has been characterized by Gerakopulos (2010) at Reynolds numbers between $8 \times 10^4 \leq Re \leq 2 \times 10^5$ and was shown to have a steady stall angle α_{ss} between 10 and 14 degrees, increasing with Reynolds number. The airfoil was shown to have a laminar separation bubble that decreases in size with Reynolds number, resulting in an increase in static lift coefficient. Furthermore, this airfoil has been used in multiple VAWT studies along with thinner airfoils of the same family NACA 0012-0015 (Simão Ferreira et al., 2007a,b, 2009, 2010; Islam et al., 2007). The test airfoil had an aspect ratio at test conditions of $AR = 2.3$. A similar airfoil with a 100 mm chord and $AR = 4.6$ was constructed similarly to investigate the effect of aspect ratio on the flow field.

2.1.3 Pitch and surge apparatus

The airfoil was attached to a 12.7mm (1/2") keyed shaft constructed of hardened stainless steel, so that the center of the shaft was aligned with the leading edge and suspended above the water tunnel with less than 1mm from the bottom wall of the test section to minimize tip effects. This shaft was supported by a thrust bearing and directly connected to a NEMA 34-485 microstepping 2-phase motor with holding torque of 3200N-mm. This resulted in a dynamic pitch system with 1/20,000 of a rotation (0.018°) accuracy, and zero backlash. The motor and thrust bearing were fixed to a

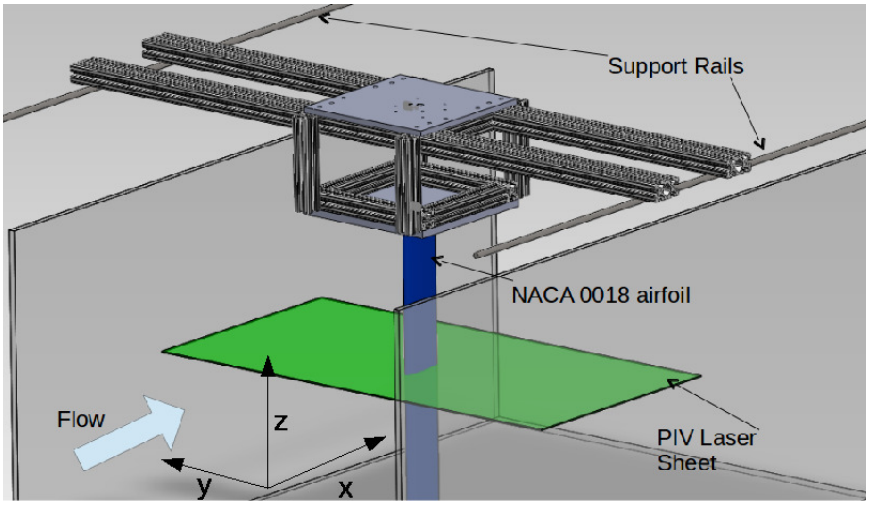

Figure 2.2: CAD model of the pitch/surge mechanism.

300mm square by 200mm deep aluminium cart mounted to linear bearings supported on rails outside the water channel. A CAD model of this cart in the tunnel is shown in figure 2.2. A 19mm ball nut was attached to the cart and actuated with a 1.22m long 19mm diameter ballscrew with backlash of $\leq$ 0.2mm. This ball screw assembly was attached to a NEMA 34-490 microstepping motor with holding torque of 9900N-m, resulting in linear position control system with 0.64μm accuracy. The motions of both pitch and surge control systems were measured using 2000 step optical encoders to further ensure accuracy and repeatability of the experiments. Control and measurement of angle of attack (pitch) and linear position (surge) were performed simultaneously using National Instruments LabVIEW$^{\text{TM}}$ and a National Instruments PCIe-6321 data acquisition card. A picture of this setup from above and upstream is shown in figure 2.3.

2.1.4 Experimental conditions

Experimental parameters, including Reynolds number, pitch and surge amplitude, frequency, and phase, were chosen to closely match those of a representative $\eta = 2$ vertical axis wind turbine similar to the windspire turbine used by Dabiri (2011) and Kinzel et al. (2012) in the American Wind Energy Association (AWEA) national average wind velocity of 5m s^{-1} (Brent, 2009). A mean chord Reynolds number of 10^5 was achieved in room temperature water with kinematic viscosity $\nu = 10^{-6}$m^2 s^{-1} and tunnel velocity $\bar{U} = 50$cm s^{-1}. Sinusoidal pitch between $\alpha_{\pm} - 30°$ and $30°$ about the leading edge (where the subscript $\pm$ indicates pitch up + and down -) and surge of

$$\frac{U_{max} - U_{min}}{\bar{U}} = 0.9 \tag{2.1}$$

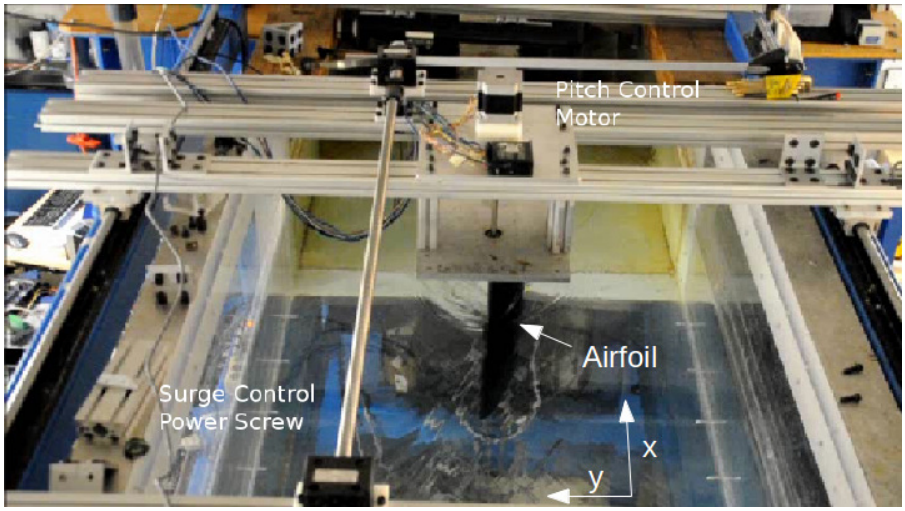

Figure 2.3: Picture of pitch/surge apparatus installed in test section.

were selected to closely match the angle of attack and Reynolds number variation of the turbine shown in figure 1.1. Maximum surge velocity was limited to 45% of free stream by the length of the test section and surge actuator. The frequency of the motion in the linear frame, i.e., the pitch and surge frequency, of $\Omega = 0.6\text{rad s}^{-1}$ was selected based on the reduced frequency of the full turbine

$$k = \frac{\omega c}{2\eta U_\infty} = 0.12 \tag{2.2}$$

in the rotating frame. Thus full-scale conditions of a real VAWT were closely replicated in the linear frame with the notable exception of the Rossby number. Note that $\theta = 0°$ in the rotating frame corresponds to maximum relative velocity U_{max} and $\alpha_+ = 0$. Therefore in the lab frame

$$U(t) = \bar{U} + 0.45\bar{U}\cos(\Omega t) \tag{2.3}$$

and

$$\alpha(t) = \Delta\alpha \sin(\Omega t), \tag{2.4}$$

where $t = 0$ corresponds to $\theta = 0$. For all experiments 10 cycles of the airfoil motion were completed before data was taken to eliminate any transient effects due to the start up of the airfoil. A comparison of α, $\dot{\alpha} = \frac{d\alpha}{dt}$ and $\ddot{\alpha} = \frac{d\dot{\alpha}}{dt}$ is shown in figure 2.4.

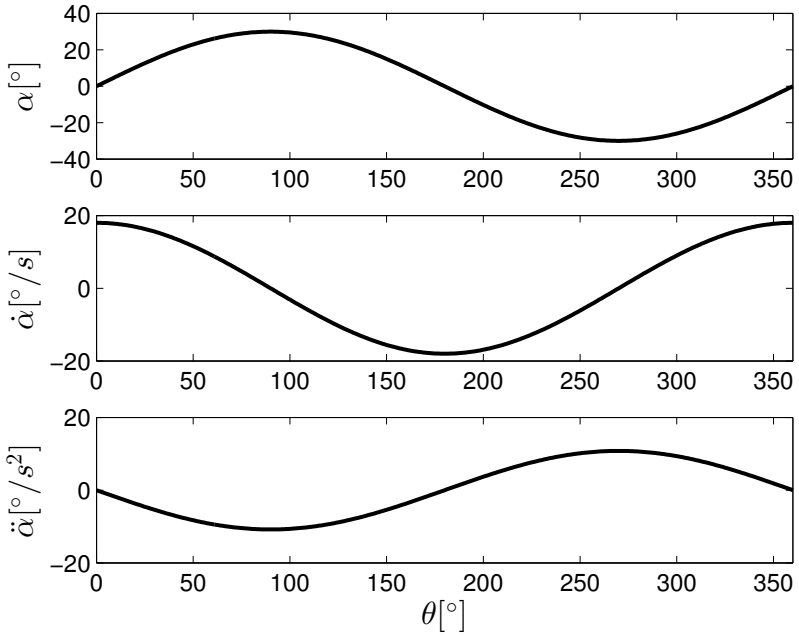

Figure 2.4: Angle of attack α, $\frac{d\alpha}{dt}$, and $\frac{d^2\alpha}{dt^2}$.

2.2 Diagnostics

Particle image velocimetry (PIV) was used to measure time resolve velocity fields in the streamwise/crosstream (x/y) plane as well as the streamwise/spanwise (x/z) plane to measure 3D effects.

2.2.1 Particle image velocimetry system and setup

A commercial PIV system built by LaVision and driven by DaVis 7 software was used to make PIV measurements. The flow was seeded with well mixed, neutrally buoyant, hollow, silver coated glass spheres approximately 100μm in diameter, purchased from Potters Industries. Illumination was provided by a 25mJ DM20-527 Photonics YAG laser passed through a cylindrical lens to produce a laser sheet approximately 1mm thick in the measurement window. Two Photron Fastcam APS-RX CMOS cameras capable of sampling at 3000Hz at full 1024 $\times$ 1024 pixel resolution were used for image acquisition.

A schematic of the PIV setup for streamwise/cross-stream measurements is shown in figure 2.5. The laser head was placed on a hight adjustable stand, and the cylindrical lens was mounted on a small optical table 15cm away from the laser head. This stand was mounted approximately 1m from the near wall of the test section, levelled and aligned perpendicular to the test section as seen. This illuminated a plane of the flow z = 200mm from the floor of the test section, and greater

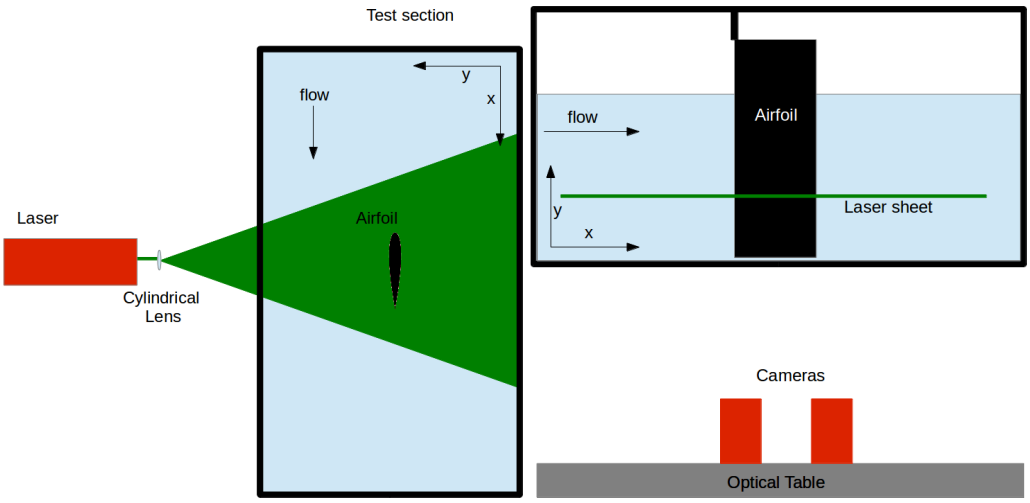

(a) View from above test section, flow from top to bottom.

(b) View from side of test section, flow from left to right.

Figure 2.5: Schematic of PIV setup for streamwise/cross-stream measurements.

than 700mm in the streamwise direction, such that the flow within the camera field of view was well illuminated. Both cameras were mounted to an optical table on the floor of the laboratory, underneath the test section, isolated from the tunnel to avoid unnecessary mechanical vibration. The cameras were aligned in the cross-stream direction and offset in the streamwise direction such that they observed the maximum streamwise distance with approximately 1.5c overlap necessary to knit the flow fields from both cameras together in post processing. The cameras were levelled, such that the field of view was parallel to the illumination, and focused on the laser sheet.

For streamwise/spanwise measurements the laser head and cylindrical lens were lowered below the test section, and a large mirror was placed at a 45° angle in the streamwise direction to reflect the laser sheet parallel to the airfoil. The laser was aligned such that it was $\leq$ 1mm from the closest portion of the airfoil (the leading edge or the 1/4 chord point depending on angle of attack) to the camera, so it was not obstructed by the airfoil. The cameras were placed by the side of the test section with similar streamwise overlap to the x/y measurements, providing a field of view approximately 500mm by 225mm (2.5×1.13c) in the streamwise/spanwise direction. These measurements were performed 150mm from the floor of the test section, and from 0.5c upstream to 2c downstream of the airfoil leading edge. Clear from the schematic (figure 2.6) the cameras are aligned above the laser head, and the laser passes through the bottom of the test section parallel to the airfoil.

For all experiments images were captured at 80Hz with an exposure time of 1/400s, yielding 2047 velocity fields with a duration of 25.6s or 2.5 motion cycles. 80Hz provided sufficient time resolution

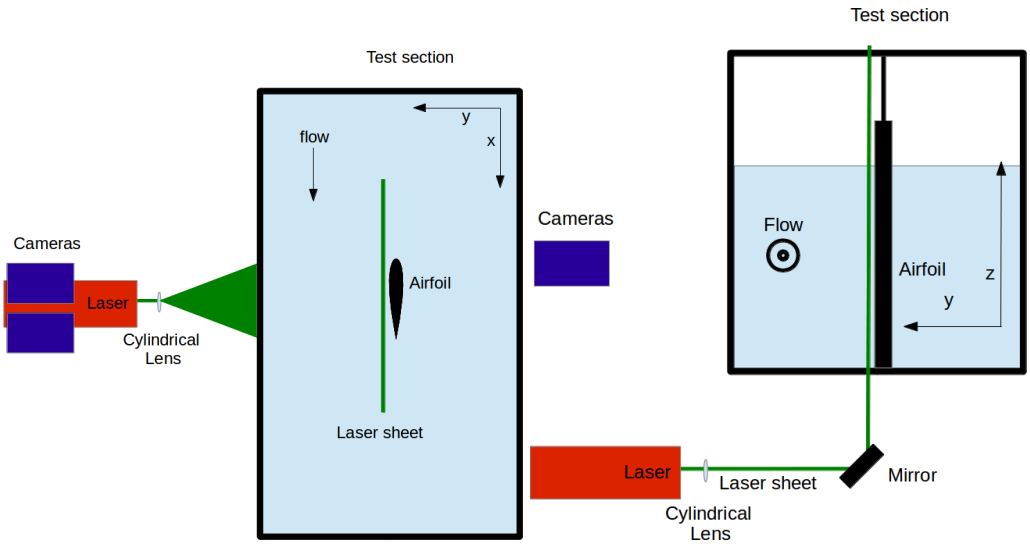

(a) View from above test section, flow from top to bottom.

(b) View from behind test section with flow coming toward the reader.

Figure 2.6: Schematic of PIV setup for streamwise/spanwise measurements.

to measure all expected flow behavior, resolving frequency several times higher than the expected Strouhal shedding of the airfoil at

$$F \sim \frac{St * U_{max}}{th} = \frac{0.2 * 0.75}{0.2 * 0.018} = 4.17\text{Hz}, \tag{2.5}$$

where th is the thickness of the airfoil and U_{max} is the maximum possible airfoil relative velocity. Furthermore, given camera storage restrictions of $N = 2048$ images per experiment, 80Hz permitted multiple motion cycles to be measured in each individual experiment. An exposure time of 1/400s yielded bright distinct particles with negligible motion and was sufficient for all experiments. The composite field of view, once images from both cameras were knit together, was 69×31cm (3.5×1.5c) streamwise x cross-stream.

2.2.2 Vector processing

Velocity vectors were calculated for each camera using LaVision DaVis software. Three vector processing runs were performed with a 50% window overlap and decreasing interrogation window of 64 pixels for the first run and 32 for the final two. Vector validation was performed, and spurious vectors were removed and replaced by interpolation. The final data was smoothed in space using a 3×3 moving average filter. These parameters yielded a spatial resolution of 5.5×5.5mm (0.028×0.028c). Finally, the velocity vectors from both cameras were knit together to form a single field of

view. Three different methods of knitting these velocity fields were tested to understand their effect on the flowfield. First, the *merge vectors* post processing step within the Davis software, which re-interpolates both results into a single x/y grid, was used. Second a similar re-interpolation was performed manually in MATLAB, and finally both measurement fields were cropped such that there was an overlap consisting of an integer number of interrogation windows (as in Lehew (2012)), and the vector fields were reassembled without any interpolation. The three methods demonstrated negligible quantitative or qualitative differences and, as such, re-interpolation to a grid within MATLAB was used for all following results.

2.3 Data sets

Experiments were performed on airfoils undergoing a combined pitch/surge motion with amplitude and phase determined by the VAWT at $\eta = 2$ shown in figure 1.1, as well as solely pitch motion and surge motion at $\alpha = 15°$ and $20°$. Due to the large airfoil motion in the streamwise (x) direction required for the pitch/surge combined experiments and surging experiments separate experiments, were performed in somewhat overlapping front and back fields of view. The position of the airfoil in each of these fields of view can be seen in figure 2.7(a). In each of these experiments the airfoil position (x_l, α) was carefully measured with (where $x_l = x_l(t)$ is the time varying position of the leading edge of the airfoil in the laboratory reference frame). The position of x_l with respect to θ is shown in figure 2.7(b). Experiments were performed until fifteen datasets with measured leading edge position x_l within 1% and angle of attack α within 0.5° of desired position were completed. The following data sets will be considered in this thesis. In all cases data is only presented on the top surface of the airfoil, as the shadow of the airfoil prevents PIV vector calculation on the bottom surface (figure 2.7(a)).

2.3.1 Pitch/surge combined motion

Two different data sets are considered in the combined pitch surge field of view.

2.3.1.1 Phase-averaged data

For phase-averaged data set fifteen experiments, performed in both the front and back fields of view, were ensemble averaged together based on the phase of the airfoil motion. This ensemble averaged data was then knit together to form a near complete picture of the averaged flow for 2.5 periods of

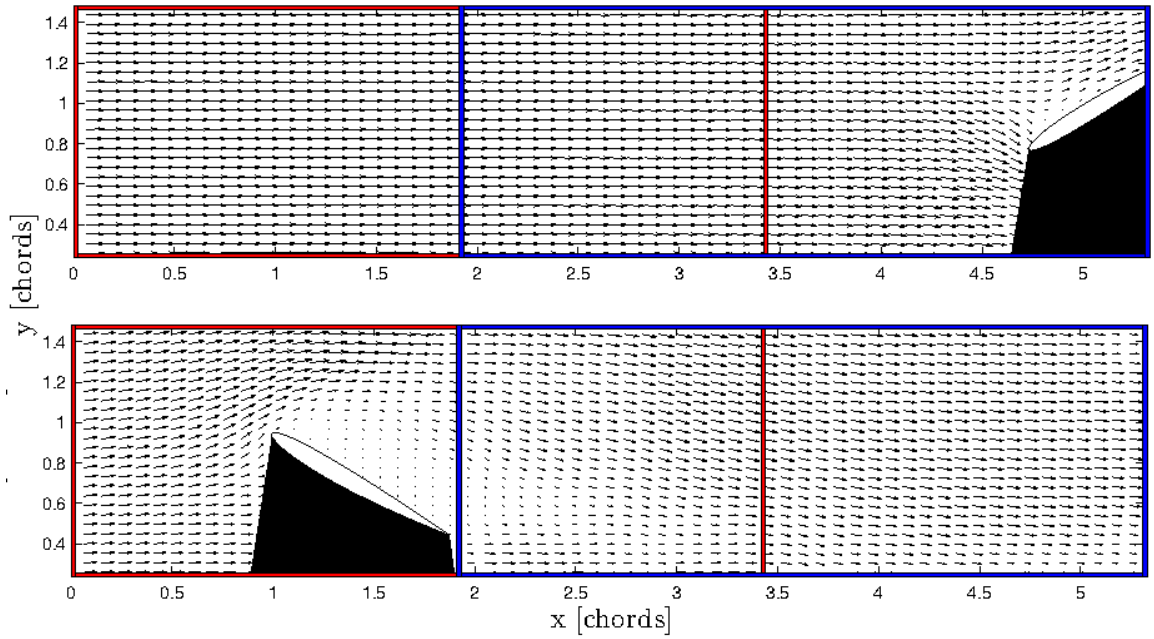

(a)

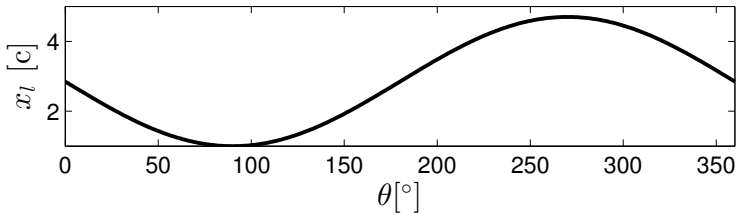

(b)

Figure 2.7: (a. top) Experimental field of view in laboratory frame. Front and back fields of view shown in red and blue, respectively. Top panel shows airfoil in maximum aft position, bottom in maximum forward position for pitch/surge and surging motion (pitch/surge shown). Pitch only experiments were performed only in the front field of view, at the maximum forward position $x_l = 1$ shown in the top panel. (b. bottom) Plot of leading edge position x_l in airfoil motion cycle.

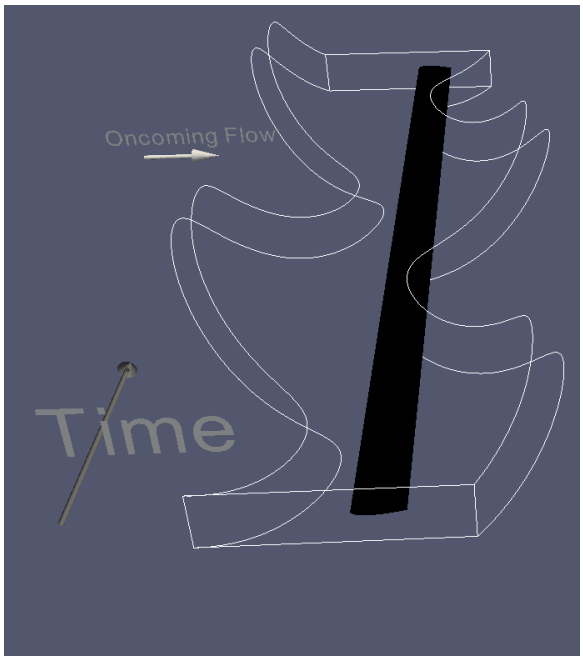

Figure 2.8: Field of view in the airfoil-fixed frame. Time is extruded in the z direction to show entire time series in one image. White lines show how field of view moves around in the airfoil fixed frame. Flow is from left to right.

the pitch/surge motion. This composite field of view measures the flow over the leading edge of the airfoil for its entire cycle. As a final post processing step the velocity fields were rotated into the airfoil reference frame with the leading edge at the origin with positive x in the upstream direction. White lines in figure 2.8 show the position of the rotated field of view over the airfoil where time has been extruded along the z axis. Further experiments would be necessary to examine the trailing edge at the furthest aft point in the cycle.

2.3.1.2 Instantaneous data

The instantaneous data set consists of single experiments performed in both the front and back fields of view. These data sets are used to investigate behavior not directly linked to the motion of the airfoil, and therefore averaged out by the phase-averaging process. These data sets are presented individually and are left in the laboratory frame as in figure 2.7(a).

2.3.2 Pitch motion

The pitch motion data set is a phase average of the fifteen experiments based on the airfoil angle of attack. Due to the lack of surging motion experiments were only performed in the front field of view, which was centered under the airfoil leading edge (the axis of rotation for pitch). These experiments

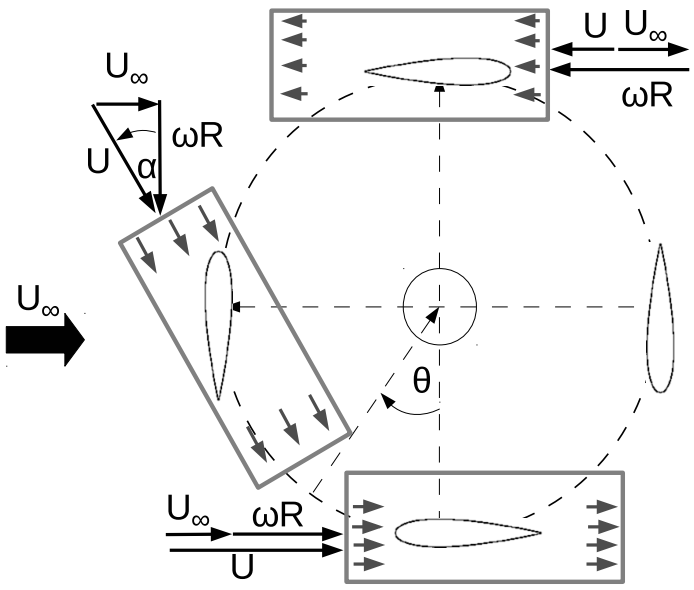

Figure 2.9: Top view of a VAWT demonstrating experimental field of view in rotating VAWT frame. Wind speed U_∞, effective velocity U, blade velocity ωR. Experimental field of view shown by grey boxes (not to scale).

measure a velocity field over the entirety of the airfoil for the full motion period. Velocity fields are presented in the airfoil fixed field of view.

2.3.3 Surge motion

Experiments on the surge motion were performed at two angles of attack $\alpha = 15°$ and $\alpha = 20°$. For both cases experiments were performed in the front and the back field of view, then phase-averaged and knit together based on the position of the leading edge, similar to the combined motion in 2.3.1. These measurements are presented in the airfoil fixed field of view.

2.3.4 Reference frame

In the reference frame of the rotating VAWT the linear pitch/surge experiments is equivalent to performing measurements in a non-inertial reference frame moving with the blade (figure 2.9). The result of this rotating reference frame is to impose a Coriolis and centrifugal force which are neglected in the linear pitch/surge experiments. The non-dimensional momentum equation in this rotating frame is given by

$$\frac{\partial \hat{u}}{\partial t} + (\hat{u} \cdot \nabla)\hat{u} = -\nabla p + \frac{1}{Re}\nabla^2 \hat{u} - \frac{2\omega c}{U_\infty} \times \hat{u} - \omega \times (\omega \times \hat{x}) \tag{2.6}$$

(Tsai and Colonius, 2014), where p is the pressure, $\hat{u}$ and $\hat{x}$ are the velocity and position vectors, in the rotating frame, respectively. The last two terms in this equation ($\frac{2\omega c}{U_\infty} \times \hat{u}$ and $\omega \times (\omega \times \hat{x})$) individually represent the Coriolis and centrifugal forces. Taking the curl and divergence of this equation result in the vorticity and pressure equations. The Coriolis force appears in both of these equations, and has an effect on vortex convection as discussed in chapter 6 as well as by Tsai and Colonius (2014). The centrifugal term however only appears in the pressure equation, as a pressure gradient perpendicular to the airfoil chord. As such the centrifugal force has no effect on the velocity field, and because the pressure gradient is perpendicular to the direction of airfoil motion it does not effect the torque on the resulting turbine.

2.4 Analysis techniques

2.4.1 Vortex identification

The Γ_1 and Γ_2 criteria developed in Graftieaux et al. (2001) were used to identify vortices in the flow field. These methods calculate a vortex center and core location, respectively, based on the velocity field, avoiding numerical derivatives as required for methods based on the velocity gradient tensor such as the Q, λ_2 or λ_{ci} criteria (Chakraborty et al., 2005), thus making them less sensitive to numerical noise. Γ_1 and Γ_2 at a point P within boundary S are given by

$$\Gamma_1(P) = \frac{1}{S}\int_{M\in S} \frac{PM \times U_M \cdot z}{||PM|| \cdot ||U_M||} dS = \frac{1}{S}\int_S \sin(\theta_M) dS \tag{2.7}$$

$$\Gamma_2(P) = \frac{1}{S}\int_{M\in S} \frac{PM \times (U_M - U_P) \cdot z}{||PM|| \cdot ||(U_M - U_P)||} dS, \tag{2.8}$$

where S is the area around P and M lies on S. PM is the radius vector from P to M, U_M is the velocity at point M, θ_M is the angle between PM and U_M, and U_P is the local convection velocity at P.

For the data in this thesis a circular stencil with a radius of three grid cells was generated with MATLAB and summed to approximate the integrals in equations 2.7 and 2.8. A small change to the radius had little effect on the results; however, if too large a stencil was chosen vortices were missed or smeared together. If too small a value were chosen, single vortices could be split up into two, and the results were sensitive to noise. A downside of the Γ criteria is that Γ_1 is non-Galilean invariant (though Γ_2 is) (Graftieaux et al., 2001), and thus the freestream velocity relative to the

airfoil U was subtracted from the flow field at each time step before the Γ criteria were used to perform vortex identification in the reference frame of the airfoil.

A threshold of $\Gamma_1 \geq 0.7$ was chosen for each data set to indicate the existence of a vortex, and $\Gamma_2 = 2/\pi$ indicates the boundary where rotation is stronger than shear (Graftieaux et al., 2001). A vortex is only considered to exist if both criteria are met, i.e., $\Gamma_1 \geq 0.7$ somewhere within the region where $\Gamma_2 \geq 2/\pi$. The choice of $\Gamma_1 = 0.7$ yielded the best results over the broad range of data chosen, striking a balance between an overly sensitive metric (low Γ_1) that identified vortices from noise and too restrictive a metric that caused no vortices to be identified. Requiring both metrics resulted in a strict vortex measure to ensure that no spurious vortices were used for calculation. In some cases however this caused vortices to not appear in a given timestep, and as such appears as occasional data drop outs in the results presented in this thesis.

For the rest of this thesis the location of the vortex is given by the location of the maximum of Γ_1. Integral quantities, such as vortex size and circulation, are calculated within the $\Gamma_2 \geq 2/\pi$ boundary. A 3D connectedness algorithm was implemented in MATLAB, using the *bwlabeln* command, to track vortices in time, which depending on the data set identified between 100 and 500 vortices, with significantly fewer appearing in the phase averaged data. The circulation (μ_Γ) within the vortex boundary $\Gamma_2 > 2/\pi$ was calculated using Stokes theorem

$$\mu_\Gamma = \iint_{\Gamma_2 > 2\pi} \chi dA, \tag{2.9}$$

where χ is the spanwise vorticity.

In these flows a leading edge vortex is expected to appear during the positive, pitch up portion of the airfoil motion cycle ($\alpha_+ \leq 0$). As discussed in section 1.2 this vortex is expected to include a significant portion of the total circulation and be coherent in time up until it is shed from the airfoil. Thus the LEV was identified as the vortex with the largest integrated circulation over the pitch up period

$$max \, \forall \, v \left(\int_{\alpha=\alpha_0}^{\alpha=\alpha_0+\Delta\alpha} \mu_\Gamma^v(\alpha) d\alpha \right), \tag{2.10}$$

where μ_Γ^v is the circulation of vortex v at each timestep parametrized by angle of attack α. This method is robust for both phase-averaged results and individual data sets since the vortex is strong and long lasting in time.

2.4.2 Dynamic mode decomposition

The Dynamic Mode Decomposition (Schmid, 2010), was used to dissect the flow fields into single frequency modes ϕ that can be ranked by their dynamic significance. The algorithm, which is developed in detail by Schmid (2010) estimates a mapping $\mathbf{S}$ between each timestep of the measured velocity field $\mathbf{V}$. DMD modes $\Phi_j = \mathbf{U}\mathbf{y_j}$ are computed, where $\mathbf{U}$ are the right singular vectors of the time sequence $\mathbf{V}$ and $\mathbf{y}_j$ are the eigenvectors of $\mathbf{S}$. $\lambda_j = log(\mu_j)/\Delta t$ transforms μ_j, the eigenvalues of $\mathbf{S}$, such that λ_j is the complex temporal growth rate for each dynamic mode ϕ_j, where Δt is the timestep between each velocity snapshot. Using this transformation, the frequency of each mode is given by Imaginary$(\lambda) = \lambda_i$ and modes with Real$(\lambda) = \lambda_r > 0$ are growing and $\lambda_r < 0$ decay. Finally, a relative measure of the amplitude of each DMD mode, a_j, is computed. The reader is referred to Schmid (2010) for more detail.

The DMD algorithm is insensitive to non-integer numbers of periods (Chen et al., 2012). As such the data set is not truncated in time, but the full time sequence of 2.5 periods is used to achieve optimal convergence of the DMD modes. For purely periodic data the modes found using DMD are identical to the Fourier modes from a discrete Fourier transform (Rowley et al., 2009). More recently Hemati and Rowley (2015) found that the classical DMD algorithm is very sensitive to snapshot noise, and often miscalculates modal growth/decay rates. They developed a noise-robust total DMD algorithm that was found to improve the measurement of modal growth rates in many simple flows. In this study DMD was used to find these modes from not purely periodic data and from a small, non-integer number of periods from both phase-averaged and instantaneous measurements; it also was used to pick out modes with strong dynamic significance, to calculate low order models of the flow, and, as a Fourier filter, to analyze frequency content. This type of spectral method is ideal for this type of flow since the input signal, i.e. the blade motion, is sinusoidal with a single frequency, and as such can be identified using a single frequency mode. Furthermore, coupled modes at harmonic frequencies are also identified by the analysis. Lastly, by separating out the frequencies associated with the periodic motion, behavior of the flow caused directly from the motion can be decoupled from other physical phenomena. As such, the dynamic mode decomposition can be used not only to reduce the order of the base flow model, but also to directly investigate the physics inherent in dynamic stall.

2.5 Three-dimensional effects

Experiments in the streamwise/spanwise plane as discussed in section 2.2.1 were performed to analyze the spanwise variation and three-dimensionality of the flow. These experiments were performed on the primary 200mm chord airfoil at full Reynolds number of 10^5 at static angles of attack of $\alpha = 10°$, $15°$, and $20°$. Similar experiments were performed on the smaller airfoil at the same freestream velocity, resulting in $Re = 5 \times 10^4$ and the full chord airfoil at $Re = 5 \times 10^4$ to compare the effect of aspect ratio.

2.5.1 Basic velocity profiles

The mean streamwise velocity profiles at the measurement plane used for later experiments, $z =$ 200mm, at angles of attack $\alpha = 10°$, $15°$, and $20°$, are plotted in figure 2.10. At $\alpha = 10°$ the u velocity increases in the region just behind the leading edge, reaching a peak at $x/c \sim 12\%$, and then decreases to near the freestream velocity behind the airfoil $x/c \geq 1$. This effect is caused by the local acceleration of the flow as it curves around the leading edge of the airfoil. At $\alpha = 15°$, however, the flow velocity decreases, and, in fact, reverses with a maximum amplitude of $\frac{u}{\bar{U}} = -0.4$ near $x/c = 0.25$ before returning to a somewhat increased velocity at $x/c = 0.5$. This indicates a separation bubble on the airfoil that extends away, in y, from the leading edge to the measurement domain. This separation bubble begins near the leading edge, and the flow re-attaches near midchord; however, exact determination of this position cannot be made without measurements at the airfoil surface, and is not the focus of this study. Finally, at $\alpha = 20°$ u decreases at the leading edge, quickly approaching $\frac{u}{\bar{U}} = 0$. This indicates fully separated flow over the airfoil at this high angle of attack.

2.5.2 Spanwise variation of u

Contour plots of average u scaled by the freestream velocity $\bar{U}$ for all three angles of attack are shown in figure 2.11, with the location of the streamwise/cross-stream measurement plane corresponding to the data repeated later shown by the green line. Units in the z direction are left dimensional (in mm) to indicate distance from the floor of the water channel.

As can be seen from these images, the flow is fairly constant in the spanwise direction near the x/y measurement region of $z = 200$mm; however, the different flow states discussed above can be seen in all three cases. Near the top of the measurements for $\alpha = 10°$ and $15°$ in figure 2.11 a clear

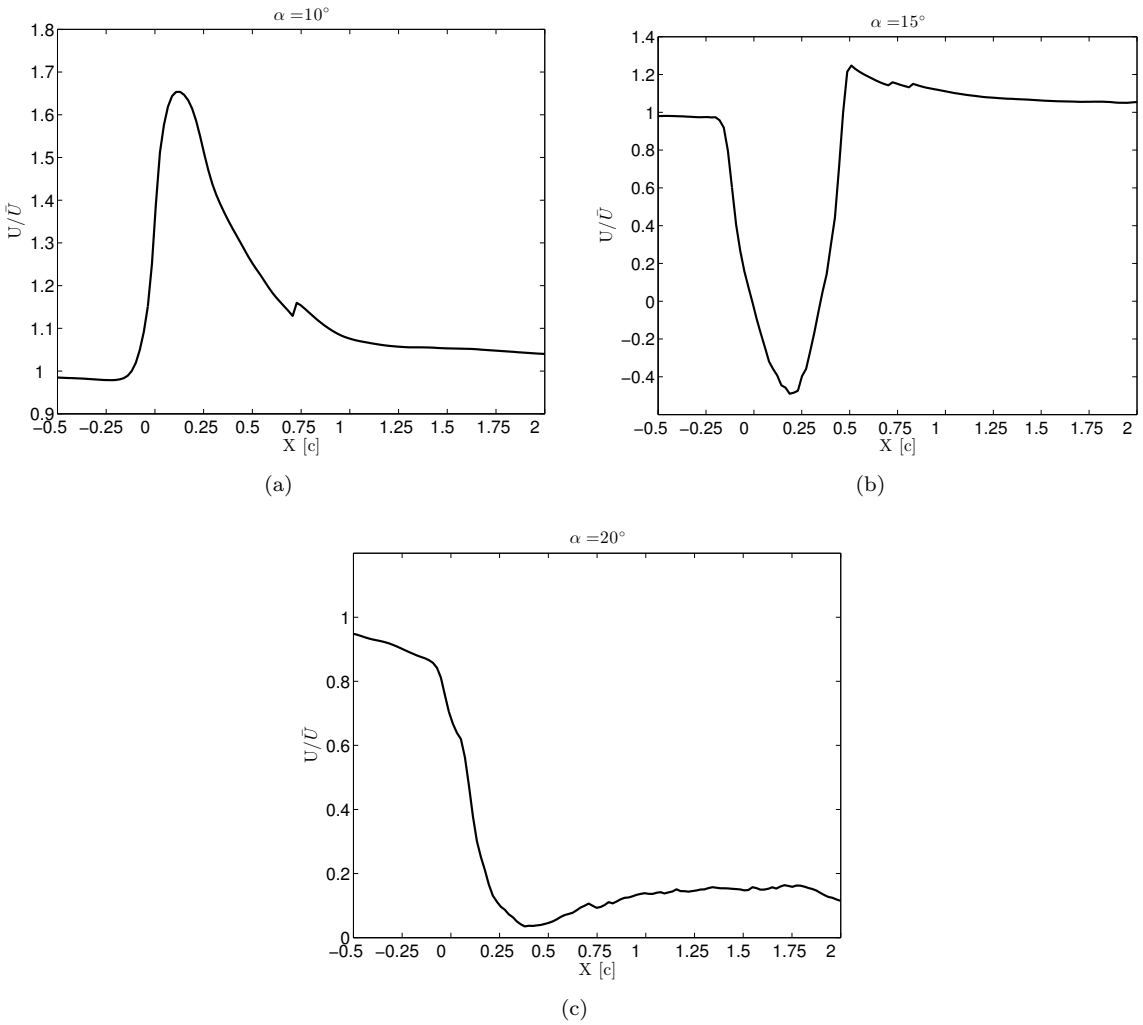

Figure 2.10: Mean streamwise velocity u for $\alpha = 10°$ (a), $\alpha = 15°$ (b) and $\alpha = 20°$ (c) scaled by the freestream velocity $\bar{U}$, at $z = 200$mm (x/y measurement domain).

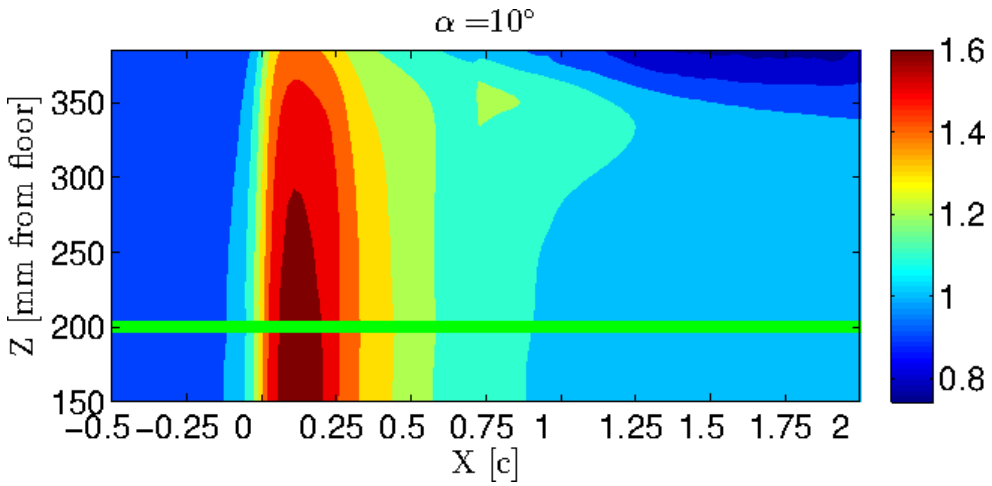

(a)

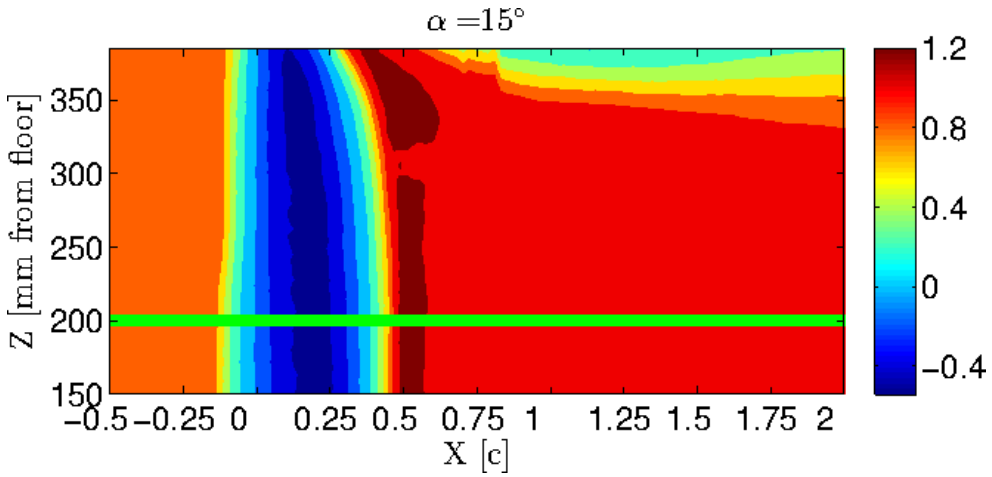

(b)

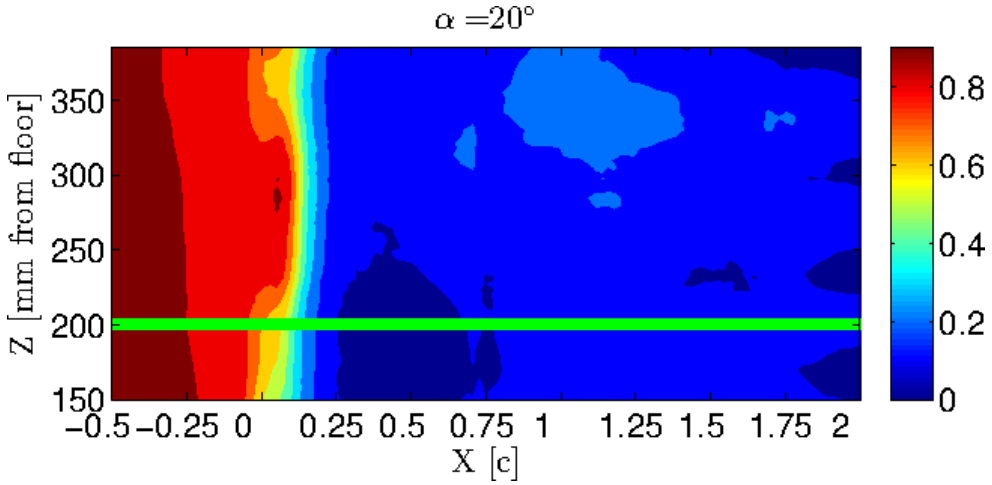

(c)

Figure 2.11: Contour plots of average u velocity, scaled by the freestream velocity $\bar{U}$, measured in x/z plane at static angles of attack. Airfoil leading edge at $x = 0$. Water tunnel floor at $z = 0$ (units in mm), water depth 457mm. x/y measurement plane/laser at $z \sim 200$mm shown by green line on plots.

u velocity deficit can be seen beginning at approximately the midchord and growing downstream to $z \gtrsim 350$cm.

2.5.3 Mean spanwise flow

Mean spanwise velocity w at the measurement region, $z = 200$mm, is plotted in figure 2.12. In all three cases there is a slight upward (toward free surface) bias in the incoming flow $\frac{w_{max}}{U} \lesssim 0.02$. For $\alpha = 10°$ and $15°$ this bias goes away and the spanwise flow approaches zero where there is an effect of the airfoil on the streamwise velocity, corresponding to flow rotation and the separation bubble respectively. At the maximum angle of attack, when the flow is fully stalled, there is slight negative (toward wall) velocity ($\frac{w_{max}}{U} \lesssim 0.08$) at the airfoil that decays away after $x/c \sim 1$. This can also be seen in the contour plot, figure 2.13(c), with towards wall velocity increasing with negative z centered at the mid chord.

The velocity deficit seen near the top of figures 2.11(a) and 2.11(b) corresponds to a small negative w velocity over the entire airfoil chord most extreme at the top of the airfoil (figures 2.13(a) and 2.13(b)). This velocity deficit and spanwise flow are a result of the depression of the free surface on the pressure side of the airfoil, and as can be seen are contained within the top 100mm of the test section, and do not have an effect on the x/y measurements that are the focus of this work.

2.5.4 Instantaneous measurements

The variance of the u and w velocity is plotted in figure 2.14 to investigate the variation around the mean values shown above. Both show negligible variation, except for peaks near the leading and midchord, as well as a peak in the streamwise velocity variance just before the quarter-chord. These locations correspond to the beginning, end, and middle of the separation bubble identified in figure 2.11(b). To investigate this behavior a vector plot of one realization of the flow at $\alpha = 15°$ is shown in figure 2.15. In this image the uniform incoming and exiting flow can be clearly seen as well as reverse flow in the separation bubble. At the leading and trailing edges of the bubble some spanwise flow can be seen, accounting for the increased variance; this effect may indicate the presence of 3D stall cells. However, there is significant out-of-plane velocity in this section and as such the velocity fields in these regions are not well resolved. The appearance of stall cells in this flow would be consistent with the work of Weihs and Katz (1983), who found that the number of stall cells $n = AR/2.28$ for separated airfoils in this regime. For the experiment discussed here that would correspond to $n = 1$ stall cell appearing. In the core of the laminar separation bubble the

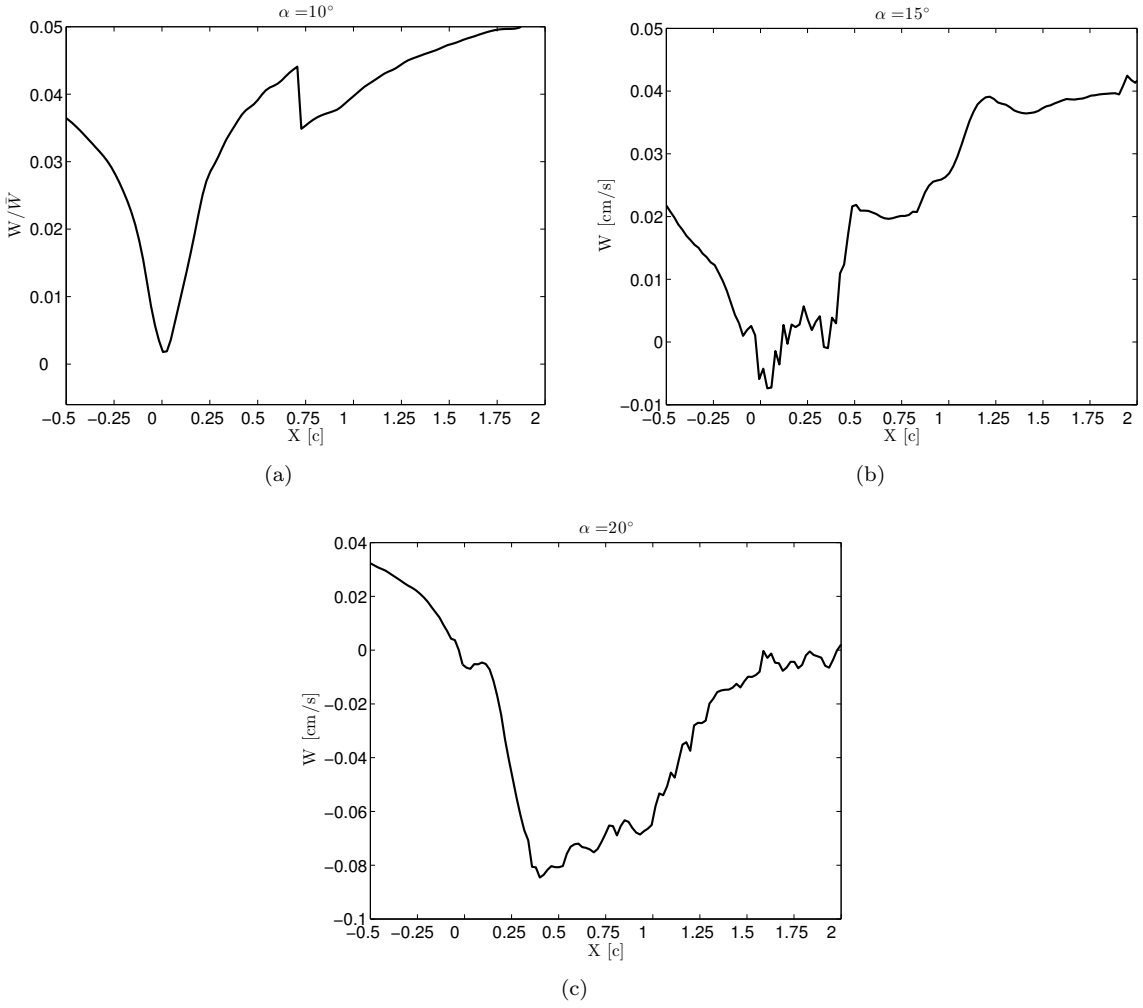

Figure 2.12: Mean spanwise velocity w scaled by the freestream velocity $\bar{U}$, at $z = 200$mm (x/y measurement domain).

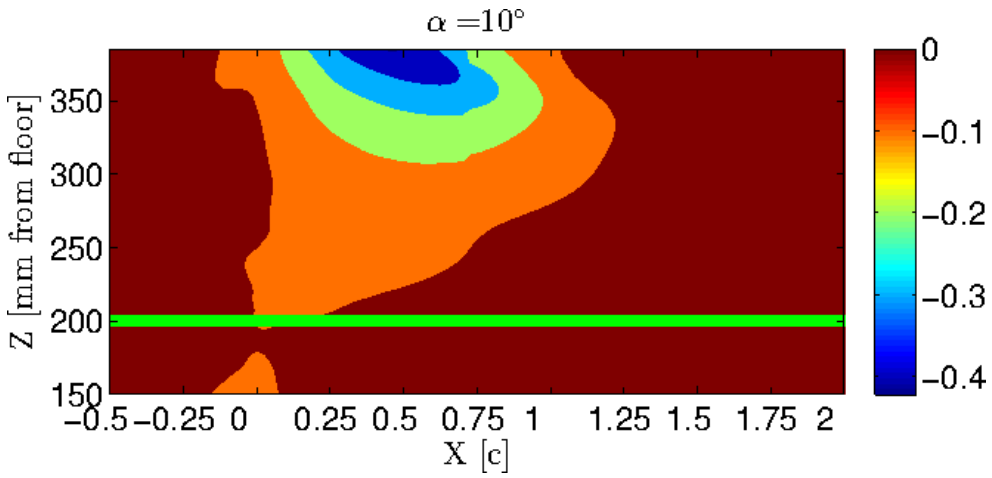

(a)

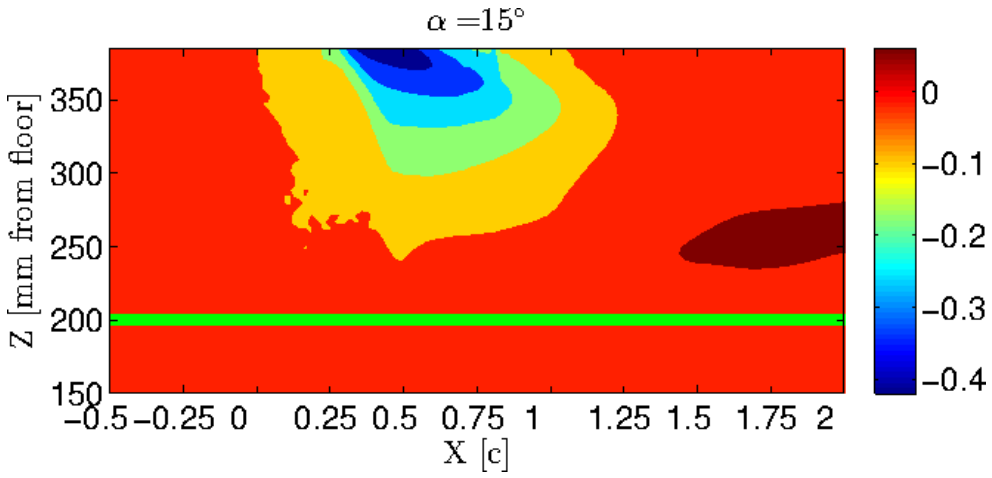

(b)

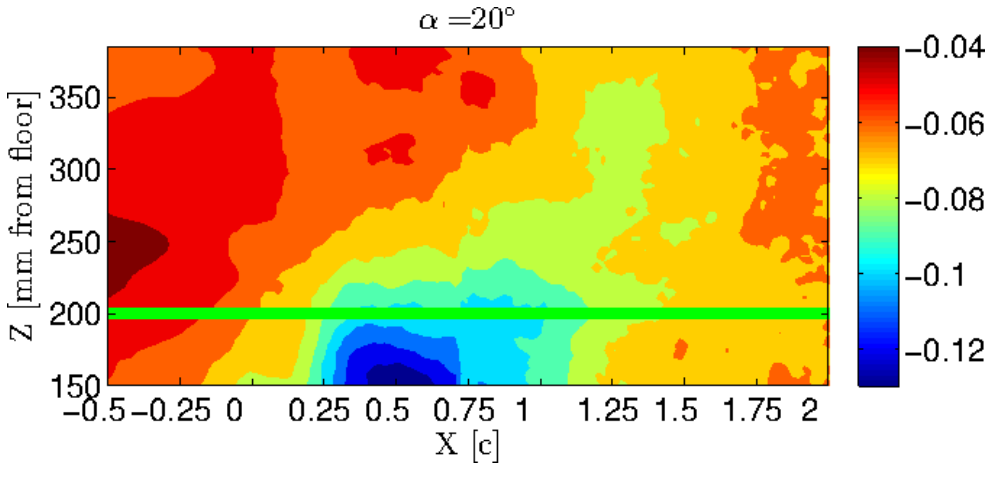

(c)

Figure 2.13: Contour plots of average w velocity, scaled by the freestream velocity $\bar{U}$, measured in x/z plane at static angles of attack. Airfoil leading edge at $x = 0$. Water tunnel floor at $z = 0$ (units in mm), water depth 457mm. x/y measurement plane/laser at $z \sim 200$mm shown by green line on plots.

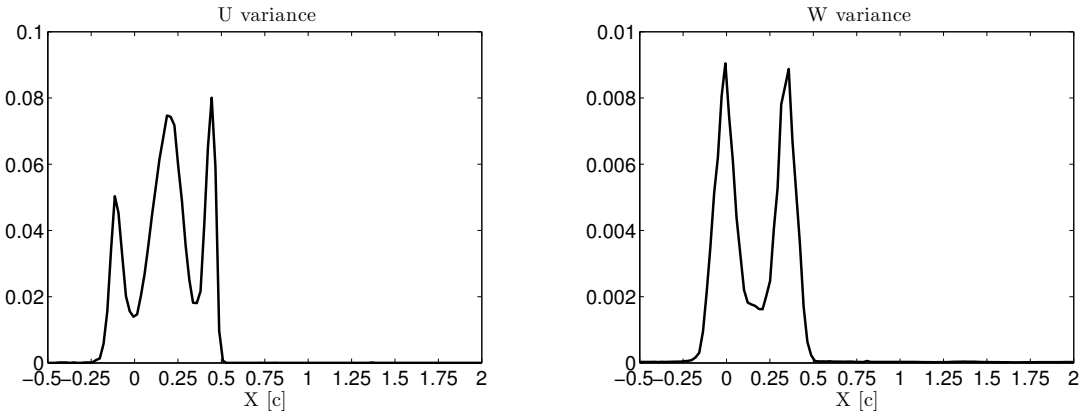

(a) (b)

Figure 2.14: Variance of u and w at $z = 200$mm (x/y measurement domain) $\alpha = 15°$.

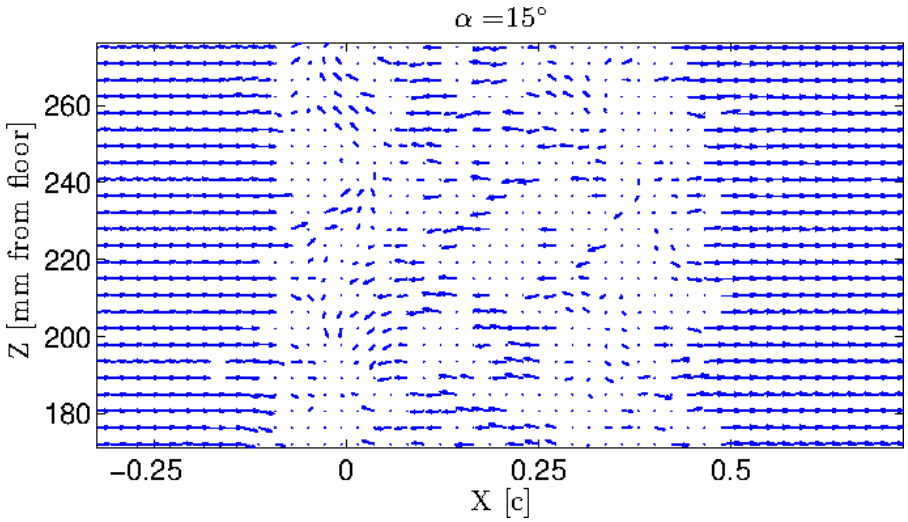

Figure 2.15: Vector plot instantaneous vector field for airfoil at $\alpha = 15°$.

measurements show negative u velocity and minimal w velocity, but there is significant unsteadiness in this region in the x/y plane resulting in the increase in u velocity variation.

2.5.5 Effect of aspect ratio

Contour plots of the u and w velocity fields on the 100mm chord airfoil with aspect ratio $AR = 4.6$ at $Re = 50,000$ are plotted in figures 2.16 and 2.17 for comparison with the results of figures 2.11 and 2.13. Qualitatively both the u and w fields are the same as the larger airfoil at $\alpha = 10°$, demonstrating an increased velocity as the flow accelerates around the airfoil; however, velocity deficit at high z values does not appear as the smaller airfoil causes less of a disturbance in the free surface. At the higher angles of attack, however, the separation bubble and fully separated region in

$\alpha = 15^\circ$ and $\alpha = 20^\circ$ respectively are not captured, but instead a slight increase of velocity is seen from $0 \lesssim x/c \lesssim 0.25$. The separated regions cannot be measured in these experiments, since on the smaller airfoil they extend a correspondingly smaller distance in y from the airfoil, and as such do not extend to the measurement domain. The flow is still expected to exhibit a separation bubble as well as full separation at this lower Reynolds number; however, it cannot be directly measured using this setup. The flow fields from experiments on the large airfoil at $Re = 50,000$ show similar results to those at $Re = 100,000$.

Measurements were performed in the streamwise/spanwise (x/z) plane to investigate any three-dimensionality in the base flow, as well as to test any aspect ratio as well as free surface effects. Minimal average spanwise flow was found at the x/y measurement domain for all three angles of attack tested. Some free surface effects were seen due to the perturbation of the surface by the airfoil; however, these effects did not extend to the plane of the x/y measurements.

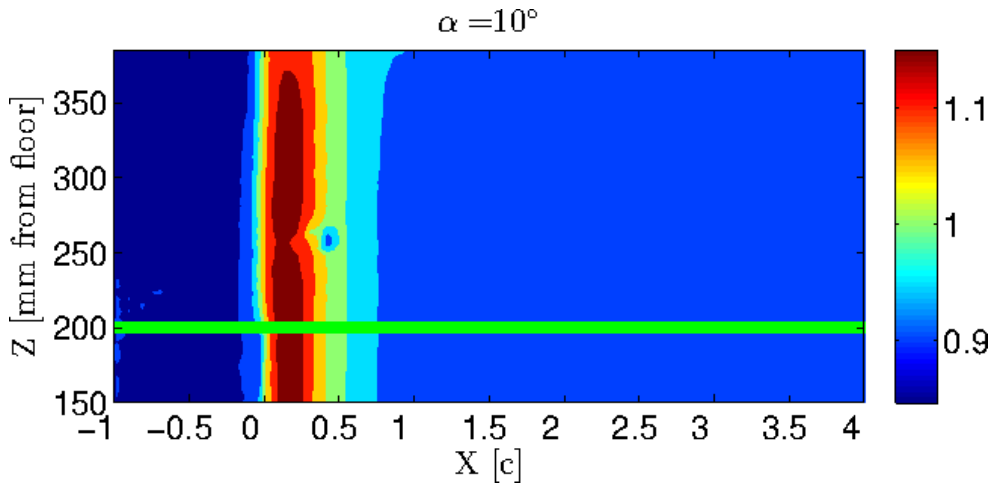

(a)

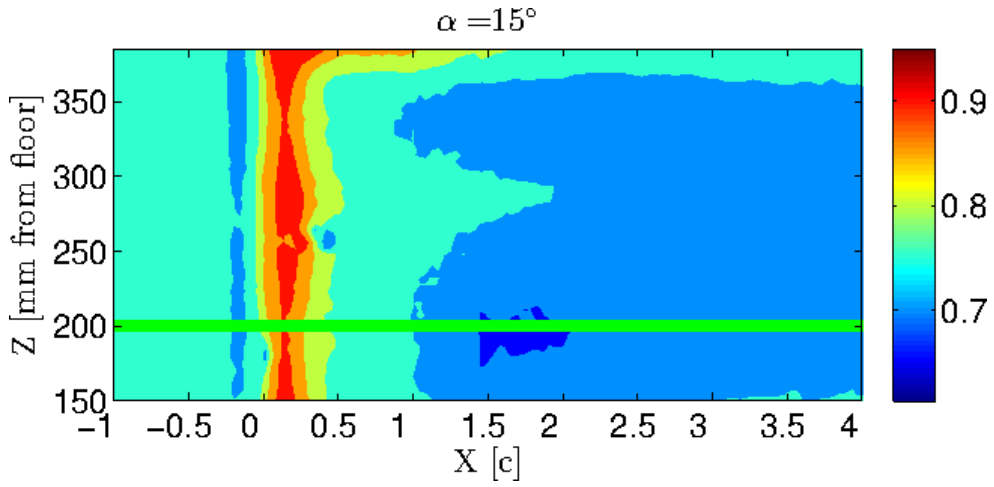

(b)

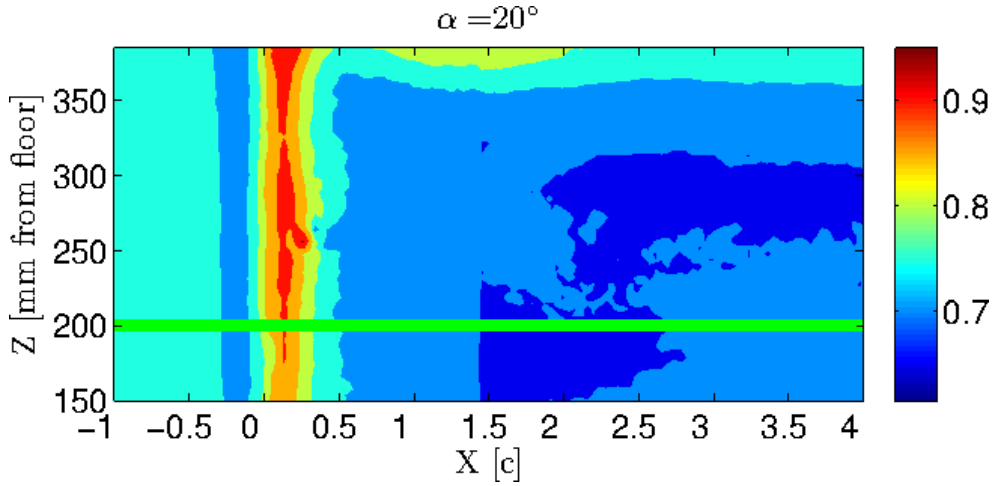

(c)

Figure 2.16: Contour plots of average u velocity, scaled by the freestream velocity $\bar{U}$, measured in x/z plane at static angles of attack on $c = 100$mm $AR = 4.6$ airfoil at $Re = 50,000$. Airfoil leading edge at $x = 0$. Water tunnel floor at $z = 0$ (units in mm), water depth 457mm. x/y measurement plane/laser at $z \sim 200$mm shown by green line on plots.

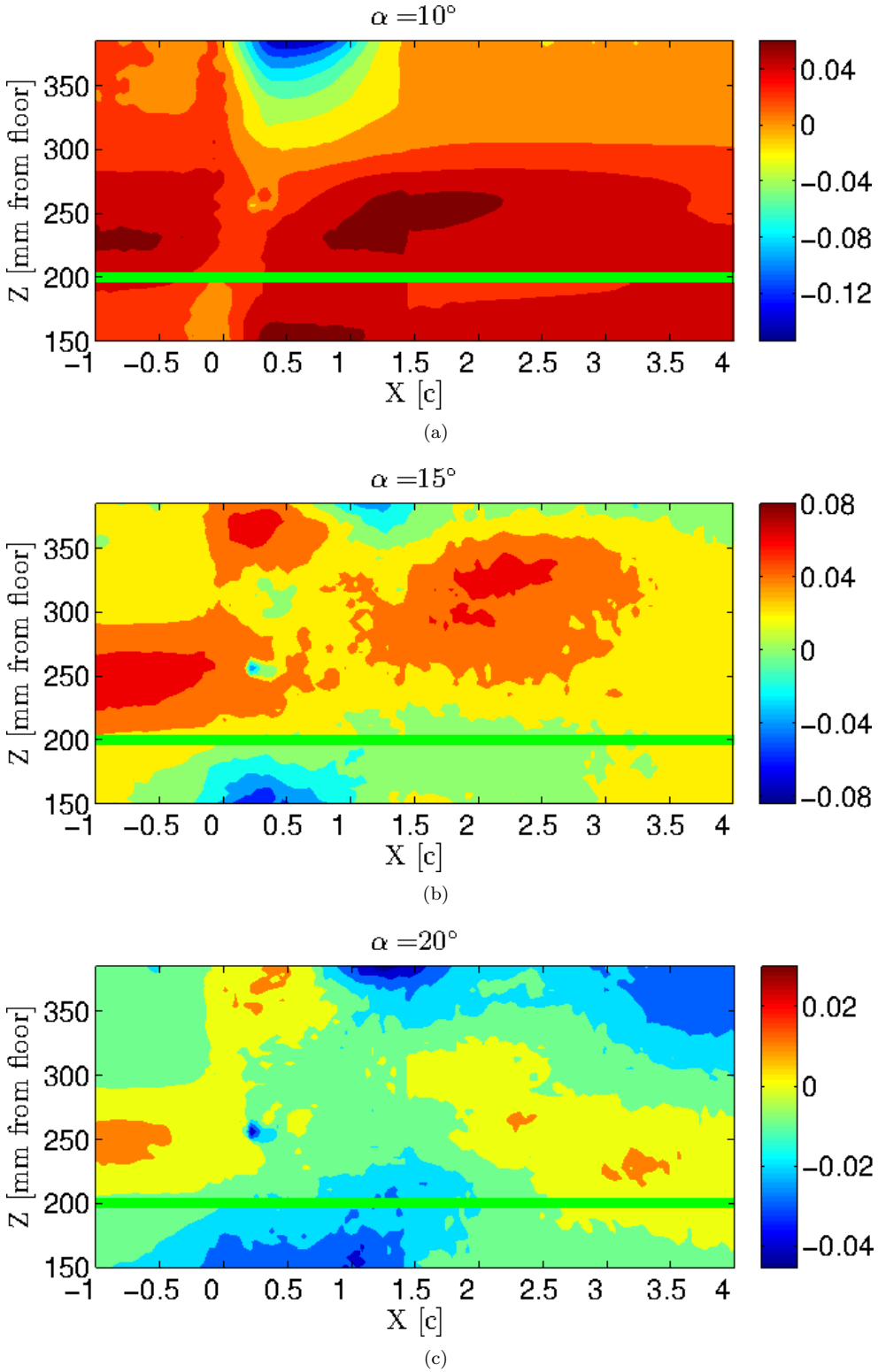

Figure 2.17: Contour plots of average w velocity, scaled by the freestream velocity $\bar{U}$, measured in x/z plane at static angles of attack on $c = 100$mm $AR = 4.6$ airfoil at $Re = 50,000$. Airfoil leading edge at $x = 0$. Water tunnel floor at $z = 0$ (units in mm), water depth 457mm. x/y measurement plane/laser at $z \sim 200$mm shown by green line on plots.

Chapter 3

Phase-Averaged Flow Around a Pitching and Surging Blade

In this chapter the flow over the combined pitch/surge airfoil motion shown in figure 1.1 will be investigated. The only data set considered is the phase averaged pitch/surge data set discussed in section 2.3.1.1. The analysis of this data set provides understanding of the most basic components of the unsteady periodic flow, by averaging out noise and flow phenomena not linked directly to the phase of the airfoil motion. Therefore, this chapter explores the physics determined solely by the periodic motion.

To provide this physical insight the dynamic stall process is investigated in detail, with an eye toward flow structure and an analysis of the separation and reattachment characteristics of the flow. Vorticity contours are used to visualize shear layer and vortex activity. Dynamic mode decomposition (DMD) as developed by Schmid (2010) is used on the velocity time series to isolate and rank periodic structures by their dynamic significance. A model using only five of the identified modes is able to capture the dynamic stall behavior and the development of the leading edge vortex. The dynamics of each of these modes are analyzed individually, and the interaction of these modes is shown to give rise to the underlying physics of dynamic stall, leading edge vortex growth and separation. As such, this simple model can easily be extended to other turbine configurations and problems in unsteady aerodynamics. The low order model we developed, as well as the physical mechanisms highlighted by this model that are shown to dominate the dynamic stall process, are the novel contribution of this chapter. This work has been published in Dunne and McKeon (2015b).

3.1 Separation evolution

A rotation cycle of the turbine consists of a pitch up and down motion, beginning at zero angle of attack and maximum surge velocity, corresponding to $\theta = 0°$ in figure 1.1 when the blade first enters the upstream (left half) of the turbine. In the upstream half of the cycle, where the turbine generates most of the power (Islam et al., 2007), the blade pitches up from 0° to 30° and back, and decelerates from maximum to minimum velocity. During this motion the flow undergoes leading edge vortex formation and dynamic stall, fully separating at $\alpha_+ \sim 25°$ on pitch up, and reattaching at $\alpha_- \sim 0$ on pitch down.

Extruding time along the z axis as in figure 2.8 and plotting an isocontour of spanwise vorticity (colored by velocity magnitude) allows the evolution of vortical structure in the flow to be visualized. Figure 3.1 shows one such isocontour over the first period of the pitch/surge motion. At zero angle of attack, point A (bottom right in the figure), the flow is attached to the airfoil, indicated by the vorticity contour following the surface of the airfoil. As the airfoil pitches up and decelerates, the location of maximum velocity magnitude moves forward until the flow separates at $\alpha_+ \sim 25°$, point B, just before maximum angle of attack and well above the static stall angle of 11.5°. Separation is defined here as the point when the shear, indicated by the vorticity isocontours, deviates from or lifts away from the airfoil surface in the y direction, thus indicating stagnant or reversed flow below the shear layer adjacent to the airfoil. After separation the vorticity is concentrated in the separated shear layer, with a constant velocity on the contour. Shortly before the return to $\alpha_- = 0°$, the flow reattaches from the leading to trailing edge at point C. From C to A' the airfoil is at negative angle of attack, and, as such, the pressure side of the airfoil is visible and the vorticity indicates the shear due to the no-slip condition at the airfoil surface. The location of points A-A' in the pitch/surge cycle can be seen in figure 3.2.

More details of the separation process are shown in figure 3.3. The approximate location of the separated region at a range of angles of attack (chosen because they most clearly show the evolution of the separation) is identified using an isocontour of the x velocity corresponding to one-quarter of the airfoil effective velocity U, $u = 0.25U$. In figure 3.3(a) the flow is still attached to the airfoil; as such the $u = 0.25U$ contour simply highlights the influence of the no-slip condition over most of the airfoil but shows the early development of slowed flow at the leading edge from the leading edge vortex. Figure 3.3(b) shows the flowfield near maximum angle of attack. The $u = 0.25U$ contour shows the separation region over the entire airfoil and extends into the wake. Finally in figure 3.3(c) the flow has reattached at the leading edge, but the contour line shows separated flow over the aft

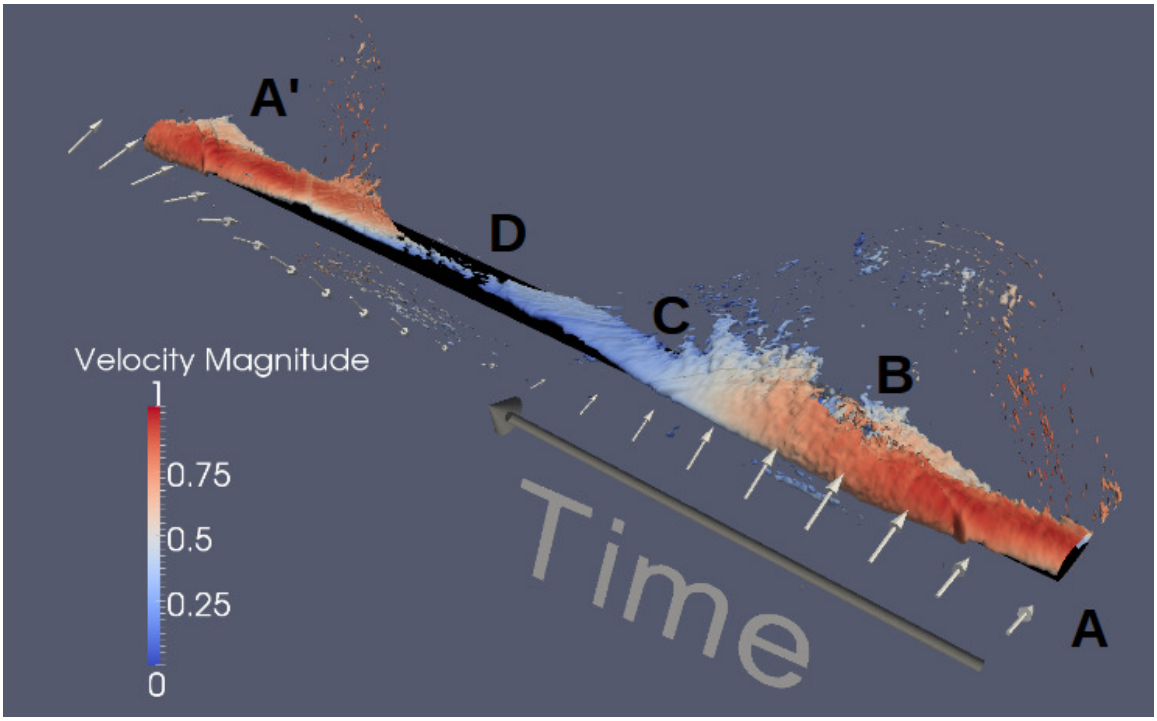

Figure 3.1: Vorticity isocontour colored by scaled velocity magnitude ($\frac{\sqrt{u^2+v^2}}{max(\sqrt{u^2+v^2})}$). 1.2 periods shown. Arrows indicate incoming angle of attack variation. Points A, A' correspond to $\alpha_+ = 0$, B to separation location, C to reattachment, D to minimum angle of attack. Note that at point D flow at and behind the trailing edge cannot be measured. The location of points A-A' on pitch/surge period showin in figure 3.2

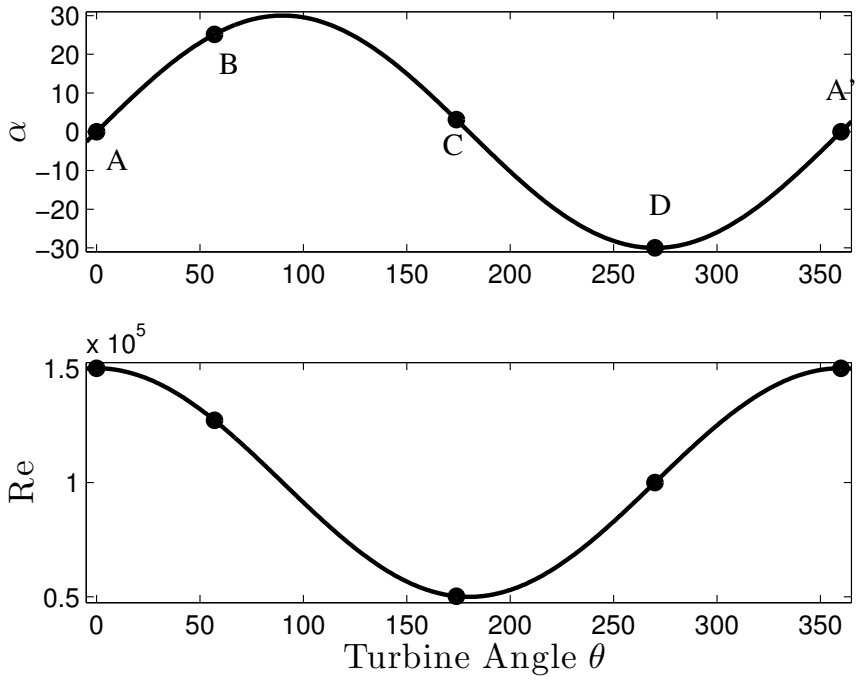

Figure 3.2: Location of points A-A' from figure 3.1 in pitch/surge cycle. Angle of attack α (top) Reynolds number (bottom).

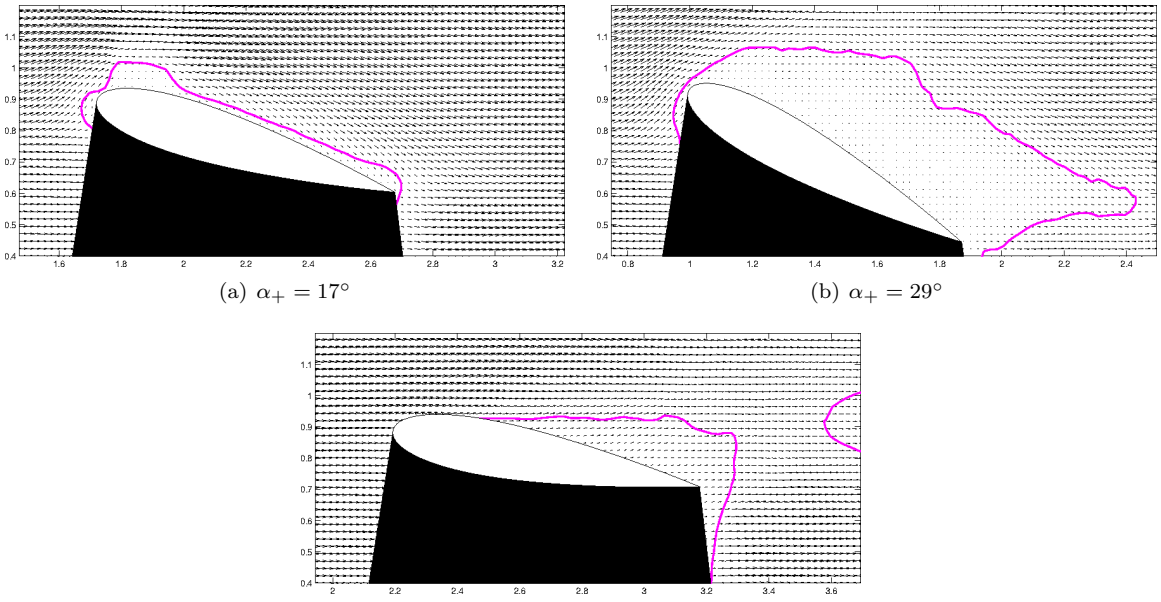

(a) $\alpha_+ = 17°$

(b) $\alpha_+ = 29°$

(c) $\alpha_- = 10°$

Figure 3.3: Vector plots in experimental field of view before and after separation. Isocontour of x velocity $u = 0.25U$ in magenta. (a) Pitch up before separation, (b) near maximum angle of attack after separation, and (c) on pitch down nearing reattachment.

three-quarters of the airfoil. The results plotted in figures 3.1 and 3.3 show clear flow hysteresis, similar to Müller-Vahl et al. (2015), with full leading edge separation on pitch up at $\alpha_+ \sim 25°$, and complete reattachment during pitch down at $\alpha_- \sim 0°$.

Figures 3.4 and 3.5 show expanded views of the vorticity in the vicinity of key changes in the structure of the vorticity isocontour of figure 3.1. The first clear structural change in the shape of the vorticity isocontour preceding separation is the split between leading and trailing edge vorticity visible near the bottom of figure 3.4 at point β, as well as the emergence of a trailing edge vortex with the opposite sense of rotation. Prior to β the isocontour identifies the shear due to the no-slip condition at the airfoil surface. However, at β this initial isocontour retracts forward from the trailing edge, and a new structure appears at the trailing edge and convects downstream. As the airfoil pitches up these structures continue to diverge, the leading edge structure moving forward until it lifts from the airfoil, indicating separation at point B, and the trailing edge structure moving aft and then disappearing at separation. The trailing edge vortex, shown in red, is also visible after point β, remaining slightly past the separation point and dissipating after the maximum angle of attack when the separated shear layer reaches the trailing edge.

As the airfoil pitches up, nearing separation, the growth of the isocontour, projecting further below and in front of the airfoil, indicates the presence of a leading edge vortex. This growth

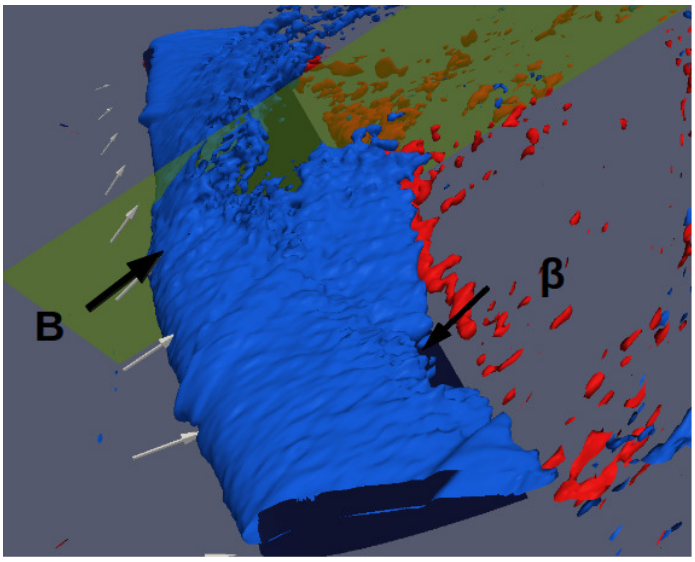

Figure 3.4: Expanded view of the vorticity isocontour from figure 3.1 leading up to separation. Clockwise vorticity in blue, counter-clockwise in red. The emergence of a trailing edge vortex is apparent at point β. Point B indicates separation location just before maximum angle of attack (denoted by the green sheet).

continues until separation at point B, as can be seen in figure 3.5. After separation the LEV convects downstream, and the vorticity isocontour lines up with the separated shear layer between the recirculation region above the airfoil and the freestream. These results are in good qualitative agreement with the evolution presented by Simão Ferreira et al. (2009) at specific angles, including LEV and TEV formation and shedding.

3.2 Low-order model from dynamic mode decomposition

The dynamic separation process described above is amenable to representation by a low order model consisting of just a few dynamic modes. In order to perform dynamic mode decomposition in the airfoil reference frame, the largest possible airfoil fixed bounding box was selected from the upper side of the airfoil in figure 2.7(a) so that the airfoil shadow did not influence results. The extent of this box can be seen in figure 3.6. Due to the significant motion of the field of view around the airfoil, the bounding box was limited to one chord length in the x direction and one-quarter chord length in the y direction and includes the flow over the front 60% of the airfoil. The time series was sub-sampled by a factor of four ($\Delta t = 1/20$ s^{-1}) for numerical stability.

Transformed DMD mode eigenvalues λ, scaled by pitch/surge frequency Ω, are plotted in figure 3.7, where on the x axis λ_r is the real part of λ representing the modal growth rate, and on the y

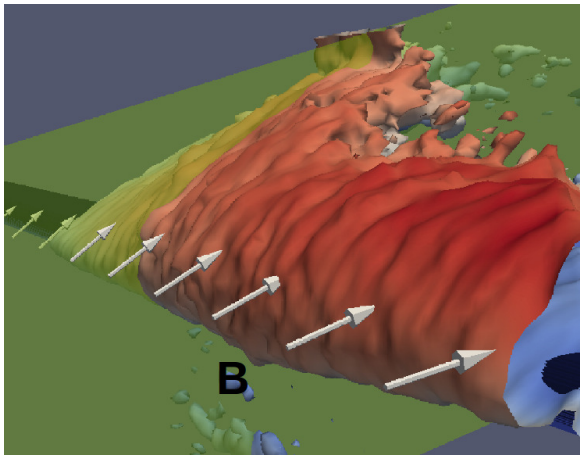

Figure 3.5: Expanded view of the leading edge vorticity isocontour from figure 3.1 during pitch up, with the maximum angle of attack indicated by the green sheet. The vorticity isocontour retreats around the airfoil leading edge until separation at point B. Vorticity isocontour, colored by scaled velocity magnitude, as in figure 3.1.

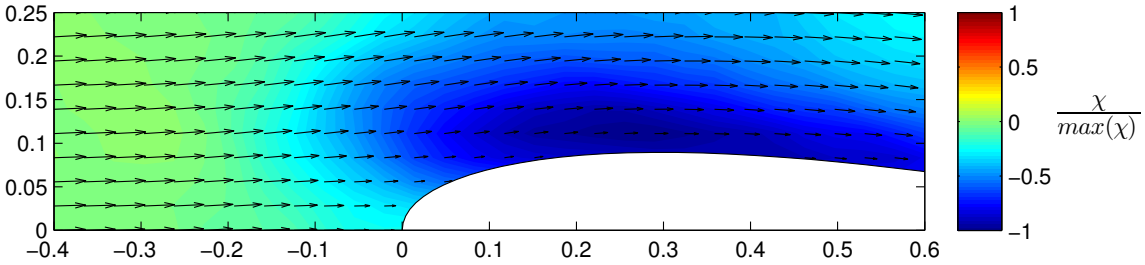

Figure 3.6: Velocity (vectors) and vorticity (contour), scaled by maximum modal vorticity, plots of time constant $\lambda_i = 0$ mode in airfoil-centered frame from a single DMD mode. Incoming flow and the diffuse vorticity associated with flow curvature around the airfoil are captured.

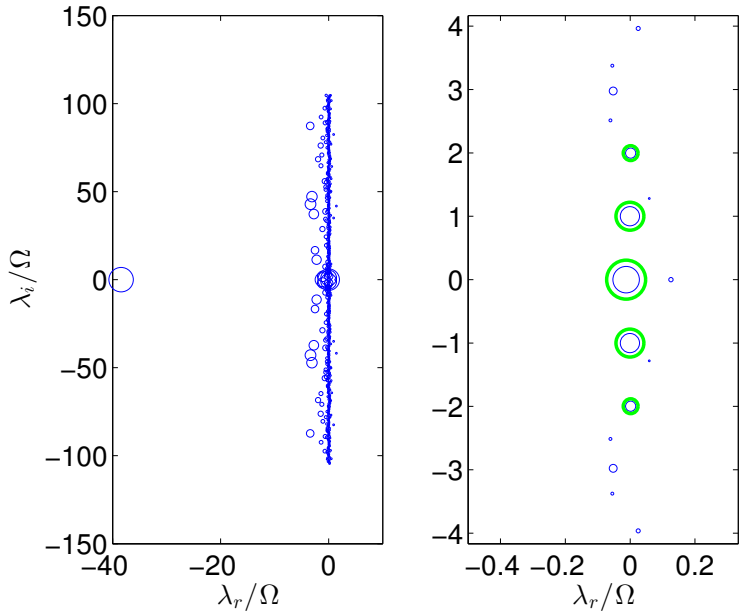

Figure 3.7: Modes calculated with DMD scaled by pitch surge frequency Ω. λ_r growth rate λ_i frequency. Point size scaled by the magnitude of the spatial structure, a. Left full spectrum, right zoomed in on strong, non-decaying modes. Modes circled in green used for further analysis.

axis λ_i is the imaginary part representing the modal frequency. The size of the points is scaled by the modal amplitude a_j to highlight the modes with a large effect on the flow field. As evident in figure 3.7 the majority of the modes cluster about the imaginary axis, thus representing the periodic, zero temporal growth modes to be expected in phase averaged measurements. Strongly decaying modes (to the left of the imaginary axis) are not expected to be physically relevant for this data set, as decaying modes should be removed by the phase averaging process, and are likely the result of experimental variation and a consequence of the limited number of datasets. The zero frequency mode with a very high decay rate $\lambda_r \sim -40$, with a very large a value indicated by its large size in the far left of figure 3.7, decays almost completely in one timestep and accounts for the variation due to noise in the first two timesteps. Using the improved algorithm developed by Hemati and Rowley (2015) may remove some of these spurious decaying modes, by eliminating the effect of noise. Zooming in on the modes with strong amplitudes, as shown in the right of figure 3.7, shows a very strong base flow with $\lambda_r \approx \lambda_i \approx 0$, a mode pair at the pitch/surge frequency $\lambda_i \approx \pm 1\Omega$, another at $\lambda_i \approx \pm 2\Omega$ highlighted in green, as well as a smaller, less significant pair of modes at $\lambda_i = \pm 3\Omega$.

Figure 3.8 shows a comparison of the full flow field (left) and a reconstruction of the flow using the highlighted five modes (base flow plus frequencies at 1 and 2Ω) (right). Such a model, using five modes and three associated frequencies (time-constant as well as two conjugate pairs), is the

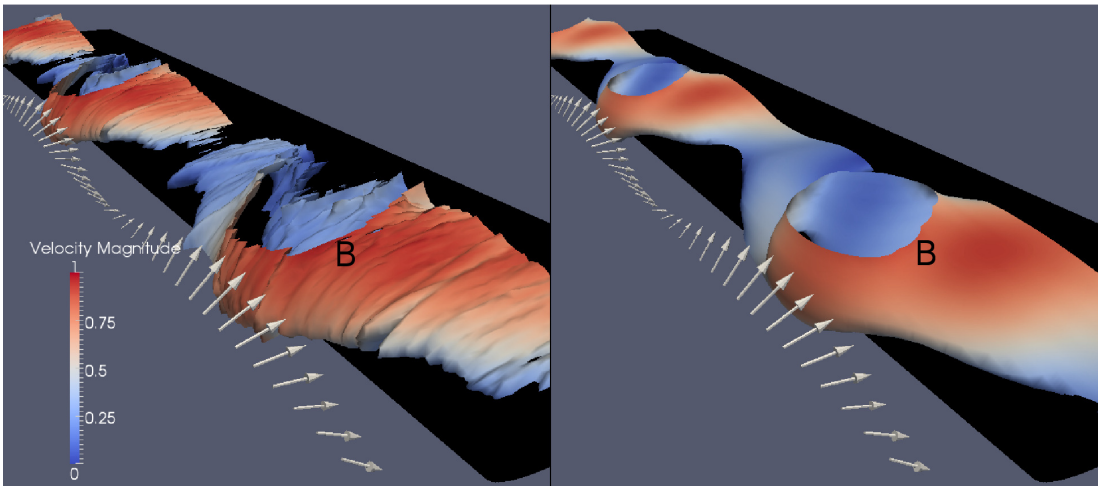

Figure 3.8: Isocontour of vorticity (colored by scaled velocity magnitude) of data (left) and five-mode DMD reconstruction (right) for entire data set. Reconstruction captures primary behavior of flow.

minimum order model that can capture the differences between pitch up and down inherent in dynamic stall. A three-mode model, including only a single conjugate pair and a time-constant mode could, in principle, reproduce the differences between suction and pressure sides; however, the flow field would be, by definition, identical on pitch up and pitch down. Thus, such a model would be unable to capture the complete physics.

Qualitatively, this five-mode reconstruction closely mimics the flow full flow field (over 500 modes). Including higher order harmonics of Ω causes negligible change in the reconstructed flow field. During pitch up, the five-mode model captures the growth of the leading edge vortex in the vorticity contour around the leading edge. At point B, a recirculation region forms behind the airfoil when the flow separates and the isocontour follows the separated shear layer. Due to the grid used for the DMD model this shear layer leaves the measurement domain, resulting in the top of the true isocontour being truncated after point B. Finally, the model captures the reattachment point near $\alpha_- = 0$ when the isocontour again highlights vorticity at the airfoil surface. The only clear difference between the full flow and the five-mode model, apparent in figure 3.8, is high frequency variation in the full flow isocontour that is the result of non-phase averaged behavior not fully removed in the averaging process and/or higher harmonics of the pitch/surge frequency.

3.2.1 Leading edge vortex circulation

To quantitatively compare the five-mode model to the full flow, the development of the leading edge vortex was analyzed. The leading edge vortex structure is identified using the Γ_1 and Γ_2 criteria

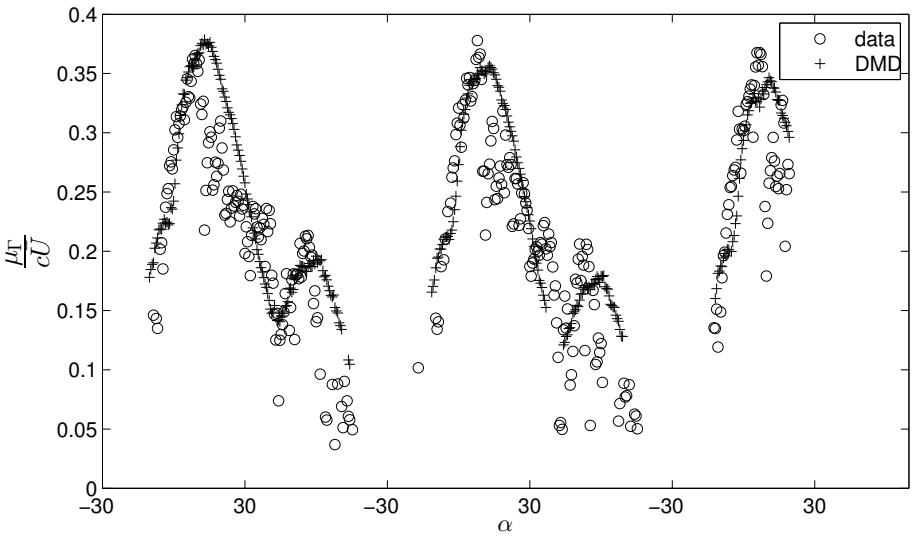

Figure 3.9: Normalized circulation within leading edge vortex of five-mode DMD model (+) and data (o). Plotted against airfoil angle of attack, α.

developed by Graftieaux et al. (2001) as discussed in Chapter 2. The circulation μ_Γ normalized by the mean velocity $\bar{U}$ and the chord length c for both the five mode DMD model and the original data is plotted in figure 3.9. Clearly the five mode DMD model does a very good job of replicating the LEV circulation, capturing both the shape and the magnitude. The peak in circulation appears just before separation $\alpha_+ \sim 25°$ when most of the vorticity is contained within the vortex at the leading edge. After separation, vorticity follows the shear layer, extending outside the DMD domain, and circulation decreases. The second peak that appears in both the data and DMD reconstruction occurs near reattachment when rotational flow once again begins to follow the airfoil surface, and is contained within the vortex boundary.

3.2.2 Modal breakdown

While the DMD model is quite simple, each mode captures phenomena relevant to the flow field arising from VAWT rotation. The zero frequency mode was shown in figure 3.6. It represents a time-constant base flow with zero angle of attack and diffuse vorticity due to the curvature of the flow around the airfoil and shear in the boundary layer.

The first complex conjugate pair at pitch/surge frequency Ω includes the velocity and angle of attack variation caused by the pitch and surge motion. In figure 3.11 the first mode is plotted with the instantaneous surge velocity subtracted, in order to make visual identification of the vortical structure in the mode more clear. Increased negative vorticity during pitch up and positive vorticity

during pitch down suggests the presence of vortex structure in the mode with counter clockwise rotation during pitch up and clockwise during pitch down. The formation of a counter-clockwise vortex above the leading edge as visible in figure 3.11(a). As the airfoil is pitched up, this vortex convects downstream, as seen in figure 3.11(b). Congruent with a periodic process, on pitch down a vortex of the opposite sign vorticity is formed and convects downstream on the pressure side of the airfoil (Figs. 3.11(d)-3.11(e)). The location of each figure within the pitch/surge cycle is shown in figure 3.10.

The behavior of the dynamic mode at twice the pitch/surge frequency is shown in figure 3.12. The period of this mode is half that of the airfoil motion, and thus a full mode cycle takes place on the suction side of the airfoil $\alpha \geq 0$. Less clear to see in vorticity, due to the resulting weaker structure but visible in the vector plot, a vortex rotating in a clockwise direction (negative vorticity) nucleates at the leading edge and convects downstream along the shear layer during pitch up, figures 3.12 (a, b and c), while a counter-clockwise vortex appears on pitch down in figure 3.12(d).

As shown in the schematic of figure 3.13, the behavior of DMD modes at one and two times the pitch/surge frequency suggests interacting primary and secondary separation modes. The relative amplitude and phase of these modes is plotted in figure 3.14. The primary mode (figure 3.13(a)), with maximum amplitude at $\alpha_+ = 0°$, corresponds to a clockwise vortex that forms at the leading edge at $\alpha_+ \sim -5°$ during the pitch up and convects downstream, lifting the streamline from the surface and leading separation. On pitch down the opposite signed vortex appears at $\alpha_- \sim 5°$ and lags the reattachment, convecting downstream on the pressure side of the airfoil. The secondary mode (figure 3.13(b)) includes a similar clockwise vortex that appears before the second mode peaks at $\alpha_+ = 15°$ and convects downstream after separation along the separated shear layer. The corresponding counter-clockwise vortex appears at the leading edge around $\alpha_- \sim 17°$ before reattachment then convects downstream, pushing the streamline back to the airfoil surface, leading reattachment from the leading edge forward as seen in figures 3.1 and 3.3.

In this way the phase relationship between primary and secondary modes gives rise to the flow physics involved in dynamic stall. Linear superposition of the DMD modes gives an accurate representation of the velocity, but the effect is more complicated in the vortex and shear layer structure shown previously. On pitch up the primary separation mode leads, peaking at $\alpha_+ = 0°$, followed by the secondary mode, peaking at $\alpha_+ = 15°$; thus, as the clockwise vortex associated with the first mode convects downstream, it is enhanced by the secondary mode, also a clockwise vortex, lifting the streamline from the airfoil and forcing the flow to separate. On pitch down the secondary

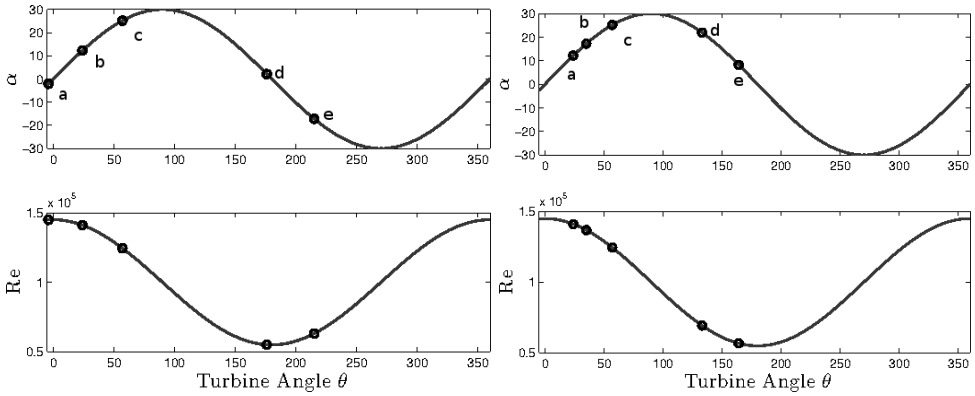

Figure 3.10: Location of plots a-e on pitch surge cycle for first (a) and second (b) mode pairs in figures 3.11 and 3.12, respectively.

mode peaks first at $\alpha_{-} = 15°$, and the corresponding counter clockwise vortex forms and convects downstream, driving the reattachment process, as seen from the leading edge back, followed by the peak of the primary mode at $\alpha_{-} = 0°$.

The phase relationship also explains the different behavior on the pressure and suction side of the airfoil. On the suction sides ($0^o \leq \alpha \leq 30^o$ for the side of the airfoil measured in the PIV experiments), the primary and secondary modes interact constructively, allowing for dynamic separation and reattachment. On the pressure side of the airfoil ($0^o \geq \alpha \geq -30^o$), primary and secondary separation modes act in the opposite direction, and the effect of each mode counters the other. Destructive interference between these two modes results in a weaker combined effect on the base flow, maintaining attached flow on the pressure side, while angle of attack and velocity variation are preserved.

The periodic blade trajectory, with a fixed frequency due to the geometry of a vertical axis wind turbine, makes the flow amenable to this simple model. The time-resolved data, with a fixed sinusoidal frequency as measured using the simplified motion in this study, allows flow content at only zero, one, and two times the motion frequency, as captured by the dynamic mode decomposition, to model the dynamics of the flow. The mean mode accounts for the rotation due to the geometry of the airfoil, and shear due to the boundary layer. The mode at the motion frequency accounts for the time-dependent incoming velocity and angle of attack, and the interplay between modes at the first two harmonics of the pitch/surge frequency is able to capture LEV growth and the hysteresis inherent in dynamic stall. Furthermore, measurement of the symmetric NACA 0018 airfoil means that the flow on both pressure and suction sides of the airfoil can be understood by this model,

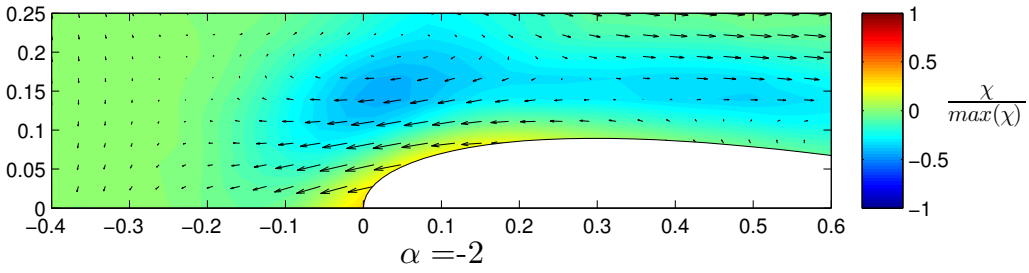

(a) First DMD conjugate pair without surge component $\alpha_+ = -2$ on pitch up.

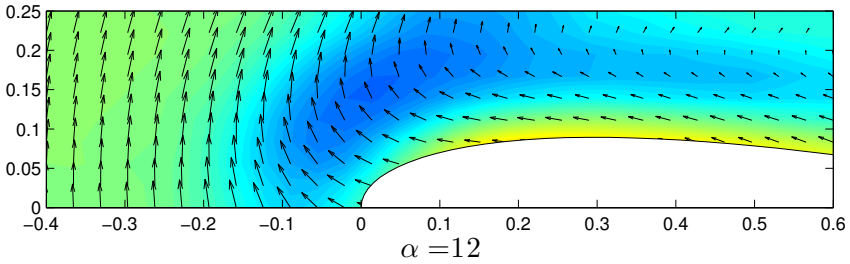

(b) First DMD conjugate pair without surge component $\alpha_+ = 12$ on pitch up.

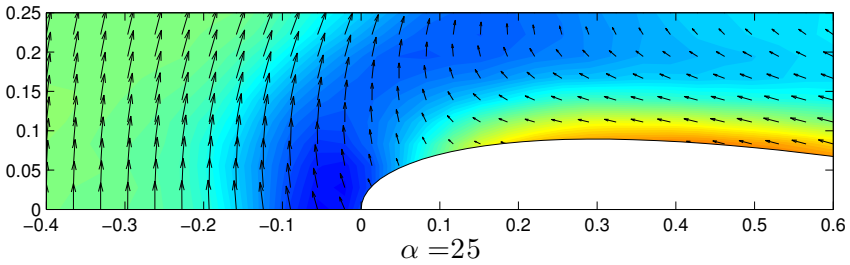

(c) First DMD conjugate pair without surge component $\alpha_+ = 25$ on pitch up.

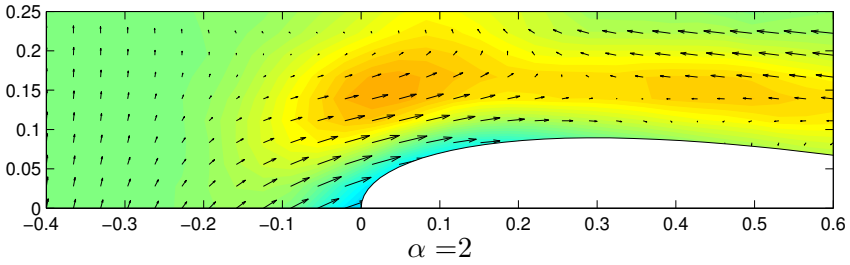

(d) First DMD conjugate pair without surge component $\alpha_- = 2$ on pitch down.

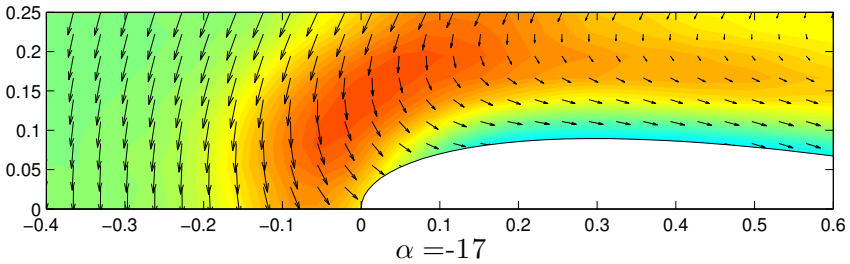

(e) First DMD conjugate pair without surge component $\alpha_- = -17$ on pitch down.

Figure 3.11: Velocity and vorticity (scaled by maximum modal vorticity) plots of first DMD conjugate pair at pitch/surge frequency Ω with the freestream velocity variation from surge removed. Vortex structure at leading edge apparent in figures a and e. Maximum velocity magnitude ($\sqrt{u^2+v^2}$) 83% of freestream velocity $\bar{U}$.

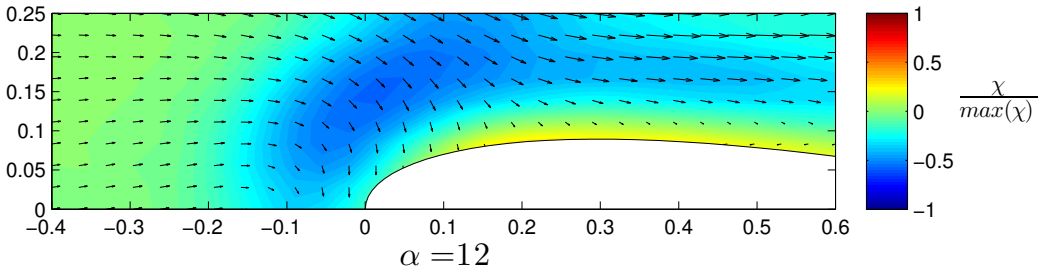

(a) Second DMD conjugate pair $\alpha_+ = 12$ on pitch up.

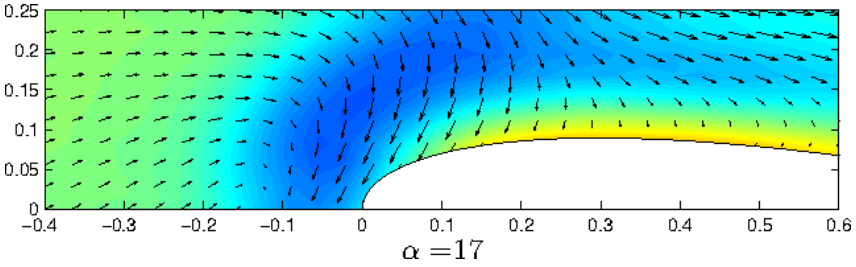

(b) Second DMD conjugate pair $\alpha_+ = 17$ on pitch up.

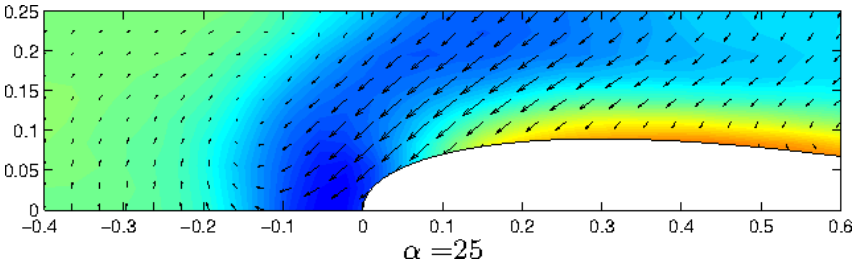

(c) Second DMD conjugate pair $\alpha_+ = 25$ on pitch up.

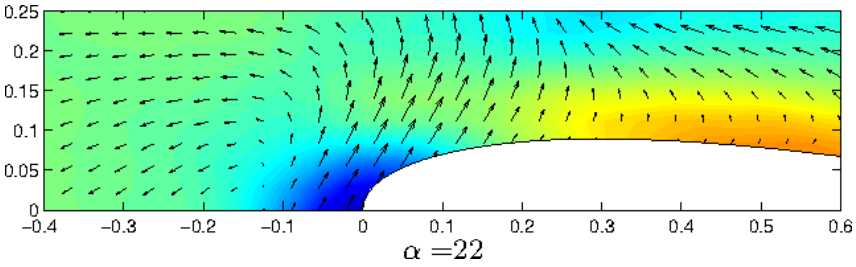

(d) Second DMD conjugate pair $\alpha_- = 22$ on pitch down.

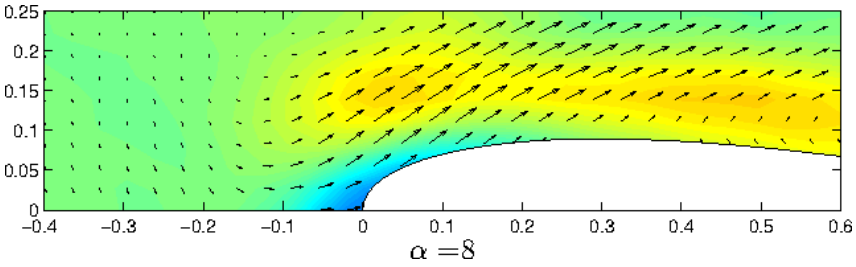

(e) Second DMD conjugate pair $\alpha_- = 8$ on pitch down.

Figure 3.12: Velocity and vorticity (scaled by maximum modal vorticity) plots of second DMD conjugate pair at twice pitch/surge frequency 2Ω. Maximum velocity magnitude ($\sqrt{u^2 + v^2}$) 30% of freestream velocity $\bar{U}$.

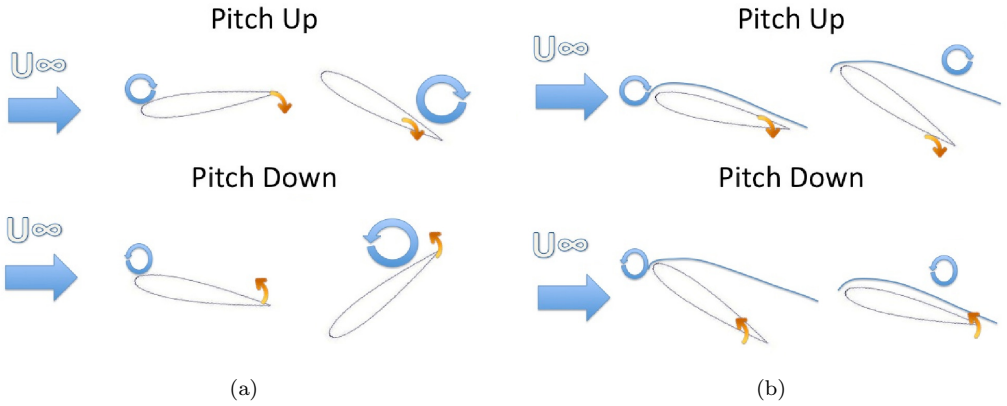

Figure 3.13: Schematics of the primary (a) and secondary (b) separation modes at first and second harmonic of pitch/surge frequency Ω. Vortex in the primary mode leads separation and lags reattachment, vortex in secondary mode lags separation convecting along the shear layer, and leads reattachment.

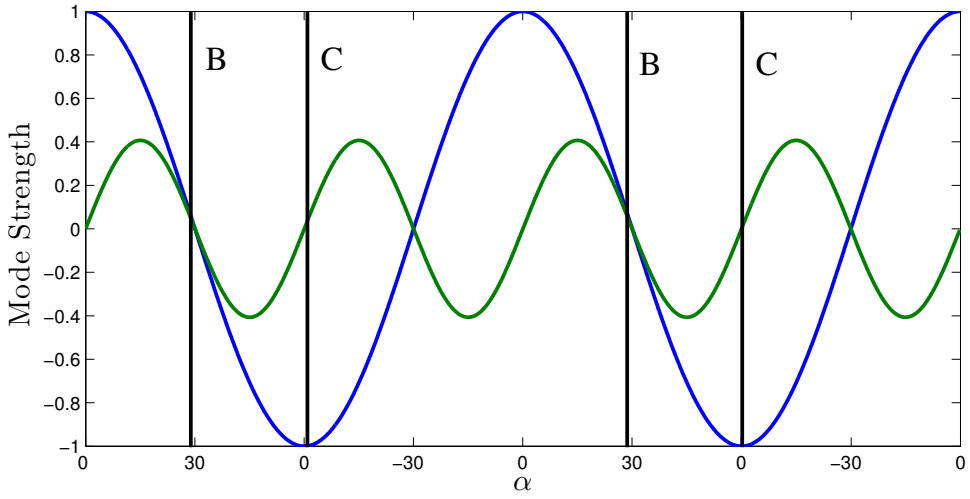

Figure 3.14: Primary (blue) and secondary (green) separation mode strengths over 2 airfoil cycles. Lines at separation and reattachment points B and C. Modes interact constructively on the suction side of airfoil ($0 \leq \alpha \leq 30$) and destructively on the pressure side ($0 \geq \alpha \geq -30$).

and the destructive interference between first and second harmonic modes maintains boundary layer attachment over the pressure side of the airfoil. This model therefore captures the dynamic stall process inherent due to the geometry of a VAWT in the most efficient way. Since this model is directly related to the inherent physics of LEV formation, it can naturally be extended to turbines operating under different conditions, including frequency, angle of attack variation, and Reynolds number, fixed by the tip speed ratio η, as long as the flow still exhibits dynamic stall.

3.3 Summary and conclusions

The data set of phase-averaged measurements on the combined pitching and surging airfoil are investigated in this chapter to determine the basic dynamic stall and reattachment behavior of the flow. Vorticity contours were shown to follow the airfoil surface up to very high angle of attack $\alpha_+ \sim 25°$, indicating attached flow well above the static stall angle. Above $\alpha_+ = 25°$ the flow separates, prior to the maximum angle of attack. The flow remains separated until the airfoil approaches zero angle of attack on pitch down, when it reattaches.

A low order model of this flow over the leading edge was assembled with five modes identified using dynamic mode decomposition (DMD). These modes have negligible growth rate, as appropriate for periodic motion, and include a time-constant base flow mode as well as two complex conjugate modes at one and two times the pitch/surge frequency. This model reduces the flow field from over 500 modes to five and captures the full dynamic stall behavior of the phase-averaged velocity field. The growth of a vortex at the leading edge is captured as well as the point of flow separation, reattachment and the general shape of the shear layer on the airfoil during attached and separated flow. Furthermore, the circulation within the leading edge vortex was calculated for the model and the flow field, and shown to be nearly identical.

Decomposing the flow field into a mean and two mode pairs provides insight into the mechanism of dynamic stall. Such a five-mode, three-frequency model encompasses the minimum number of frequencies to capture the inherent flow physics. The mode pair at the airfoil frequency first captures velocity variation necessary to reproduce the freestream velocity and angle of attack change inherent from the pitch surge motion. Additionally, this mode includes a vortex structure growing near the leading edge that acts to lift the streamline away from the airfoil and lead separation. The second mode pair, at twice the airfoil frequency, induces a similar vortex structure. During pitch up this vortex rotates in the same direction as that of the first mode, lagging separation, and strengthening the shear layer. On pitch down the vortex rotation is in the opposite direction, and, as it convects

downstream, it drives reattachment from the leading edge forward.

The phase relationship between these two modes gives rise to the hysteresis inherent in the flow. On the suction side of the airfoil ($\alpha > 0°$) the modes act constructively, providing separation and subsequent reattachment. On pitch up ($\alpha_+ \geq 0°$) the primary mode peaks before the second mode driving the LEV growth and separation. On pitch down ($\alpha_- \geq 0°$) the secondary mode leads, resulting in a differing flow field, and driving reattachment. Destructive interference of the two modes on the pressure side of the airfoil ($\alpha < 0$) maintains attached flow, while capturing the inherent velocity variation. This simple five-mode model accurately decomposes the complex physics of dynamic stall, with each mode pair modelling different physical phenomenon that give rise to leading edge vortex formation, separation, and reattachment.

Modeling angle of attack and Reynolds number variation in the linear frame led to the identification of the importance a timescale associated with the vertical axis wind turbine configuration. This timescale, related to the rotation frequency of the turbine, corresponds to the physical mechanisms responsible for the dynamic separation and reattachment process. As such, these mechanisms, identified by the five-mode model for the VAWT blade, can be extended to general periodic motions, including large angle of attack variation and resulting dynamic stall. Tuning of this model to specific frequencies would allow this extension to capture a wide range of unsteady flows that exhibit leading edge vortex development, shedding, and separation linked to the airfoil motion frequency.

Chapter 4

Flow Timescales in Dynamic Stall

In this chapter, flow phenomena associated with different physical timescales are investigated to determine their effect on the dynamic stall process. Both the phase-averaged and instantaneous combined pitch/surge data sets from sections 2.3.1.1 and 2.3.1.2 are considered in detail. This timescale analysis provides insight into the forcing frequencies that appear on VAWTs and highlights the physical processes that determine the location in the motion period, or position θ of the turbine, where vortex shedding, dynamic stall, and reattachment take place.

The first timescale identified in this flow is the timescale associated with the pitch/surge period $\frac{1}{\Omega}$ determined by the rotational frequency of the turbine. This timescale determines the reduced frequency k of the unsteady flow and sets the base periodicity of the motion shown to determine the flow evolution in the previous chapter as well as by Baik et al. (2012), Rival et al. (2009), and others. The second fundamental timescale investigated is related to the formation growth and shedding of the leading edge vortex. The time this vortex takes to nucleate and grow determines the phase within the pitch/surge motion at which large vortices are shed from the airfoil, as well as affecting the variation of forces on the blade (Choi et al., 2015). The final time scale investigated is the flow phenomenon not directly linked to the phase of the motion, but instead dominated by the interaction of the blade geometry and the variation of the blade relative freestream velocity. The interaction of these timescales and their development on a VAWT blade are the primary contributions of this chapter.

4.1 Timescale I: Pitch/surge period

The period of rotation of the turbine $\frac{1}{\Omega}$ and the turbine geometry set the reduced frequency of the equivalent pitch/surge motion considered here as $k = 0.12$, which determined the base forcing

frequency on the turbine. The model developed and validated in Chapter 3 demonstrates that the averaged flow field of the combined pitch/surge flow including the dynamic stall phenomenon can be captured using simply the first two harmonics of the pitch/surge frequency. While these primary and secondary separation modes model the physics of the flow, including leading edge vortex formation, their relationship determines the phase in the airfoil motion where separation and reattachment take place. LEV separation and stall occur before the change in direction of the maximum angle of attack and thus an additional physical mechanism, beyond the pitching/surging motion, determines the modal phase relationship that results in the point of dynamic stall.

4.2 Timescale II: Leading edge vortex formation

To investigate the development leading edge vortex in detail, the Γ_1 and Γ_2 vortex tracking method described in section 2.4.1 was implemented on the phase-averaged pitch/surge data set from section 2.3.1.1. The circulation u_Γ normalized by $\bar{U}$ and c, equivalent diameter ($D_{eq} = \sqrt{\frac{4A}{\pi}}$), and x and y location of the leading edge vortex is plotted for half a pitch up/pitch down period ($\alpha \geq 0$) in figure 4.1, where A is the area of the vortex. Four distinct regimes of leading edge vortex growth are apparent from these plots, separated by black lines at points A, B, C, Φ and Ψ, which are shown relative to the phase of the pitch/surge motion in figure 4.2. Points A, B, and C correspond to $\alpha_+ = 0°$, separation, and reattachment, as in section 3.1 and figure 3.1. Refer to figure 2.4 for the pitch velocity and acceleration during these regimes. Changes in the LEV structure characterized by the $\Gamma_2 = 2.2/\pi$ isocontour (figure 4.3) correspond to the same regimes identified in figure 4.1. Locations in figure 4.3 where no vortex contour is shown (most notably near points B and Φ) occur when the strict criteria of both $\Gamma_2 < 2/\pi$ and $\Gamma_1 \geq 0.7$ are not met.

4.2.1 Attached flow regime

Between points A and Φ the flow is fully attached to the airfoil surface. The Γ criteria pick up streamline curvature due to the shape of the airfoil surface, suggesting that the flow is behaving quasi-statically and no LEV is present. In this regime the location of maximum Γ_1, indicating the center of the rotational flow, remains at $y \sim 0.18c$ or approximately one airfoil thickness from the chordline. The core of this rotational region is seen to move forward in x as the flow is rotated more and more strongly at the leading edge. The circulation and diameter of this region initially increase together as more and more rotation occurs at the surface of the airfoil to maintain attached flow

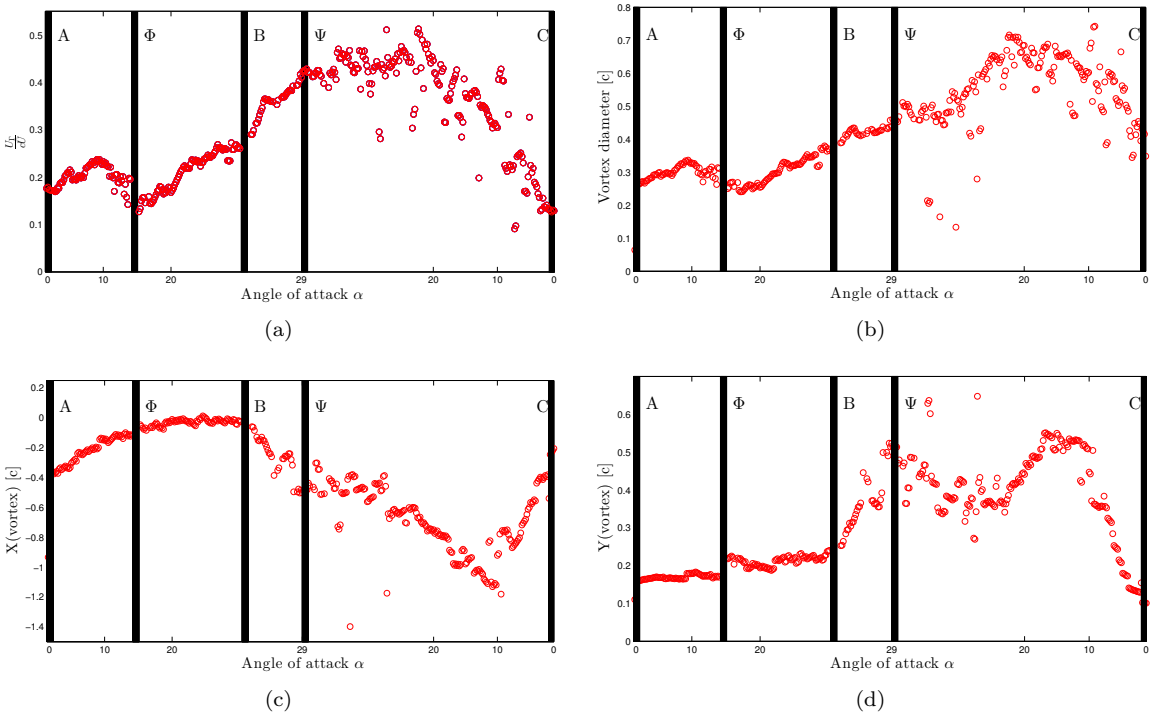

Figure 4.1: Leading edge vortex circulation, diameter, and position over half a pitch up/down cycle $\alpha \geq 0$.

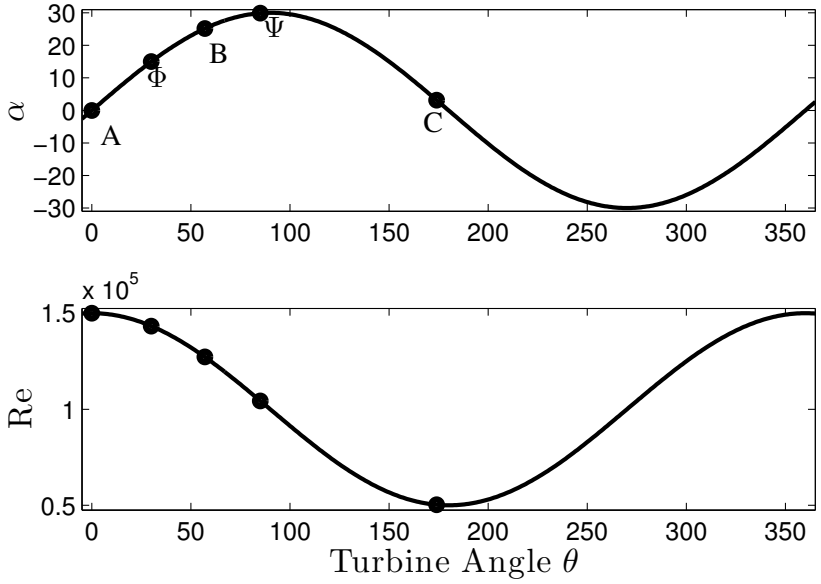

Figure 4.2: Location of points A-A' from figure 3.1 in pitch/surge cycle. Angle of attack α (top) Reynolds number (bottom).

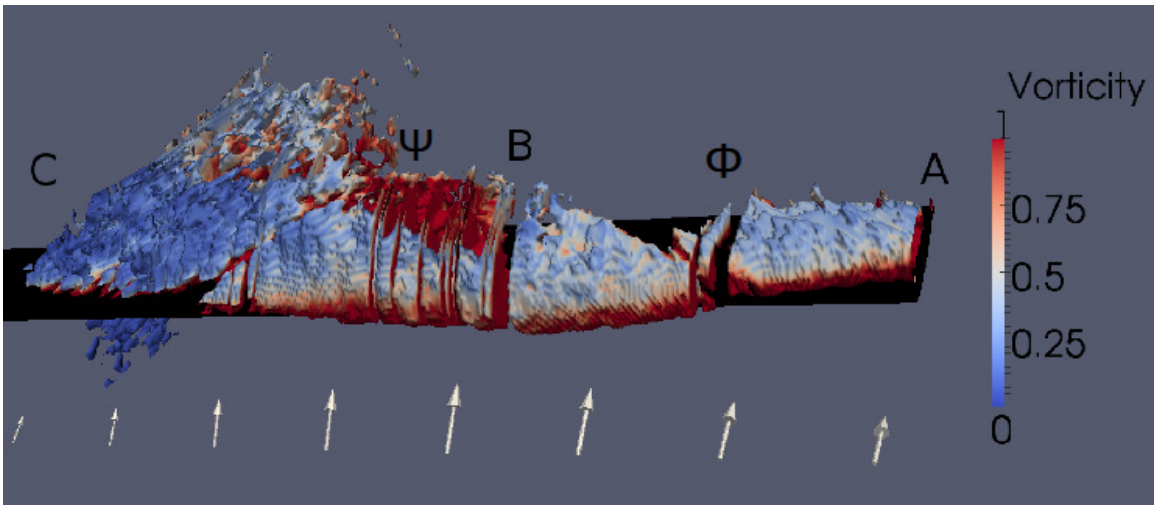

Figure 4.3: $\Gamma_2 = 2.2/\pi$ contour of identified leading edge vortex colored by vorticity. Positive angle of attack half of pitch/surge period shown. Time shown from right to left to provide best angle to view vortex structure.

at increasing angle of attack. As the airfoil passes $\alpha = 10°$, however, the size and strength of this region decrease as flow rotation at the leading edge begins to dominate.

4.2.2 Leading edge vortex development

At $\alpha \sim 15°$, point Φ, the leading edge vortex begins to dominate the rotation of the flow around the airfoil and is identified by the Γ criteria. This vortex can be seen from above in figure 4.3 between points Φ and B, as well as from below in figure 4.5. In this regime the core of this vortex remains in a constant position within 5% of the leading edge in x and about 0.2-.25c above the airfoil centerline in y. Initially the vortex is nearly circular just above the leading edge as seen at $\alpha_+ = 19°$ in figure 4.4 and at the beginning (left) of figure 4.5. In this regime this strong nearly circular core that contains most of the vorticity remains at the leading edge. As time progresses, however, the vortex includes the flow that rotates around the airfoil behind this core with weaker vorticity. This can be seen from above as the blue structure growing toward the trailing edge in figure 4.3, and as a thin layer extending from the top of the vortex core visible from below in figure 4.5. In this region the leading edge vortex circulation u_Γ and equivalent diameter grow linearly as more and more circulation is entrained in the LEV (figures 4.1(a) and 4.1(b)) and the weaker rotational layer behind the LEV grows toward the trailing edge.

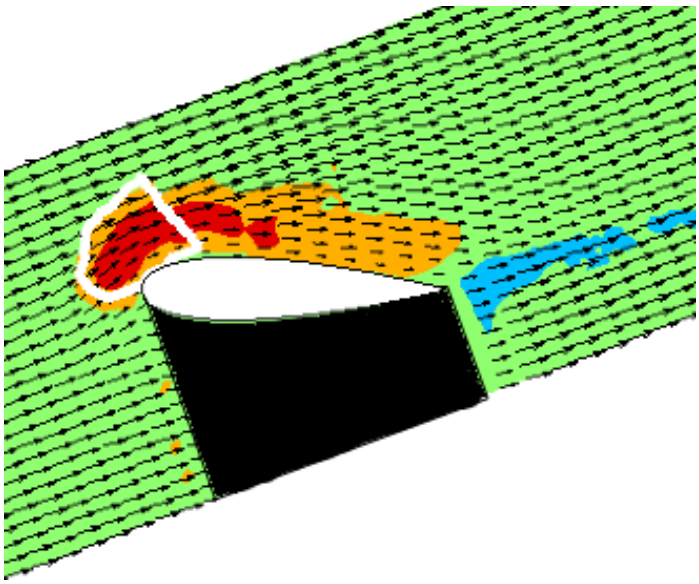

Figure 4.4: Vorticity contour with velocity vector plot near the beginning of LEV formation ($\alpha = 19°$). $\Gamma_2 = 2/\pi$ contour in white at the leading edge of the airfoil.

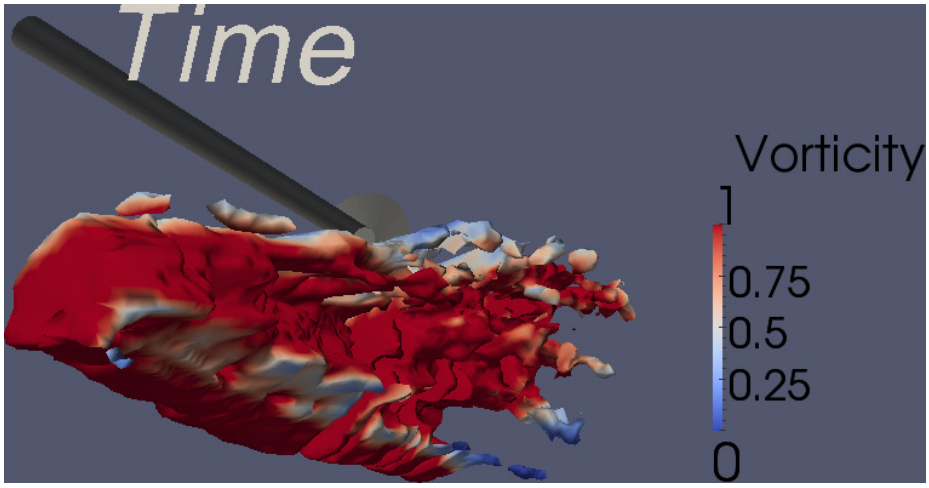

Figure 4.5: Isocontour of $\Gamma_2 = 2.2/\pi$ colored by vorticity seen from below indicating the leading edge vortex during the development regime beginning at point Φ, at the left side of the isocontour and ending at B on the right side of the contour. From this angle the primary core of the vortex can be seen as a circular structure. This structure remains just above the leading edge of the airfoil, which has been removed from the image, so the shape of the vorticity isocontour can be observed.

4.2.3 Leading edge vortex separation

At point B the strong circular core of vorticity at the leading edge that characterizes the LEV in the development regime begins to extend backward toward the trailing edge. This results in a strong vorticity signature appearing in the $\Gamma_2 = 2.2/\pi$ isocontour behind the leading edge (figure 4.3). This corresponds to the center of the vortex beginning to move toward the trailing edge and up away from the airfoil in the y direction (figures 4.1(c) and 4.1(d)). This rearward motion of LEV toward the trailing edge indicates moment stall, as defined by Carr et al. (1977). Since the vortex has begun to move back at this point and is no longer attached to the leading edge of the airfoil, point B is defined as the time when the leading edge vortex is shed.

After the vortex has shed the diameter continues to grow at the same rate as during LEV formation (figure 4.1(b)); however, the rate of circulation growth increases rapidly as the vortex convects into the shear layer (figure 4.1(a)). This apparent increase in circulation is observed because after the LEV is shed, the $\Gamma_2 \geq 2.2/\pi$ includes the vortex as well as the developing separated shear layer behind it. This increase in total circulation likely corresponds to the continuing lift increase as the LEV convects over the airfoil surface before lift stall, as defined by Carr et al. (1977). The LEV separation regime ends when the center of the vortex reaches $x_v = 0.5c$ (figure 4.1(c)) and the vortex extends all the way back to the trailing edge at point Ψ.

4.2.4 Stalled flow

Finally, after Ψ the leading edge vortex structure leaves the airfoil behind, followed by the trailing edge vortex seen in figure 3.4 and investigated by Rival et al. (2009). At this point the circulation of the vortex is no longer bound to the airfoil, and lift stall occurs (Carr et al., 1977). After lift stall, the flow is fully separated, and the Γ criteria pick up vortices in the separated shear layer. As such, the isocontour in figure 4.3 no longer shows a single coherent vortex but instead appears rough, indicating multiple smaller vortices. As the LEV convects away from the airfoil and decays, circulation plateaus and eventually drops, while the size of the rotational region increases to include large portions of the separated shear layer.

4.2.5 Non-phase averaged results

A comparison of the phase averaged data with that of a single measurement in the front field of view, during vortex development, and after vortex shedding (figure 4.6) show similar general behavior, but smaller structure in the instantaneous measurement that is removed with phase averaging. This effect

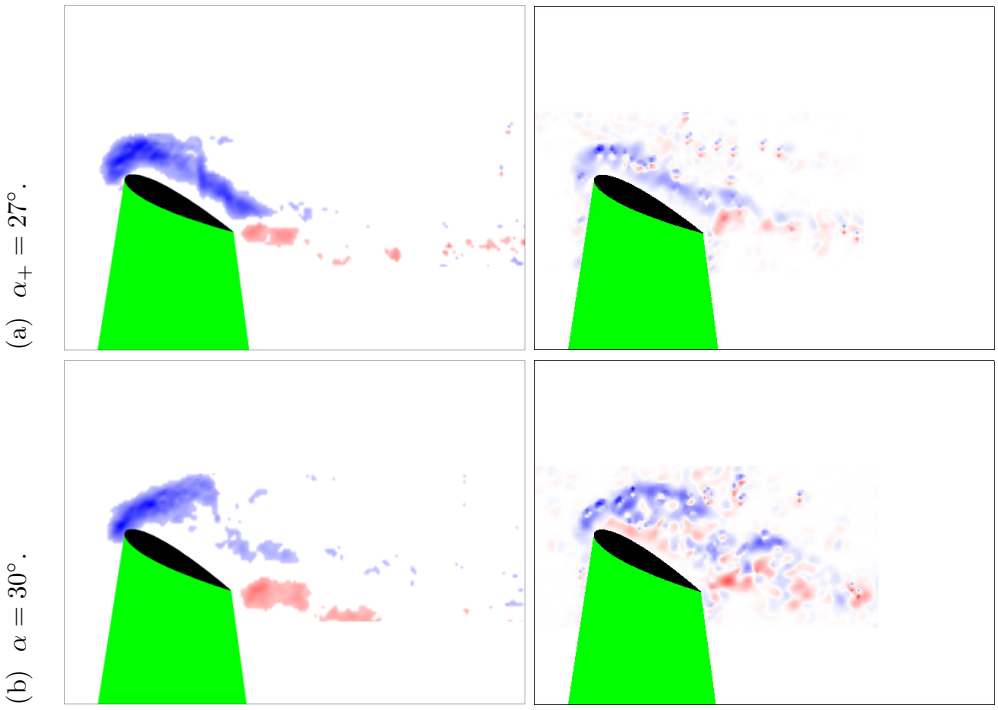

Figure 4.6: Vorticity contours from phase-averaged realization (left) and instantaneous (right) from the front field of view. Red and blue contours indicate positive and negative vorticity, respectively. The green area indicates the PIV laser shadow.

is similar to the measurements performed by Simão Ferreira et al. (2009) who found smaller vortical structure in the instantaneous measurements, within the phase-averaged LEV contour. Their results found a very slightly ($\sim 5\%$) stronger LEV circulation values in the instantaneous measurement due to small amounts of negative vorticity being included in the phase averaged LEV contour. These slight differences however do not change the results or conclusions presented in this section.

4.2.6 Vortex formation time

The development of the leading edge vortex can be further studied by considering the variation of the vortex circulation with time. The circulation of the LEV from $\alpha = 0°$ through separation at point Ψ from figure 4.1 is plotted against the airfoil convective time scale $\hat{T} = \int_0^T \frac{U(t)}{c} dt$ in figure 4.7, where $U(t)$ is the time dependent freestream velocity relative to the airfoil. The LEV development phase between Φ and B occurs in $\hat{T} \sim 4$. This is consistent with the universal vortex formation time of Gharib et al. (1998), with unsteady conditions as developed by Dabiri and Gharib (2005). This result suggests that at such low reduced frequencies ($k = 0.12$), the vortex formation is dominated by quasi-steady dynamics, and the vortex is able to grow to its maximum strength before convecting downstream at moment stall. Furthermore during this regime the rotational velocity of the airfoil

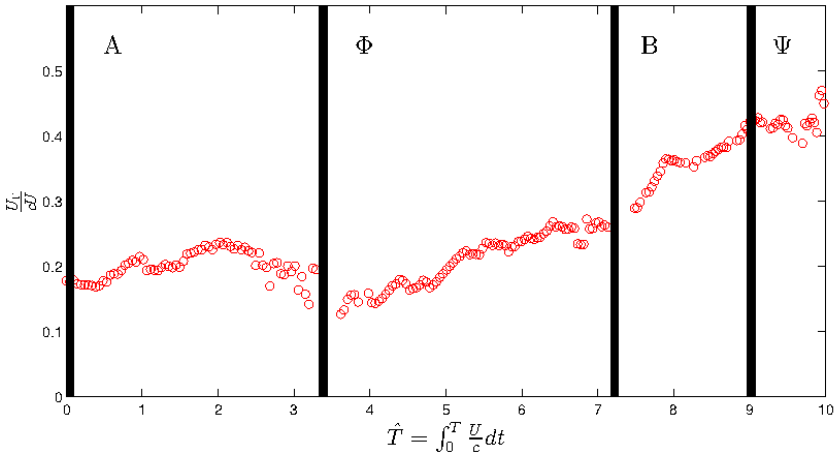

Figure 4.7: LEV circulation to formation time $\hat{T}$ over vortex growth period.

$\dot{\alpha}$ is small (and decreasing as it approaches maximum angle of attack), suggesting that the flow devlopment during vortex formation is not strongly affected by the increasing angle of attack. As such, the leading edge vortex development and shedding that leads to dynamic stall are dominated by the optimal vortex formation time. Therefore, while LEV formation is linked to the motion of the airfoil and appears in the phase-averaged results, the timescale responsible for the phase at which LEV develops and sheds, and thus the phase between the separation modes in Chapter 3, is associated with vortex formation while the arirfoil motion period determines the beginning of the vortex formation, (i.e. point Φ). This result is consistent with experiments by Rival et al. (2009) on plunging airfoils at slightly higher reduced frequencies.

4.3 Timescale III: Periodic vortex shedding

The phase-averaged flow fields presented in Chapter 3 and sections 4.1 and 4.2 provide insight into the flow structure associated with the frequency of the airfoil motion. However, flow phenomena not directly linked to the airfoil motion will be smeared out due to the phase-averaging process. To investigate these flow features, additional analysis of the flow field from a single experiment that measures the instantaneous flow development as discussed in section 2.3.1.2 was performed.

In the phase-averaged realization of the flow (figure 4.8) there is some vorticity shed behind the trailing edge, but no coherent periodic shedding can be observed at either angle of attack. In the instantaneous measurements (figure 4.9) counter clockwise vortices are clear and evenly spaced behind the trailing edge, indicating periodic vortex shedding at both angles of attack. At the higher angle of attack of $\alpha = 19°$ the shed vortices appear somewhat stronger than at $\alpha = 9°$. The spacing

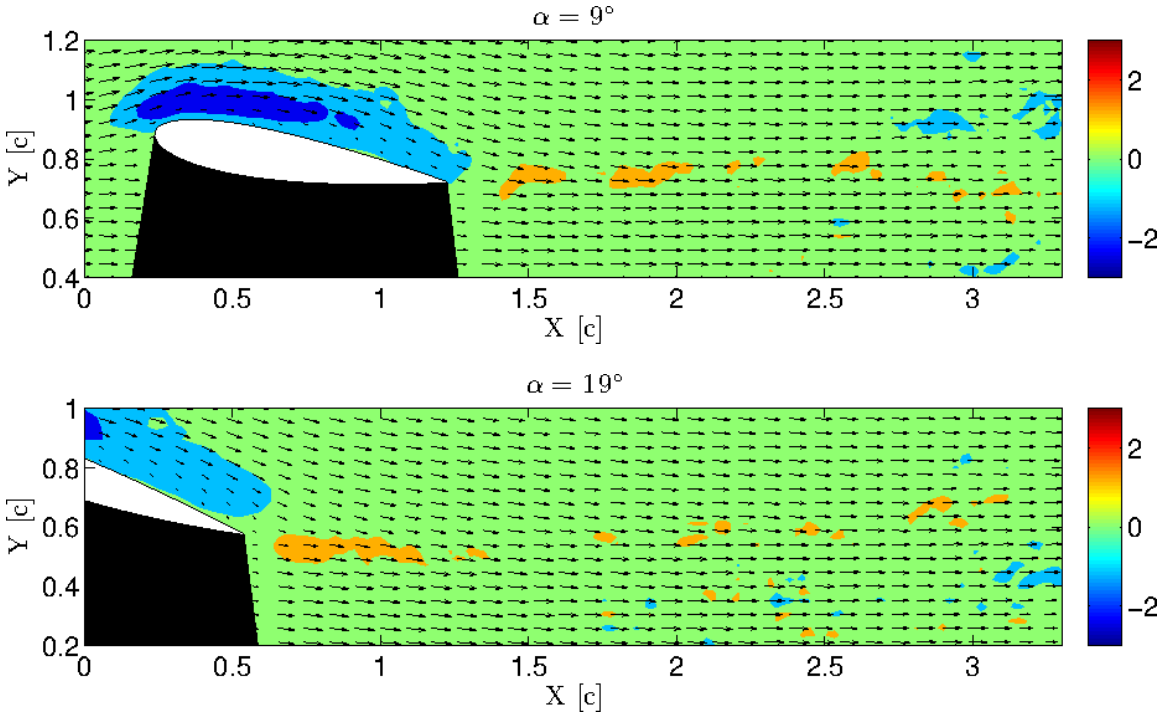

Figure 4.8: Vorticity contour plots, with velocity vector fields from phase averaged data set in the aft field of view for $\alpha = 9°$ (top) and 19° (bottom). Some vorticity can be seen behind the trailing edge, but no coherent periodic shedding is observed.

between vortices is similar at both angles of attack, and in both cases there is some delay behind the trailing edge before coherent shed vortices can be observed.

The circulation u_Γ was calculated for all vortices behind the trailing edge during the pitch up process ($0° \leq \alpha_+ \leq 30°$) using the Stokes theorem and integrating the vorticity within the $\Gamma_2 = 2/\pi$ contour. Average circulation of these trailing edge vortices is $\frac{U_\Gamma}{Uc} = [0.015, -0.008]$ for counter-clockwise and clockwise vortices, respectively. This suggests that they are individually approximately ten times weaker than the LEV, associated with dynamic stall discussed in section 4.2, and that the counter-clockwise vortices are approximately twice as strong as the clockwise ones. This dichotomy between the strength of positive and negative vortices is likely caused by the increased counter-clockwise shear imposed on the flow by the downward motion of the airfoil trailing edge during pitch up.

To identify the dominant timescales in the trailing edge shedding, the dynamic mode decomposition (section 2.4.2) was performed on the entire time history from the instantaneous data set in the aft field of view. The DMD spectrum is plotted in figure 4.10. Similar to the spectrum on the smaller measurement window presented in Chapter 3 there is a strong time-constant mode with zero growth rate and frequency, as well as a cluster of strong modes around the pitch/surge fre-

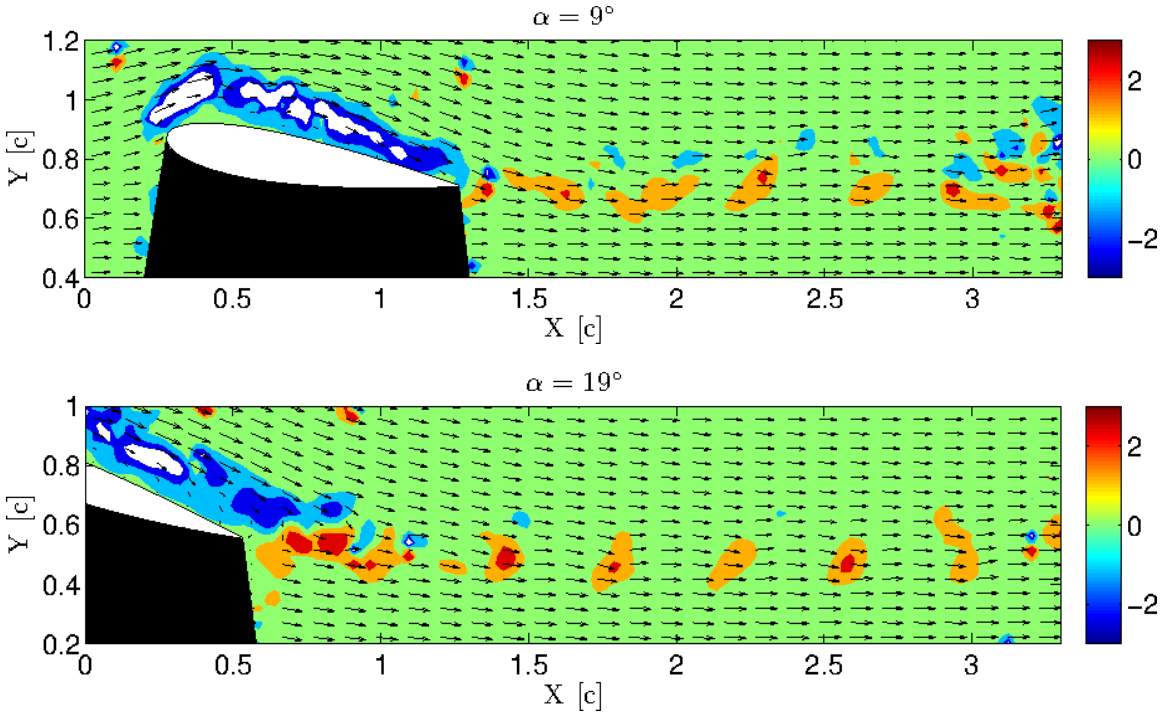

Figure 4.9: Vorticity contour plots, with velocity vector fields at the same contour level as figure 4.8 from the instantaneous data set in the aft field of view for $\alpha = 9°$ (top) and 19° (bottom). Shed vortices clear behind trailing edge.

quency. In addition to these modes, however, there are multiple modes with large spatial amplitude at high frequency, and/or a slow decay rate. Therefore it can be observed that there is broadband frequency content for the entire pitch/surge cycle, and it is more difficult to select relevant single modes. Instead a filter was used to select all modes within a frequency band, to investigate structure associated with a range of temporal frequencies.

Plotting all modes between $3 \leq F < 12$ Hz with half the contour level of figure 4.9 in figure 4.11, demonstrates similar shedding behavior as observed in figure 4.9, with periodic structure convecting downstream behind the airfoil trailing edge. This frequency band includes alternating vortices with equal strengths in clockwise and counter-clockwise rotation directions (negative and positive vorticity respectively). Including frequencies down to the pitch/surge frequency $F = \frac{0.6}{2\pi}$Hz reproduces the attenuation of the negative vorticity seen in figure 4.9. This demonstrates that the periodic motion of the trailing edge at the pitch/surge frequency adds positive vorticity to the wake, destructively interfering with the clockwise vortices as is expected due to the motion of the trailing edge. Including higher frequency modes, up to the Nyquist frequency of $F = 40$Hz, had no effect on the observation of the vortex shedding. Using this range selects modes with frequencies between five and twenty times faster than the airfoil motion, significantly above the range shown to capture

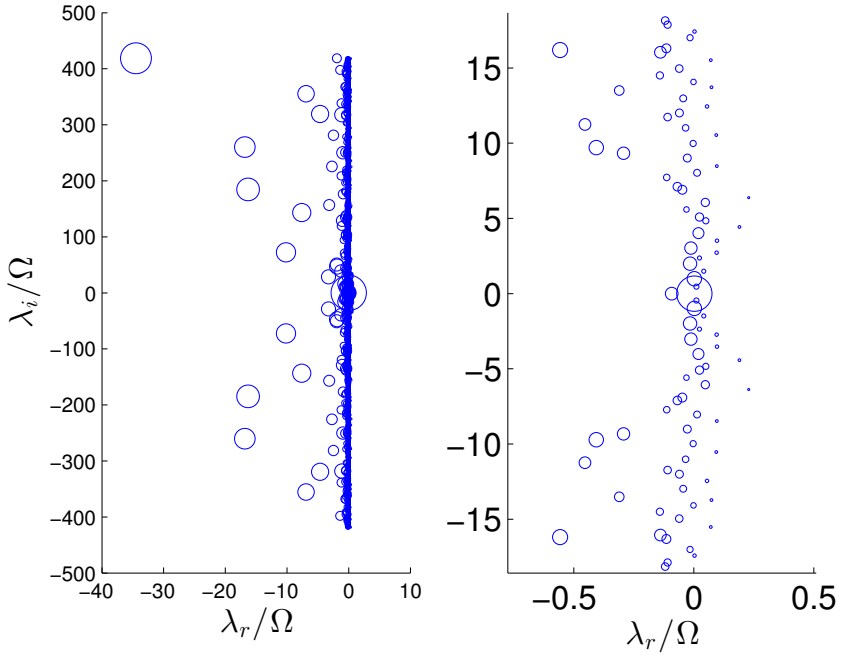

Figure 4.10: DMD mode spectrum performed on the instantaneous data set in the aft field of view. λ_r and λ_i modal growth rate and frequency, respectively. Point size determined by the relative spatial amplitude of the mode.

the phase-averaged flow presented in Chapter 3 and sections 4.1 and 4.2.

Immediately behind the airfoil $0.5 \lesssim x \lesssim 1.5$c, the vorticity seen in figure 4.11 is less distinct, and does not indicate clear, coherent vortices. Further downstream, however, coherent roughly circular vortices with alternating senses of direction are observed. This suggests that vortices are shed at the trailing edge, but are obscured by other behavior, and have not fully developed immediately at the trailing edge. Therefore they are observed after they have convected somewhat downstream. Decomposing the modes further into smaller bands of $5 \leq F < 8$ and $8 \leq F < 12$ Hz (figure 4.12) highlights this effect, with the evenly spaced vortices behind $x \sim 1.5$c contained between $5 \leq F < 8$Hz, while higher frequency modes that contribute minimally to the core shedding are required to represent the flow directly behind the airfoil. This decomposition clearly shows that vortex shedding is apparent while the flow is attached to the airfoil, and that the wake is characterized by coherent vortices that have been shed at the trailing edge, but require approximately one chord to fully develop.

The DMD mode representations at $\alpha = 9°$ appear similar, with all frequency content appearing between $3 \leq F < 12$ Hz (figure 4.13) and the highly coherent trailing edge shedding (sufficiently far behind the airfoil) still contained between $5 \leq F < 8$ Hz (figure 4.14). At this lower angle of attack

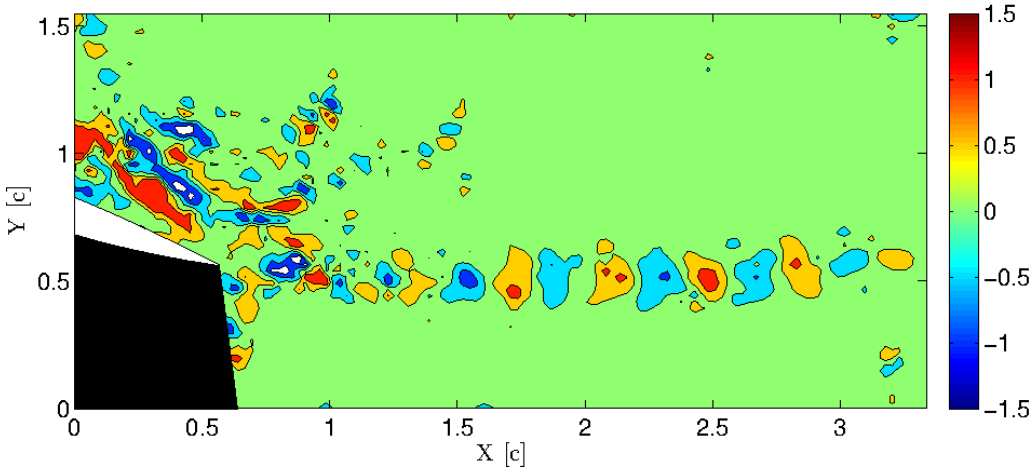

Figure 4.11: Vorticity contour plot of the DMD modes between $F = 3$ and 12 Hz at $\alpha = 19°$.

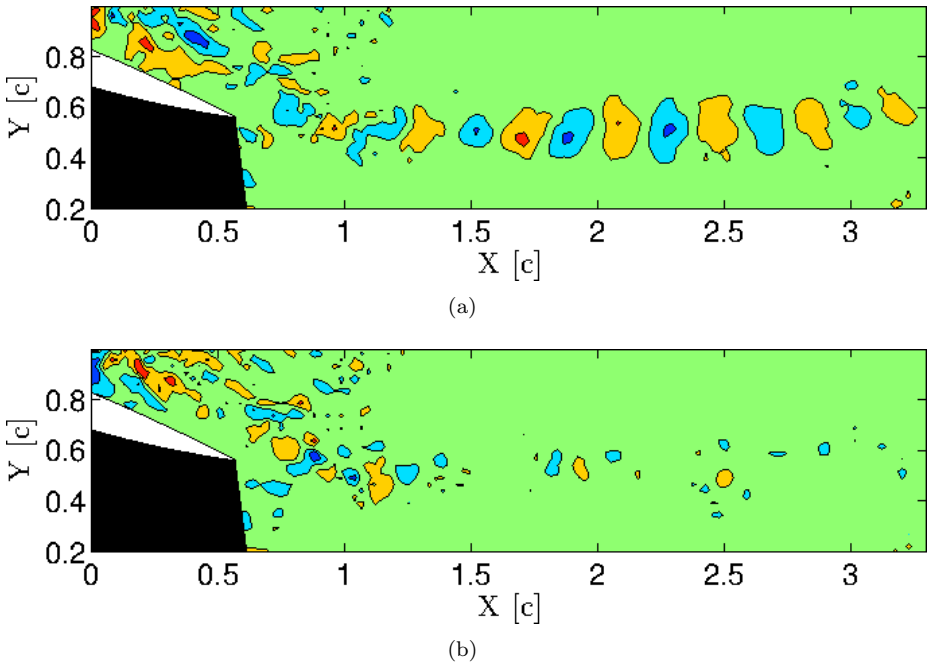

(a)

(b)

Figure 4.12: Vorticity contour plots of the DMD modes for $F = 5 - 8$ Hz (a) and $F = 8 - 12$ Hz (b) at $\alpha = 19°$ using the same contour level as figure 4.11.

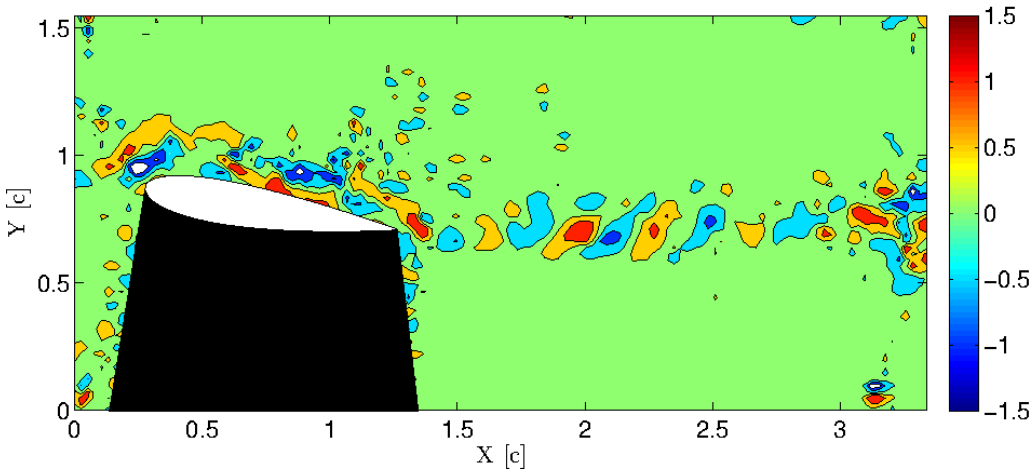

Figure 4.13: Vorticity contour plot of the DMD modes between $F = 3$ and 12 Hz at $\alpha = 9°$.

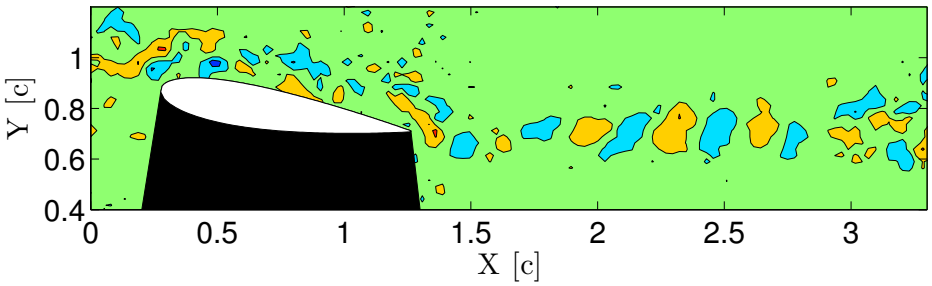

Figure 4.14: Vorticity contour plot of the DMD modes between $F = 5$ and 8 Hz at $\alpha = 9°$ at the same contour level as figure 4.13.

there is a change in behavior around $x = 3$c behind which coherent vortex shedding is not apparent in this frequency band. The less coherent vorticity field behind $x = 3$c in this figure is a result of vorticity shed by the airfoil before reattachment at $\alpha_+ = 0°$ that has not yet convected beyond the measurement domain.

To compare the exact shedding frequency between the two cases, single Hertz bands are plotted in the range between $5 \leq F < 8$ Hz in figures 4.15 - 4.17, for both angles of attack, at half the contour level of figures 4.11 - 4.14. At both angles of attack the majority of the shedding strength is contained between $6 \leq F < 7$ Hz; however, at $\alpha = 9°$ there is significant activity in the higher frequency band of $7 \leq F < 8$ Hz, while in the $\alpha = 19°$ case there is more at $5 \leq F < 6$ Hz, suggesting that the frequency of vortex shedding decreases with time.

In figure 4.18 isocontours of positive (red) and negative (blue) vorticity behind the trailing edge, within the frequency band $1.5 \leq F < 9.5$ Hz extruded over time for $0° \leq \alpha^+ \leq 30°$, are shown to demonstrate vortex shedding for the quarter of the period with positive angle of attack during

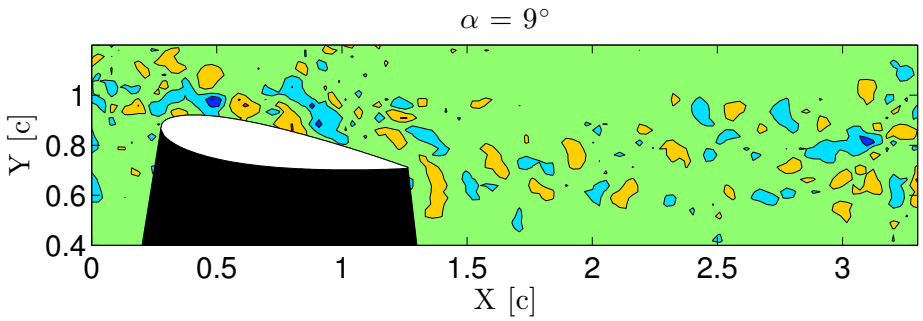

(a)

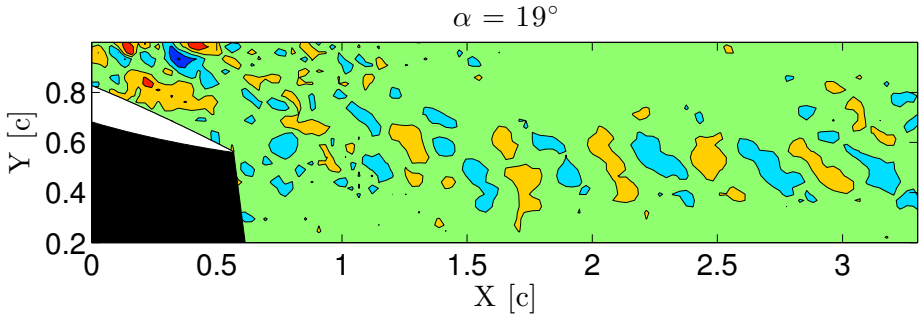

(b)

Figure 4.15: Vorticity contour plots of DMD modes between $F = 5 - 6$ Hz. $\alpha = 9°$ (top), $\alpha = 19°$ (bottom).

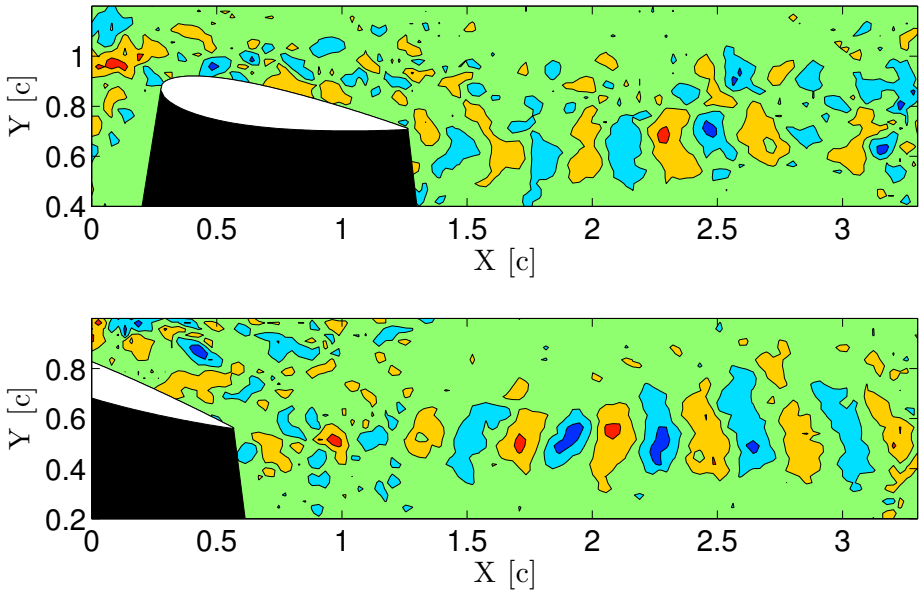

Figure 4.16: Vorticity contour plots of DMD modes between $F = 6 - 7$ Hz. $\alpha = 9°$ (top), $\alpha = 19°$ (bottom).

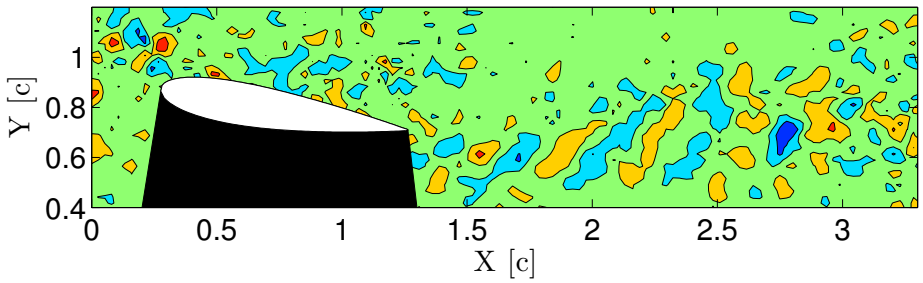

(a)

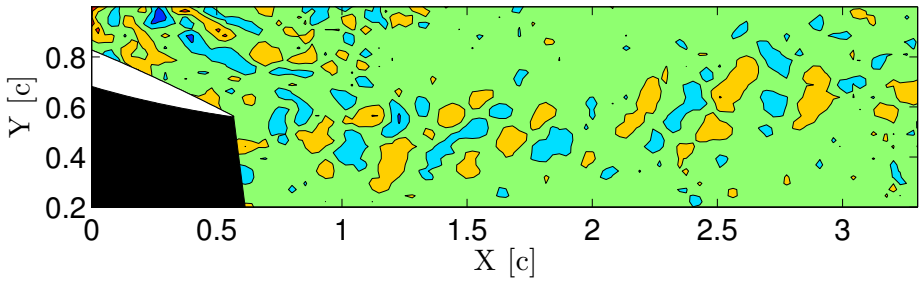

(b)

Figure 4.17: Vorticity contour plots of DMD modes between $F = 7 - 8$ Hz. $\alpha = 9°$ (top), $\alpha = 19°$ (bottom).

pitch up. Points A and B correspond to $\theta = 0°$ and separation as in figures 3.1 and 4.3. From point χ to separation at B clear periodic vortex shedding can be observed by the diagonal red and blue structures that indicate shed vortices that convect with the freestream. Similar to the results seen in figure 4.11 the vorticity directly behind the airfoil in this region is less consistent, since some distance is required before the shed vortices appear as individual structures. Before point χ and after point B vorticity content in this frequency band can be seen extending much further from the airfoil in the y direction and not solely located at the trailing edge position. This vorticity is produced by the separated flow over the airfoil prior to reattachment at A and after separation at B, and is not consistent nor periodic in this region.

In order to non-dimensionalize the frequency to form a Strouhal number $St = \frac{FL}{V}$, the instantaneous velocity $V = U(t) = \bar{U} - \frac{dx_l}{dt}$ was used where $\bar{U}$ is the free stream velocity and $\frac{dx_l}{dt}$ is the surge velocity of the airfoil. Airfoil thickness is the relevant cross-stream distance for attached flow and was chosen as the length scale L, in agreement with Koochesfahani (1989), and Jung and Park (2005). Using an approximate frequency for both angles of attack ($\alpha = 9°$ and $\alpha = 19°$) of $F = 6.5$ Hz results in Strouhal numbers of $St_{9°} = 0.38$ and $St_{18°} = 0.35$, respectively. This is in very good agreement with the results of Koochesfahani (1989), who found a natural frequency of airfoils oscillating at $k < 1$ of $St_{th} = 0.33$, and Jung and Park (2005) with $St_{th} \approx 0.3$ for $k = 0.1 - 0.4$

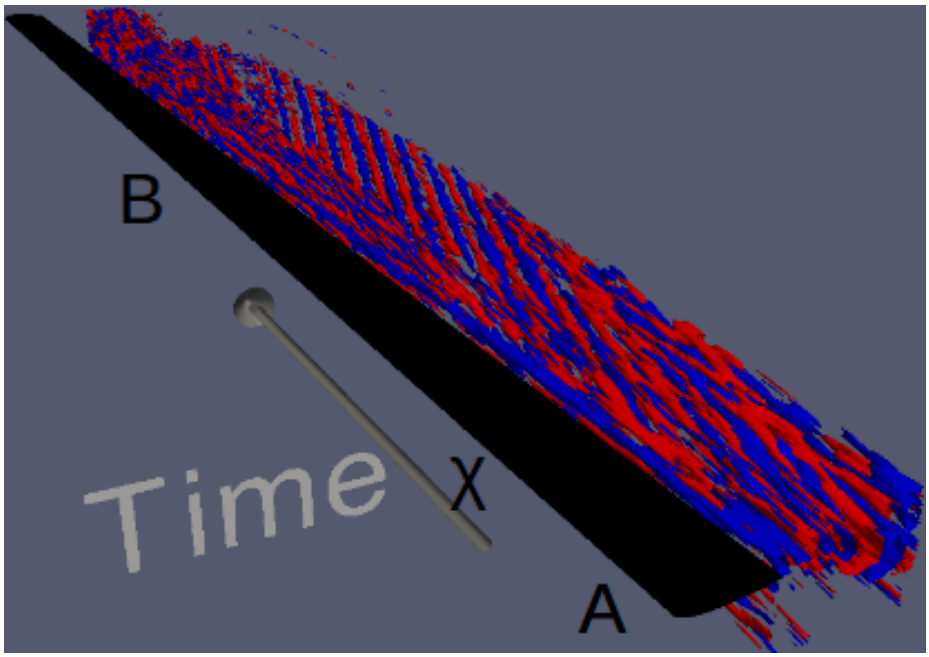

Figure 4.18: Vorticity isocontour of DMD modes with frequencies between $1.5 \leq F \leq 10$ Hz over the pitch up cycle $0° \leq \alpha_+ \leq 30°$.

around $\alpha = 3°$. This scaling is further supported by the apparent decrease in frequency between $\alpha_+ = 9°$ and $\alpha_+ = 19°$ corresponding to decreasing freestream velocity. These results suggest that during the attached flow regime from reattachment at $\alpha_+ \sim 0°$ to leading edge vortex development and separation at $\alpha_+ \sim 25°$, the flow behind the trailing edge is characterized by classical Strouhal vortex shedding.

4.4 Discussion

Three flow phenomena, with distinct causes and related timescales, were analyzed in the flow over blades undergoing a pitch/surge motion as a model for VAWT blades. First the dynamic stall that appears in the phase-averaged results and can be modelled using only the first two harmonics of the pitch/surge frequency. Leading edge vortex shedding and flow separation were shown to occur before maximum angle of attack, suggesting a second timescale that controls the separation process. The development of the leading edge vortex was shown to follow the optimal vortex formation timescale (Gharib et al., 1998; Dabiri, 2009), related to the airfoil chord and instantaneous freestream velocity, which determined the point in the motion period that LEV was shed and subsequent stall occurred. Finally, periodic vortex shedding from the trailing edge was found in the instantaneous measurements during attached flow. This vortex shedding occurs at the natural shedding frequency of the airfoil,

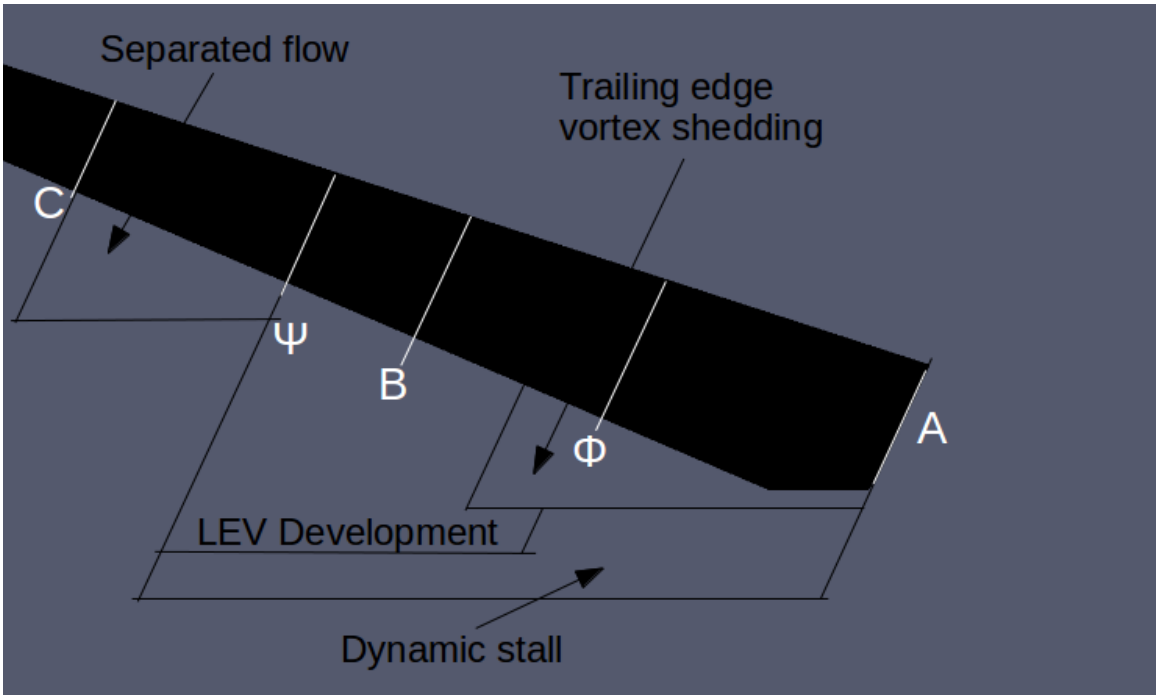

Figure 4.19: Schematic of the time extrusion for $0° \leq \alpha_{\pm} \leq 30°$ demonstrating the regions in which each timescale effects the flow. A corresponds to $\alpha_{+} = 0°$ and C corresponds to $\alpha_{-} = 0°$. White lines correspond to each location A, B, C, Φ, and Ψ in extruded time.

dominated by the freestream velocity and airfoil thickness, and is disconnected from the dynamic stall process. These effects span nearly two orders of magnitude of frequency between the pitch/surge frequency $\Omega = 0.095$Hz and a shedding frequency of $F^* \approx 6.5$ Hz corresponding to a Strouhal number of $St \approx 0.35$.

A schematic of the development of various observed flow phenomena between $0° \leq \alpha^{+} \leq 30°$ is shown in figures 4.19 and 4.20. The location of each overlapping regime in the time extruded frame is shown in figure 4.19. The phase-averaged spanwise vorticity (colored by velocity magnitude) and the 1.5-9.5 Hz DMD modes behind the trailing edge (red and blue contours behind the airfoil) are shown in figure 4.20(a) while figure 4.20(b) plots the $\Gamma_2 = 2.2/\pi$ contour indicating the leading edge vortex development.

From this figure the interplay between each timescale and related physical phenomenon can be observed. Initially, between A and ϕ the vorticity and Γ_2 criterion show fully attached flow, and periodic vortex shedding from the trailing edge is clear and uninterrupted. In this region the pitch/surge motion timescale and the periodic vortex shedding timescale are in effect, but acting somewhat independently, with vortex shedding occurring at high frequency at the trailing edge and the airfoil motion determining the evolution of the boundary layer.

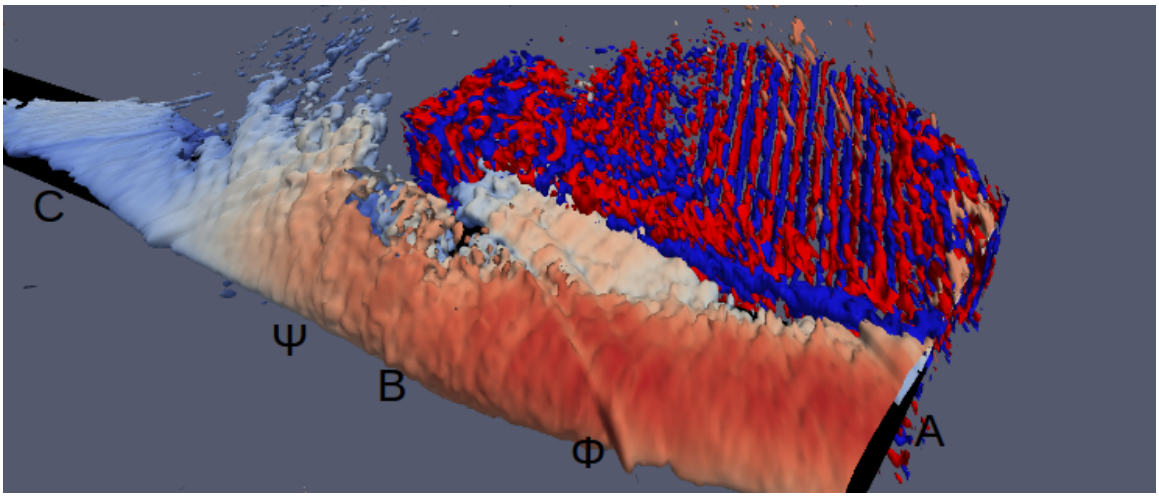

(a)

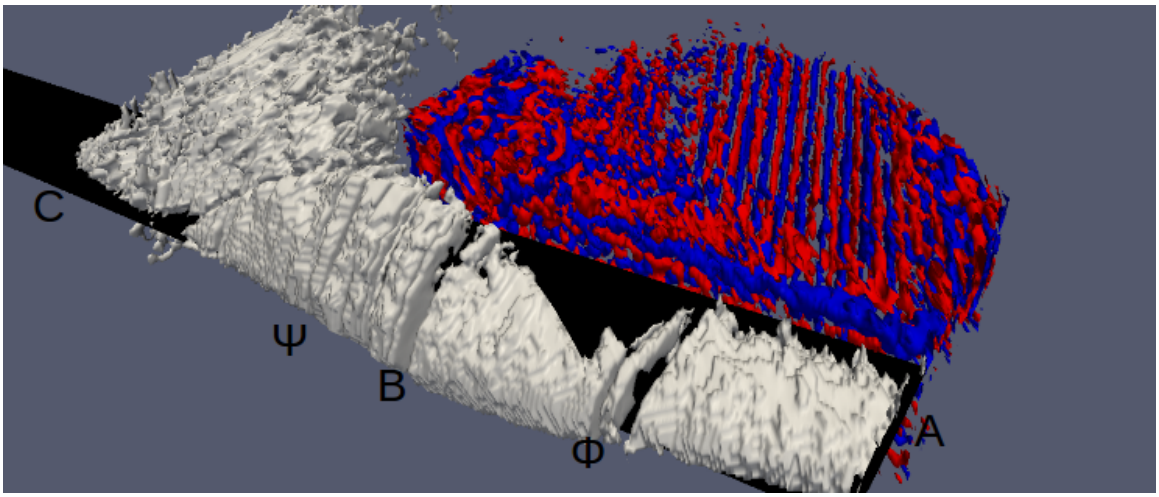

(b)

Figure 4.20: Time extrusion for $0° \leq \alpha_{\pm} \leq 30°$. The top figure shows the phase averaged spanwise vorticity (colored by velocity magnitude), and trailing edge vortex shedding determined from DMD in the range $1.5 \leq F < 9.5$ Hz (alternating red and blue contours behind the airfoil), Finally in the bottom the $\Gamma_2 = 2.2/\pi$ contour shows LEV development in relation to the trailing edge shedding. The trailing edge vortex shedding has been rotated to align with the airfoil for clarity.

In the LEV formation period from point Φ to point B, the vortex formation timescale begins to take over and dominate the phase averaged-flow physics. As the leading edge vortex develops and grows toward the trailing edge (figure 4.20(b)), trailing edge shedding is disrupted. Finally, at point B the LEV sheds from the leading edge as expected by optimal vortex formation theory. At this point the Γ_2 criterion in figure 4.20(b) indicates a large vortex moving downstream, weakening to the point that it is no longer captured by the vorticity isocontour level, which shows large scale flow separation. As the LEV convects downstream, it couples with the production of a large trailing edge vortex, and the physics leading to Strouhal vortex shedding based on the airfoil thickness is no longer valid, and the wake is characterized by broadband frequency content. After point Ψ the flow is fully separated and neither the periodic Strouhal shedding nor the vortex formation timescales are in effect, and, as such, the reattachment process linked to the period of the airfoil motion, as discussed in Chapter 3, is the relevant timescale. Note that point C corresponds to $\alpha_- = 0°$.

4.5 Summary and Conclusions

In this chapter the phase-averaged and instantaneous data sets on the combined pitching and surging airfoil are investigated in detail to determine the timescales associated with the flow structures apparent on VAWT blades. The first of these timescales is determined by the frequency of the pitch/surge motion, which sets the base periodicity of the flow, as well as determining the angle of attack at every point. The analysis in the previous chapter demonstrated that the flow fully separated before the maximum angle of attack and the corresponding change in pitch direction. Therefore, while the dynamic stall process is described by the relationship between the primary and secondary separation modes, as discussed in Chapter 3, the relative phase of these two modes that determines the point of separation is controlled by another timescale. Identifying and tracking the leading edge vortex in the full-flow field demonstrated that the leading edge vortex was allowed to fully saturate and convect away from the airfoil initiating separation from the leading edge and corresponding to lift stall by Carr et al. (1977). Temporal analysis of the development of this LEV showed that the formation of the vortex took approximately four airfoil convection times, corresponding to the 'optimal' formation time developed by Gharib et al. (1998), Dabiri (2009), and others. This result indicates that vortex formation is the second dominant timescale. It is associated with the airfoil convection time and vortex formation and determines the point of flow separation. The partial independence of these two timescales has implications for the design and modeling of vertical axis wind turbine systems, suggesting that if the LEV formation process can be altered by,

for example, delaying the start of formation, the LEV could be forced to saturate and shed exactly at the maximum angle of attack, resulting in maximum propulsive efficiency of the blade (Rival et al., 2009), or the stall point could be tailored to occur such that the shed LEV has little effect on the turbine structure and other blades.

Analysis of the instantaneous data set confirmed the existence of periodic vortex shedding from the trailing edge prior to flow separation. This periodic shedding is removed by the phase-averaged data set, suggesting that it is governed by fundamentally different physics. Converting the flow into frequency space with the dynamic mode decomposition permitted the physics of this periodic shedding to be probed. The vortex shedding was shown to occur with a timescale related to the natural, Strouhal, frequency of the airfoil, based on the thickness, the appropriate cross-stream dimension during attached flow. This periodic shedding is shown to develop relatively independently of the airfoil motion, until the effect of the leading edge vortex dominates, and the flow eventually separates when the periodic shedding breaks down. The only direct influence of the airfoil motion on the shedding is the attenuation of clockwise vorticity in the wake, due to the additional counter-clockwise circulation added due to the pitching motion of the airfoil. From this analysis three timescales spanning two orders of magnitude of frequency were identified, and their interaction and effect on the flow over the pitching and surging wing were characterized.

Chapter 5

Flow Around Airfoils Undergoing Independent Pitch and Surge Motions

This chapter presents measurements of the flow fields over airfoils undergoing pitch motions and surge motions independently in order to investigate the effect of both components of the flow on VAWT blades. The phase-averaged data sets from experiments for both motions, described in sections 2.3.2 and 2.3.3, are presented and compared to the phase-averaged pitch/surge motion (data set 2.3.1.1) discussed in Chapter 3 and 4. The combined effect of pitch and surge is not necessarily a linear combination, but key phenomena associated with each motion are identified here.

Vorticity isocontours of the pitch-only motion are compared to those of the combined motion to analyze the evolution of dynamic stall in each case and to highlight differences in separation and reattachment dynamics. The flows over surging airfoils at post-stall angles of attack of $\alpha = 15°$ and $\alpha = 20°$ are shown to highlight the effect of airfoil motion on partially separated airfoils. The leading edge vortex for the pitch motion is identified and compared to the combined pitch/surge case to understand the differing flow evolutions. Finally, dynamic mode decomposition is utilized to develop a low-order model of the phase-averaged pitching flow, similar to that developed for the pitch/surge combined case in Chapter 3. This low-order model is shown to capture the changes in physics when the surging motion is removed. A portion of this work was presented at the AIAA Applied Aerodynamics Conference, in June of 2015 in Dallas, TX, and is published in the proceedings (Dunne and McKeon, 2015a).

5.1 Separation on pitching airfoils

Comparing isocontours of vorticity from the pitch-only case to the combined pitch/surge flow from Chapter 3 (figure 5.1) shows somewhat similar behavior. Initially both isocontours show attached flow followed by separation (at point B) and reattachment (at point C) beginning from the leading edge and extending aft. The velocity magnitude colorbar is left dimensional, with a reduced range due to the smaller velocity variation in pitch only, but points A, Φ, B, and C are left in the same angular location θ in the motion. The exact dynamics of separation, however, are different. At point Φ vorticity begins to lift up, away from the surface of the pitching airfoil, as opposed to wrapping around the leading edge as observed in the pitch/surge case (figure 5.1(a)). Furthermore, separation occurs at a lower angle of attack, before point B, in the pitch-only case. This suggests that there is some delay caused by the deceleration of the airfoil in the combined pitch/surge motion. During reattachment, beginning at point C, the pitch-only isocontour (figure 5.1(b)) exhibits a much more abrupt transition from attached flow over the leading edge to separated flow further back.

5.1.1 Leading edge vortex development

The Γ_1 and Γ_2 vortex tracking methods described in Chapter 2 were implemented on the pitch-only data set in the airfoil reference frame and compared to the measurements made in Chapter 4. The streamwise position of the leading edge vortex x_v and circulation u_Γ normalized by $\bar{U}$ and c is plotted against angle of attack for both pitch and pitch/surge motions in figure 5.2. Four distinct regimes of leading edge vortex growth are apparent from these plots separated by black lines at points A, B, C, Φ, and Ψ. Points A, B, and C correspond to $\alpha_+ = 0$, separation, and reattachment as in section 5.1 and figures 5.1(a) and 5.1(b). A contour of the Γ_2 value for the leading edge vortex colored by vorticity is shown for both cases in figure 5.3, over the same period. Changes in the LEV structure visible in figure 5.3(a) correspond to the same regimes identified in figure 5.2.

As the airfoil is pitched up past $\alpha_+ = 0°$ a different effect is seen in the identified vortex in the pitch and pitch/surge cases. In pitch-only, a small vortex is seen at leading edge, whereas in pitch/surge, the Γ criteria pick up the rotation of the flow around the maximum curvature of the NACA 0018 airfoil. This suggests that the dominant rotation of the flow in pitch is determined by the leading edge vortex, while the combined case behaves more similarly to a static airfoil, with flow streamlines rotated due to the airfoil shape. In this regime the LEV in the pitch-only case increases in strength at a constant rate similar to the vortex formation regime of the pitch/surge flow (Chapter 4). Slightly prior to point Φ, where the LEV formation begins in the combined pitch/surge case, the

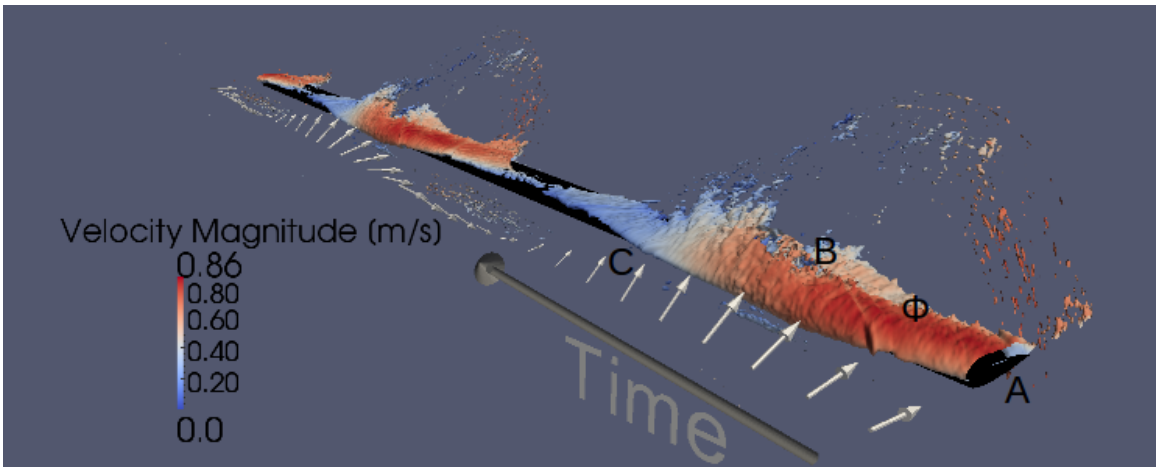

(a) Combined pitch/surge motion.

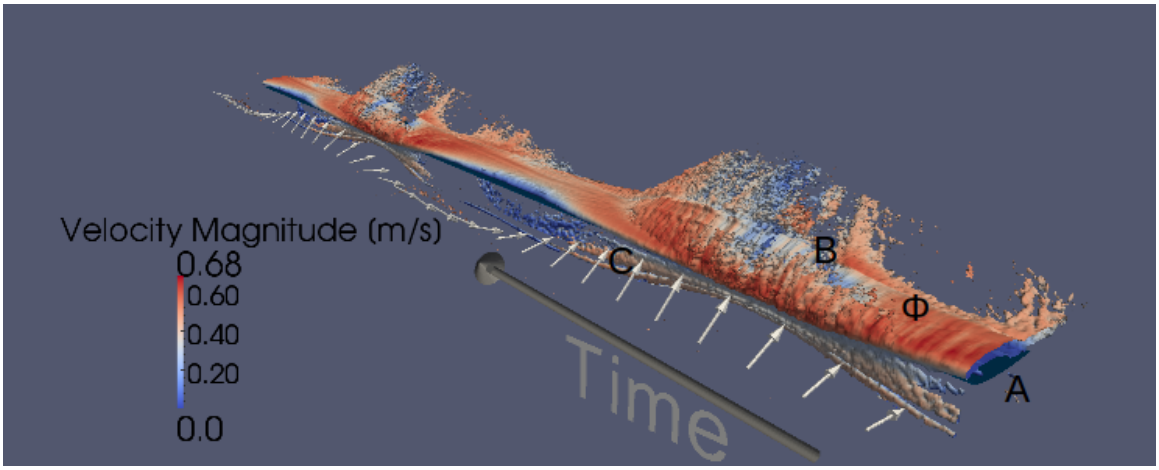

(b) Pitch-only motion.

Figure 5.1: Vorticity isocontour for sinusoidal pitch (bottom) and combined pitch/surge motion (top) colored by velocity magnitude. Two periods shown beginning at A $\theta = 0°$, $\alpha = 0°$ maximum surge velocity as in figure 1.1. Arrows indicate incoming angle of attack variation. Φ indicates the beginning of leading edge vortex growth, B at separation location, C at the beginning of reattachment.

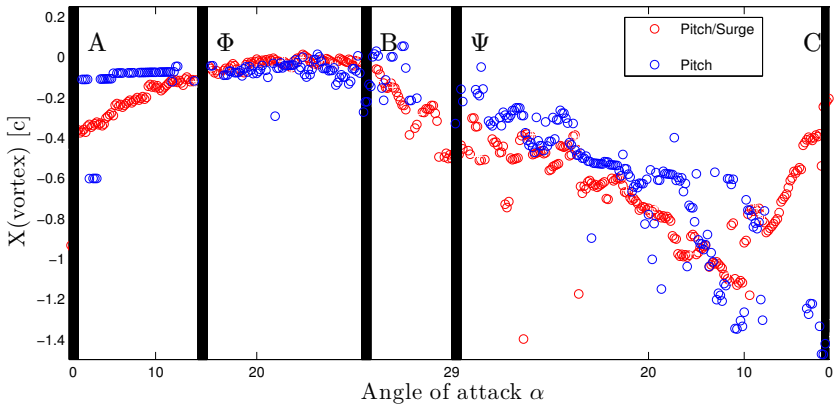

(a) Vortex X position leading edge at 0 downstream negative

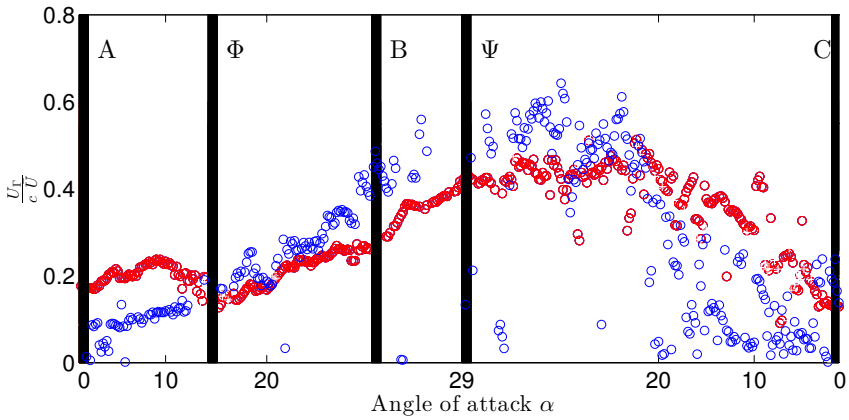

(b) Non-dimensionalized LEV circulation

Figure 5.2: Leading edge vortex x position (top) and circulation (bottom) over half a pitch up/down cycle $\alpha \geq 0$ for pitch (blue) and combined (red) cases.

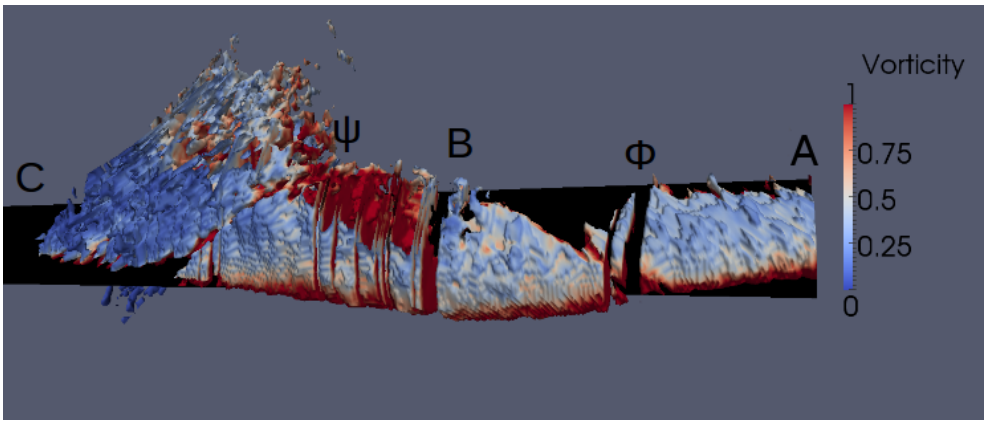

(a) Pitch/surge

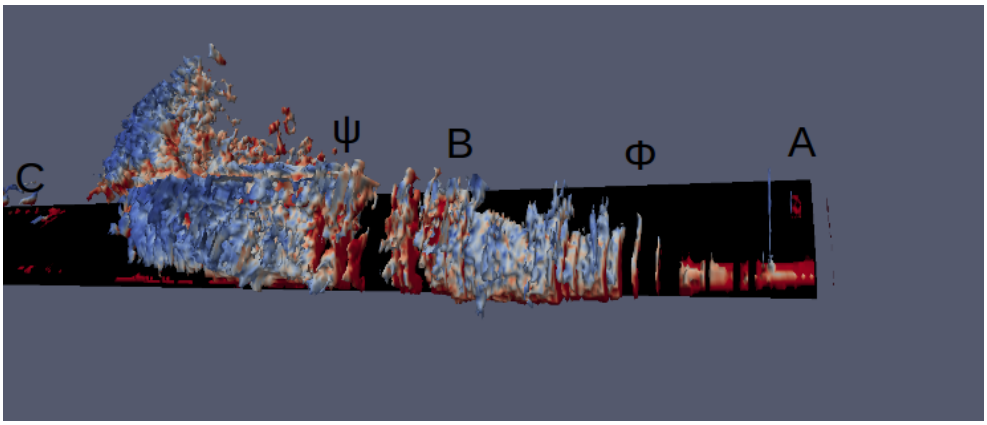

(b) Pitch

Figure 5.3: $\Gamma_2 = 2.2/\pi$ isocontour of identified leading edge vortex colored by vorticity magnitude for half a pitch up/down cycle $\alpha \geq 0$ (Pitch/surge (top), pitch (bottom)). Time is from right to left. A, Φ, B, Ψ, and C correspond to figure 5.2, based on changes in the pitch/surge flow field. Gaps exist where Γ vortex criteria are not met.

LEV in the pitch-only case begins to grow significantly, entraining more vorticity outside the circular core of the vortex (figure 5.3(b)). This shares a similar structure to the LEV in the pitch/surge flow during vortex formation and corresponds to an increase in the rate of increase of the pitch-only LEV circulation. During this regime the growth of the LEV is faster in the pitch-only case, resulting in a stronger LEV when it sheds somewhat before point B (where the pitch/surge LEV sheds figure 5.2(b)). After point B the LEV is quickly lost from the top of the measurement window, resulting in missing contours (figure 5.3) and lack of measurements of the vortex position and circulation between point B and point Ψ (figure 5.2). After point Ψ both pitch and pitch/surge cases exhibit full leading edge separation and the $\Gamma_2 = 2.2/\pi$ contour indicates non-coherent rotational flow from separated body.

5.1.2 Vortex formation time

The normalized circulation ($\frac{\mu_\Gamma}{c\bar{U}}$) and x position of the leading edge vortex is plotted against the airfoil convection time ($\hat{T} = \frac{\bar{U}t}{c}$ simplified due to the constant freestream) in figure 5.4 for pitch up and down $\alpha \geq 0°$. As seen in this figure as well as figures 5.2 and 5.3 the LEV is present at the leading edge at $\alpha_+ = 0°$, and remains there until it sheds at point B', just before point B (where the combined pitch/surge LEV sheds), indicated by the vortex beginning to move back ($-x$) in figure 5.4(b). Additionally at this point the rate of change of LEV circulation increases. Similar to the pitch/surge combined case the vortex formation regime in the pitch only flows from $\alpha_+ = 0$ to point B' at $\alpha_+ \sim 24°$ and occurs over $\hat{T} = 4$ convection times, corresponding to the optimal vortex formation timescale of Gharib et al. (1998) and Dabiri and Gharib (2005). In the pitch only case, however, the vortex nucleates much earlier and grows over a much larger portion of the pitch up cycle.

5.2 Low-order model of the flow over a pitching airfoil

The dynamic mode decomposition method described in section 2.4.2 and used to develop a simplified three-frequency model of the combined pitch/surge flow in section 3.2 was performed on the pitching airfoil. An identical box to the analysis in section 3.2 was chosen with one chord in the streamwise direction and one-quarter chords in the cross-stream direction. This selection was made to enable direct comparisons between the two cases. The extent of this box can be seen in the airfoil frame in figures 3.6 and 5.9. The DMD spectrum scaled by the motion frequency $\Omega = 0.6$ rad s^{-1} is plotted

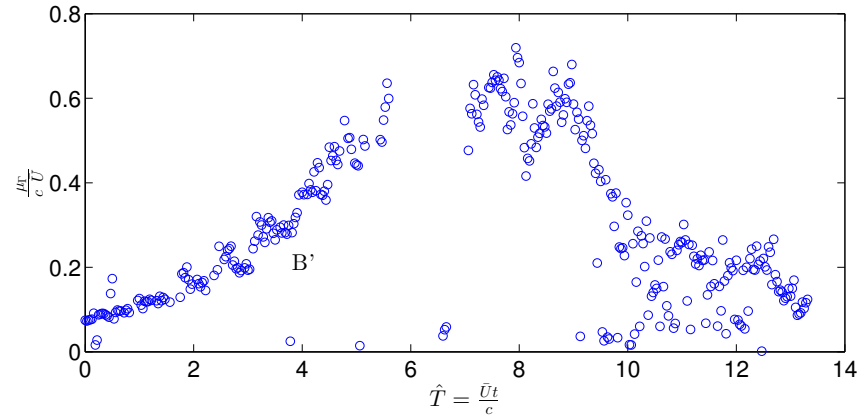

(a)

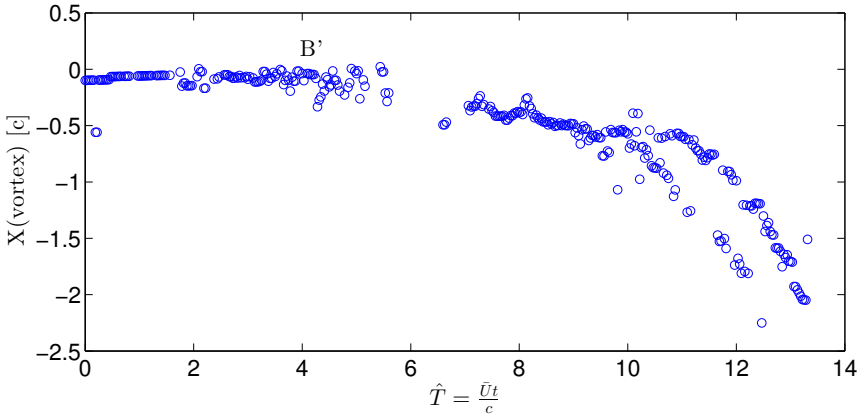

(b)

Figure 5.4: Leading edge vortex circulation and x position plotted against airfoil convection time for pitch up/pitch down half period $\alpha \geq 0$. $\hat{T} = 0$ corresponds to $\theta = 0°$, $\alpha_+ = 0°$.

.

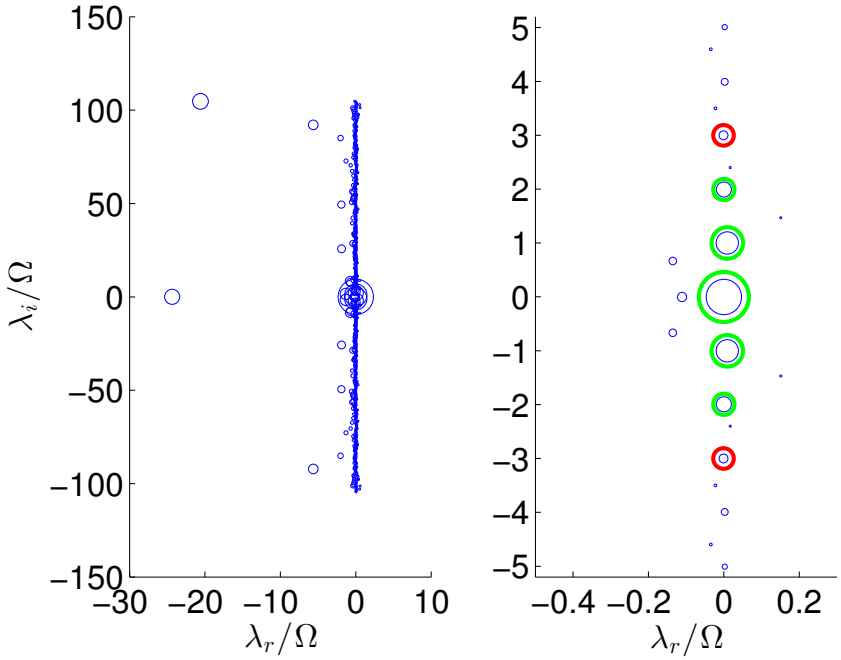

Figure 5.5: Modes calculated with DMD for pitch-only motion scaled by pitch frequency Ω. λ_r growth rate λ_i frequency. Point size scaled by the magnitude of the spatial structure, a. Left full spectrum, right zoomed in on strong, non-decaying modes. Modes circled in green used for five-mode model, red modes used for seven-mode model.

in figure 5.5 with the real part λ_r on the x axis representing the growth rate, and the imaginary part λ_i on the y axis representing frequency. Similar to the spectrum for the combined pitch/surge flow in figure 3.7 the majority of the modes cluster around the imaginary axis as expected for phase-averaged data. Large modes with $\lambda_r \leq -20\Omega$ are not physically relevant for this flow but account for experimental variation in the first few time steps. Again, the most dynamically important modes with large amplitude (a) values have $\lambda_r \sim 0$, indicating no decay or growth, and $\lambda_i \approx \pm n\Omega$, where n is an integer, indicating that they are harmonics of the pitch frequency. The decrease in the amplitude of the spatial structure a with increasing n, however, is weaker with the modes at $\lambda_i = \pm 3\Omega$ circled in red still appearing strong when compared to modes at $\lambda_i = \pm 1$ and 2Ω.

Isocontours of vorticity for the pitching flow in the DMD domain and a model using only the first five modes (highlighted in green in figure 5.5), including the mean base-flow, as well as the first two harmonics of the pitch frequency $\lambda_i = \pm 1$ and 2Ω, are shown in figure 5.6. This model is able to capture the initial attached flow from the pressure side $\alpha_+ \leq 0°$; the beginning of separation occurs in both the model and the full flow at point B. However, this five-mode model does not capture the shape of the separation region after point B as well as in the pitch/surge case. Furthermore, the flow

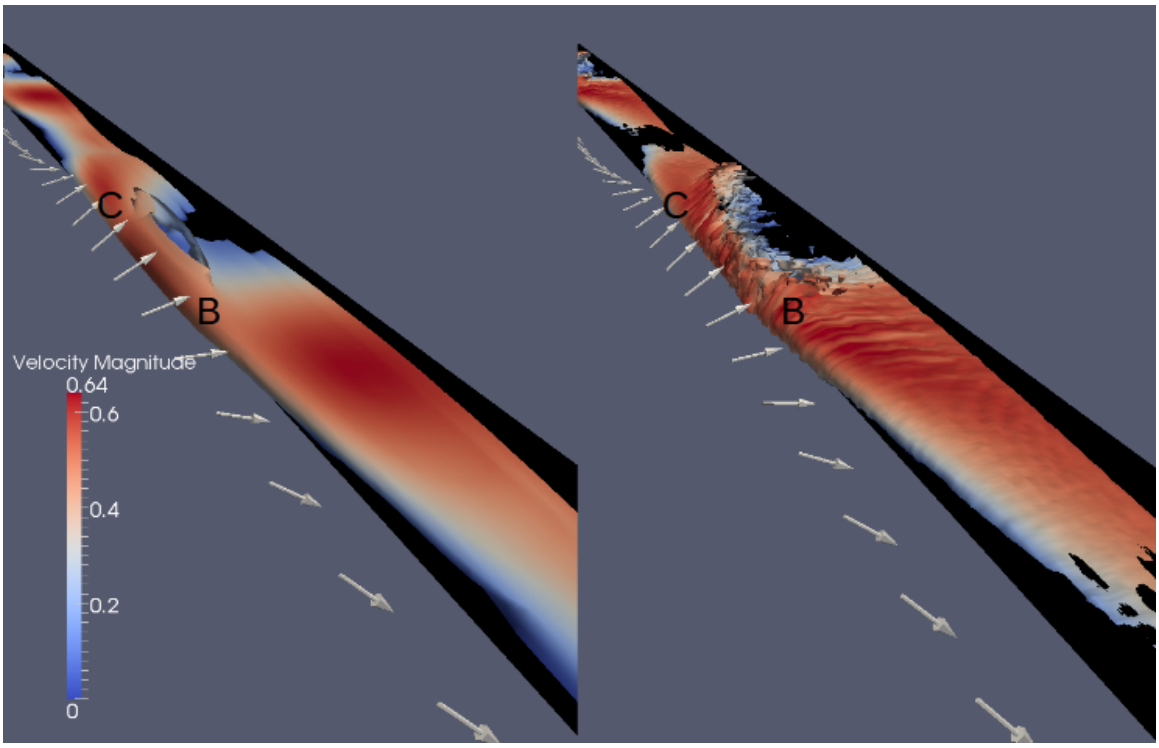

Figure 5.6: Isocontour of vorticity (colored by scaled velocity magnitude) of the five-mode DMD reconstruction (left) and data (right) focused on point of dynamic stall. Vectors show the incoming velocity field. Model captures separation point, but misses flow detail.

in the model appears to reattach abruptly in time and at too high an angle of attack as opposed to the smooth transition toward the trailing edge of the airfoil beginning at point C observed in the full dataset.

In order to correct the five-mode model in figure 5.6, the next harmonic frequency modes at $\lambda_i = \pm 3\Omega$ (highlighted in red in figure 5.5) were added. These modes have a competitively high amplitude a as compared to those for the pitch/surge flow at the same frequency and, as such, are able to change the reconstruction significantly. This seven-mode model is shown in figure 5.7 and is able to capture the shape of the separated region more accurately. In this representation the reattachment no longer occurs instantly as shown in the five-mode model, but instead the separation point moves back smoothly, similar to the full data. Furthermore, in the seven-mode model the maximum velocity magnitude, indicated by red color, appears just before separation at point B, similar to the full dataset, and unlike the five mode model that exhibits a significant decrease in velocity prior to point B. On the pressure side of the airfoil, after point C, the isocontour of the full dataset briefly drops out, indicating a slightly weaker vorticity value measured at the first grid point above the airfoil surface.

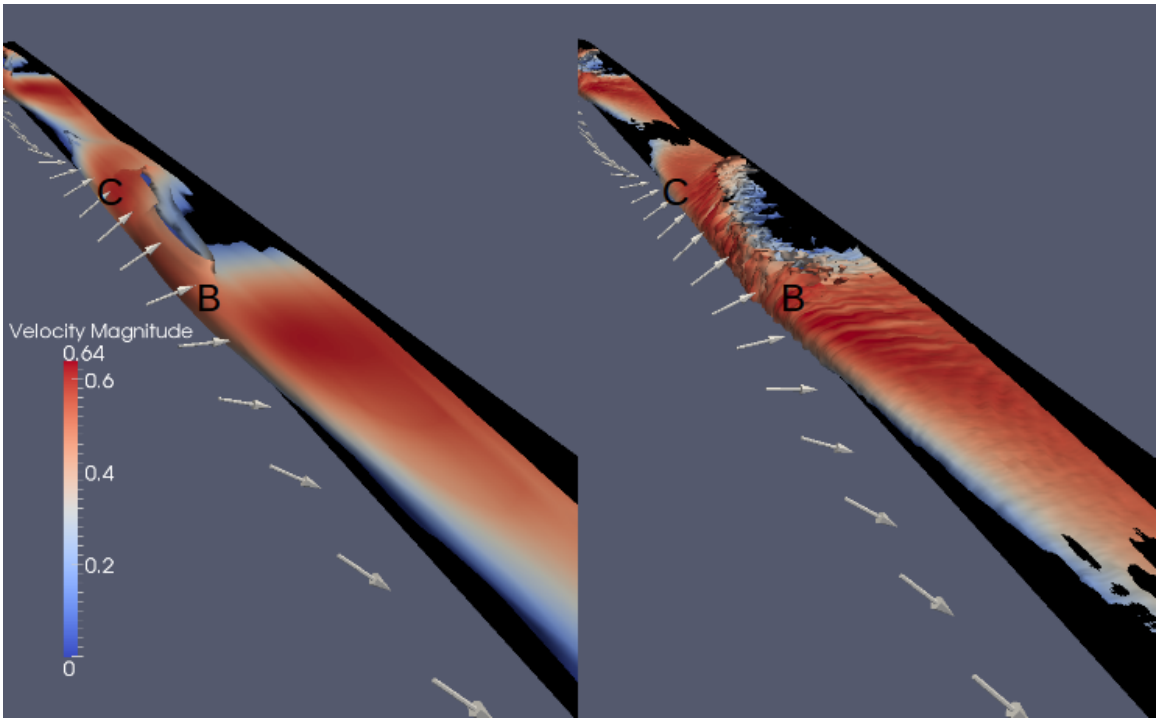

Figure 5.7: Isocontour of vorticity (colored by scaled velocity magnitude) of the seven-mode DMD reconstruction (left) and data (right) focused on point of dynamic stall. Vectors show the incoming velocity field. Shear layer and reattachment shape captured with the addition of $\lambda_i = \pm 3\Omega$ mode to the reconstruction in figure 5.6.

An enlarged image showing only the separated region, including reattachment, is shown in figure 5.8(a), and demonstrates that the seven-mode model captures the details of the separated region. For comparison a similar image of the five-mode model (figure 5.8(b)) demonstrates early reattachment. Similar to the model of the combined pitch/surge flow in Chapter 3, this reconstruction misses the high frequency behavior, seen as ripples in the full data set, that is associated non-phase-averaged behavior, which is not fully removed in the averaging process as well as high frequency behavior. Increasing the order of the model to nine modes, and thus including $\lambda_i = \pm 4\Omega$, had a slight effect on the overall shape of the shear layer but did not have significant effect on the qualitative accuracy of the model.

5.2.1 Modal breakdown

The mean mode $\lambda_i = 0$ is shown in figure 5.9(a) to illustrate the base-flow around which the flow varies and for comparison with the mean mode of the pitch/surge flow (figure 5.9(b)) plotted previously in figure 3.6. From this comparison it is clear that in the pitch-only case the flow rotation is confined closer to the leading edge and does not grow around the front of the leading edge as shown qualitatively in section 5.1. Furthermore, the average vorticity remains closer to the airfoil in y, indicating that the mean shear remains closer to the airfoil surface.

The first mode pair at the pitch frequency Ω is plotted at specific points in the pitch up/down period in figure 5.10. This pair shows similar behavior to the primary separation mode identified in Chapter 3 (figure 3.11). Similar to the mean flow, the shear associated with this mode occurs closer to the airfoil surface; however, structures that can be seen in the vector plots are qualitatively similar. During pitch up (figure 5.10 (a-c)) a clockwise vortex nucleates at the leading edge at $\alpha_+ \sim 0^\circ$ and can be seen to convect downstream by $\alpha_+ \sim 8^\circ$, driving the flow away from the airfoil and leading separation. On pitch down the opposite sense vortex appears as expected at $\alpha_- \sim 0^\circ$. The appearance and convection of the vortex associated with this mode occurs approximately two degrees earlier than that of the pitch/surge model seen in section 3.2. This agrees well with the qualitative observation that the LEV appears and separation occurs somewhat earlier in the pitch only flow, and confirms that the separation process is driven by this mode.

The second mode pair at $\lambda_i = \pm 2\Omega$ is shown in figure 5.11, for comparison with the secondary separation mode identified for the combined pitch/surge flow in Chapter 3 (figure 3.12). During pitch up, a vortex with clockwise rotation just above the leading edge is apparent in the vector plot at $\alpha_+ = 16^\circ$, as well as the vorticity contour, and convects downstream by $\alpha_+ = 25^\circ$, similarly to the

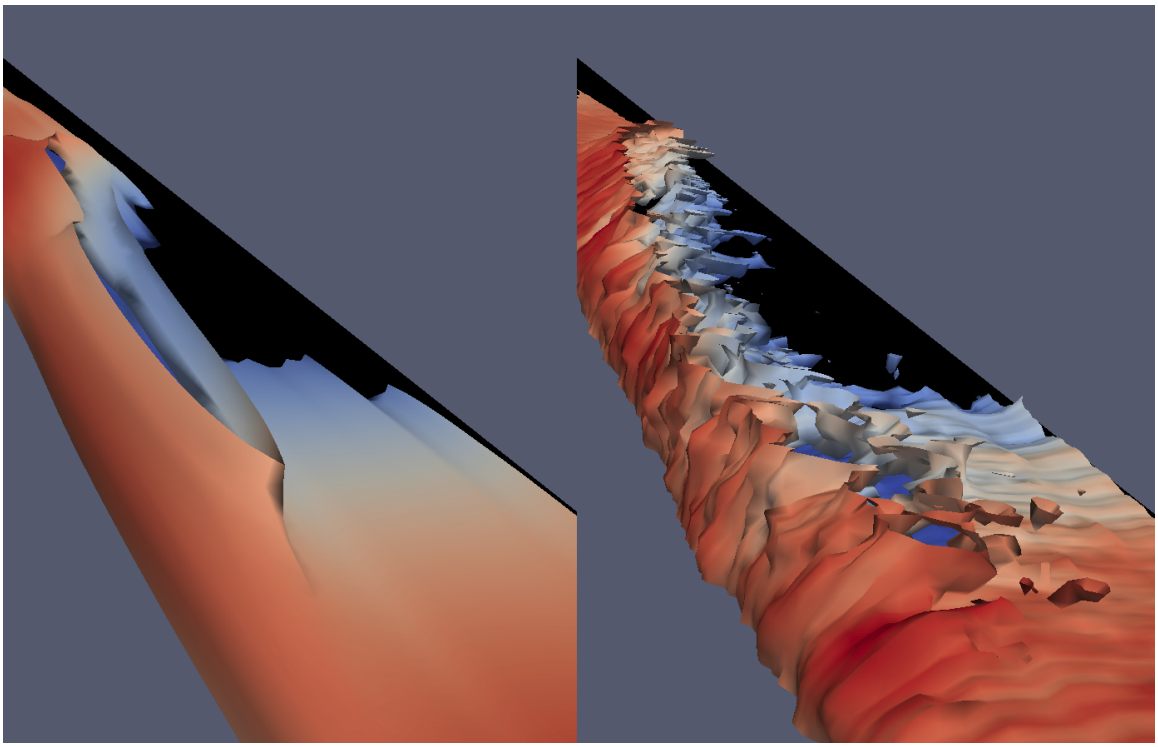

(a) Seven-mode model

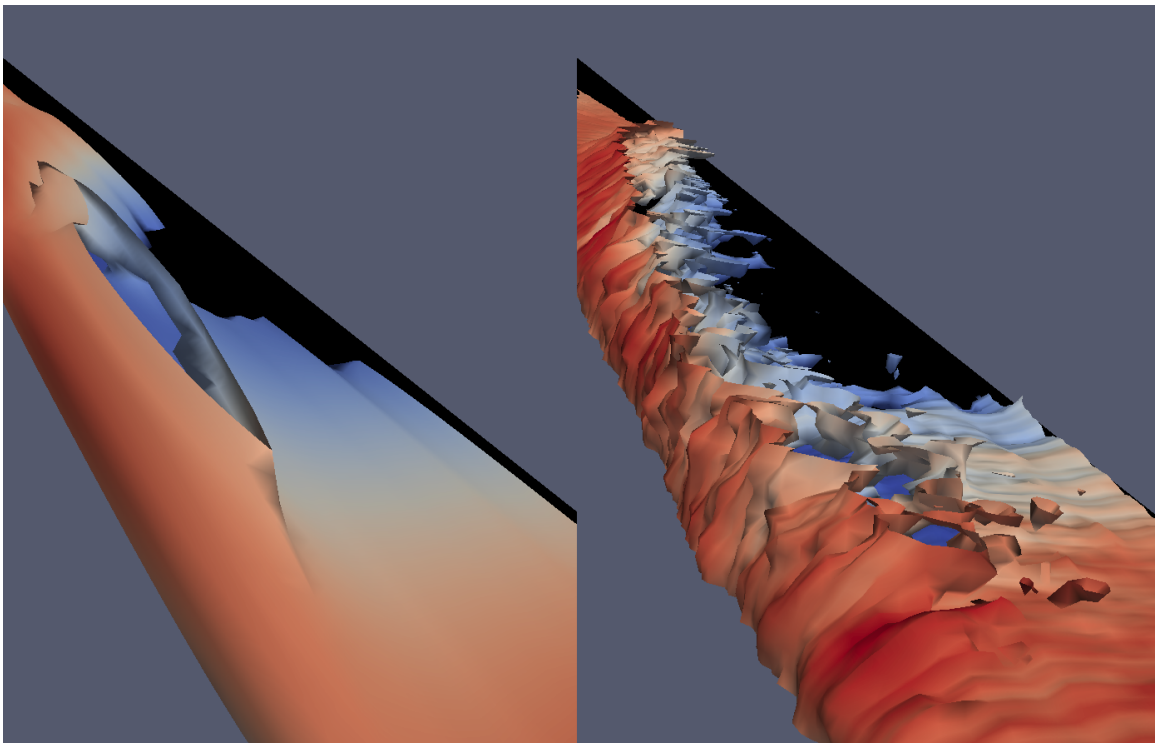

(b) Five-mode model

Figure 5.8: Isocontour of vorticity of seven-mode (top) and five-mode (bottom) DMD reconstruction (left) and data (right) zoomed in on the separated region. Unlike the five-mode model, the seven-mode model captures the details of the separated region, including reattachment point.

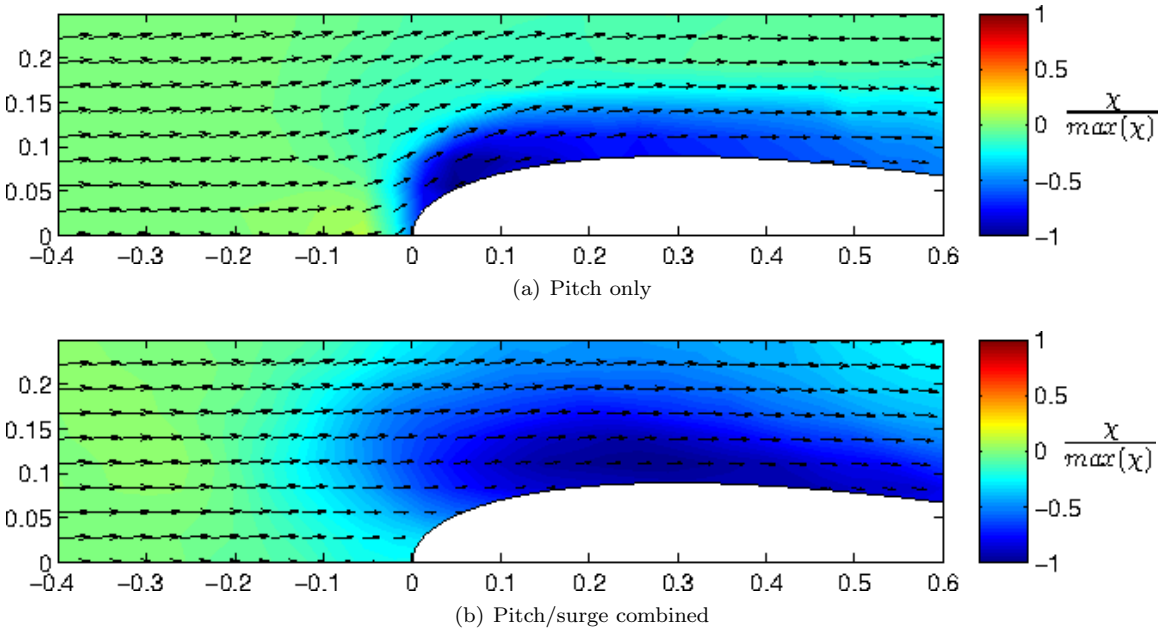

(a) Pitch only

(b) Pitch/surge combined

Figure 5.9: Velocity (vectors) and vorticity (contour), scaled by maximum modal vorticity, plots of time constant base flow in airfoil-centered frame from a single DMD mode. Incoming flow and diffuse vorticity associated with flow curvature around the airfoil are captured.

secondary separation mode for the combined pitch/surge flow. This structure enhances separation, effectively strengthening the primary separation mode associated with $\lambda_i = \pm\Omega$ (figure 5.10). On pitch down the opposite structure appears as a vortex with counter-clockwise rotation above the leading edge at $\alpha_- = 26°$, convecting downstream by $\alpha_- = 17°$. Comparing these modal flow fields to those for the pitch/surge combined case in figure 3.12 the nucleation and convection of this clockwise vortex occurs at a much higher angle of attack (lower turbine angle θ) with figure 5.11(d) at $\alpha_- = 17°$ corresponding to figure 3.12(e) at $\alpha_- = 8°$ for pitch/surge. This relatively earlier vortex for pitch-only results in the artificially early reattachment observed in the five-mode pitch only model.

Adding the mode pair at $\lambda_i = \pm 3\Omega$ to the $\lambda_i = \pm 2\Omega$ one, as used in the seven-mode model, and plotting the combined spatial structure corrects the early separation (figure 5.12). On pitch up at $\alpha_+ = 16°$ and 25° both vorticity and vector plots appear similar to those of the $\lambda_i = \pm 2\Omega$ modes corresponding to the minimal change in initial separation behavior between the five- and seven-mode models (figure 5.6 and 5.7). On pitch down at $\alpha_- = 26°$, however, the counter-clockwise vorticity responsible for reattaching the flow is significantly weakened and the combined flow field at $\alpha_- = 8°$ resembles that of the second pair only at $\alpha_- = 17°$, corresponding to the delay in reattachment provided by the third mode pair, and necessary to accurately represent the data.

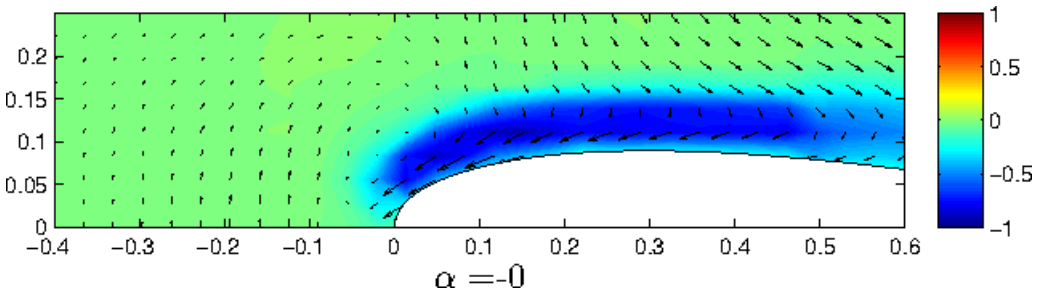

(a) First DMD conjugate pair at $\alpha_+ = 0$ on pitch up.

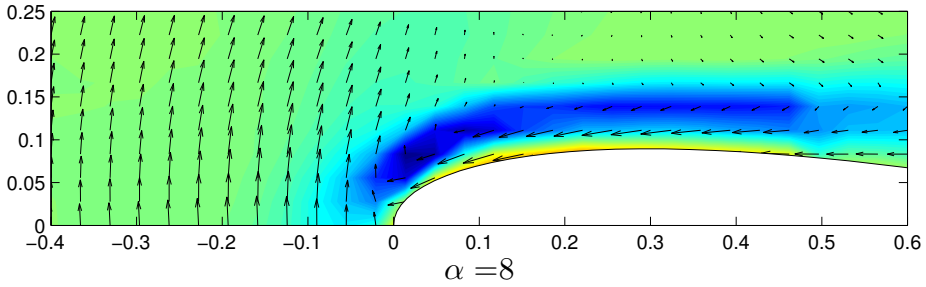

(b) First DMD conjugate pair at $\alpha_+ = 8$ on pitch up.

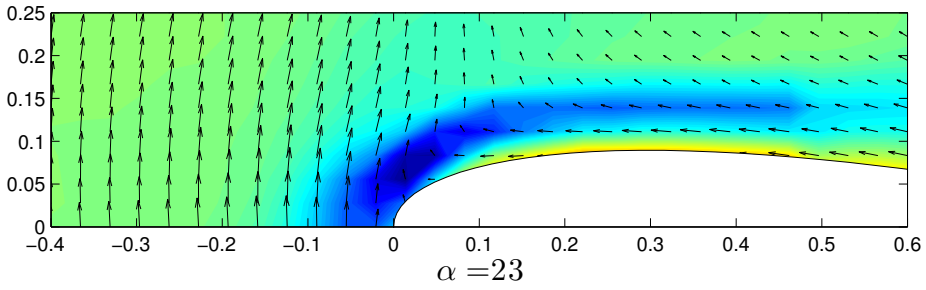

(c) First DMD conjugate pair at $\alpha_+ = 23$ on pitch up.

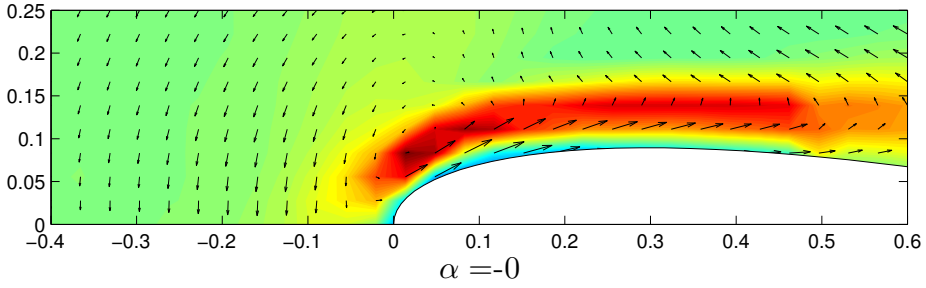

(d) First DMD conjugate pair at $\alpha_- = 0$ on pitch down.

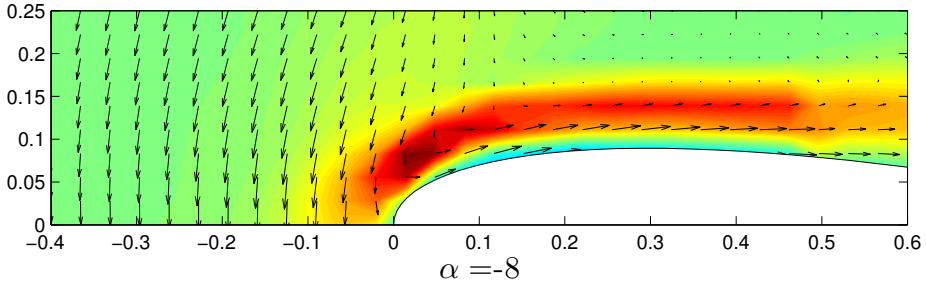

(e) First DMD conjugate pair at $\alpha_- = -8$ on pitch down.

Figure 5.10: Velocity (vector) and vorticity (contour) (scaled by maximum modal vorticity) plots of first DMD conjugate pair at pitch frequency Ω. Vortex structure at leading edge apparent in figures a and e. Maximum velocity magnitude ($\sqrt{u^2 + v^2} \sim 100\%$ of freestream velocity $\bar{U}$).

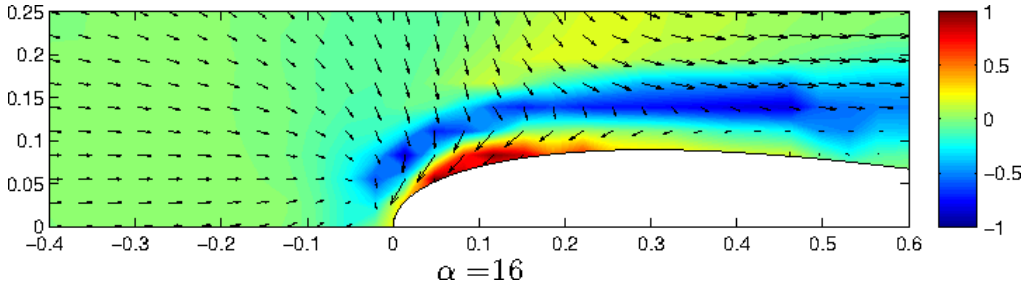

(a) Second DMD conjugate pair at $\alpha_+ = 16°$ on pitch up.

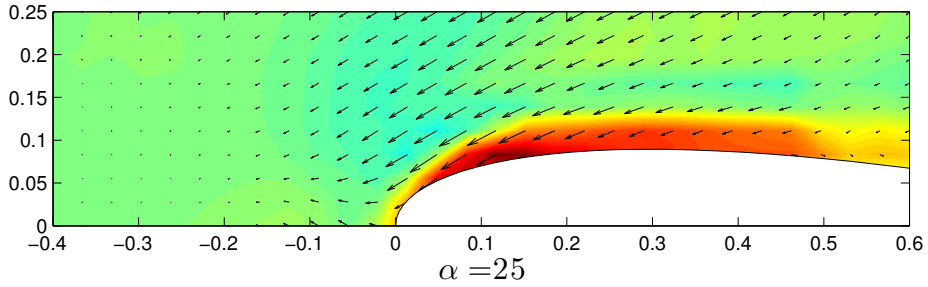

(b) Second DMD conjugate pair at $\alpha_+ = 25$ on pitch up.

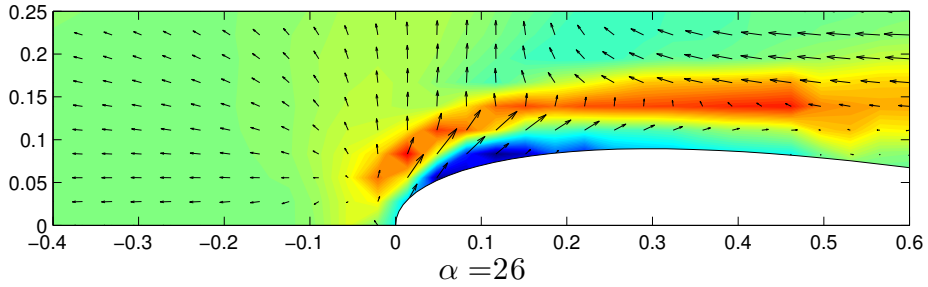

(c) Second DMD conjugate pair at $\alpha_- = 26$ on pitch down.

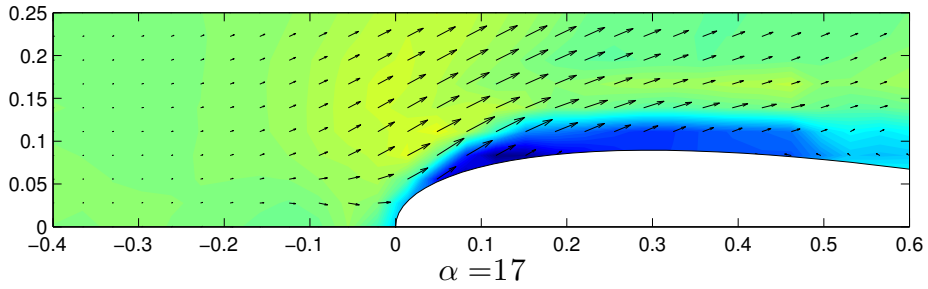

(d) Second DMD conjugate pair at $\alpha_- = 17$ on pitch down.

Figure 5.11: Velocity (vector) and vorticity (contour) (scaled by maximum modal vorticity) plots of second DMD conjugate pair at twice the pitch frequency Ω. Maximum velocity magnitude ($\sqrt{u^2 + v^2} \sim 44\%$ of freestream velocity $\bar{U}$).

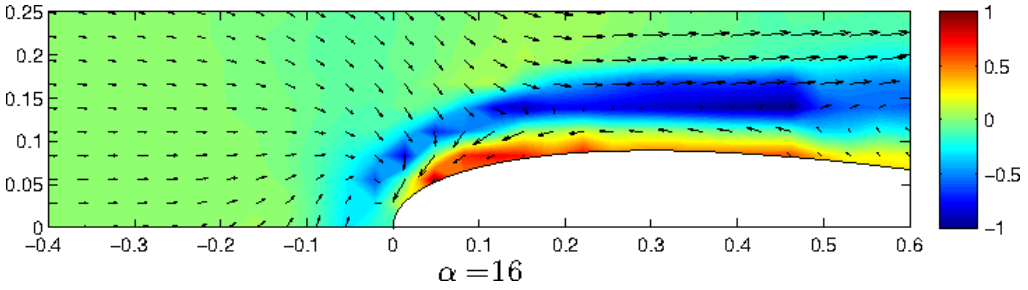

(a) Second and third DMD conjugate pairs at $\alpha_+ = 16°$ on pitch up

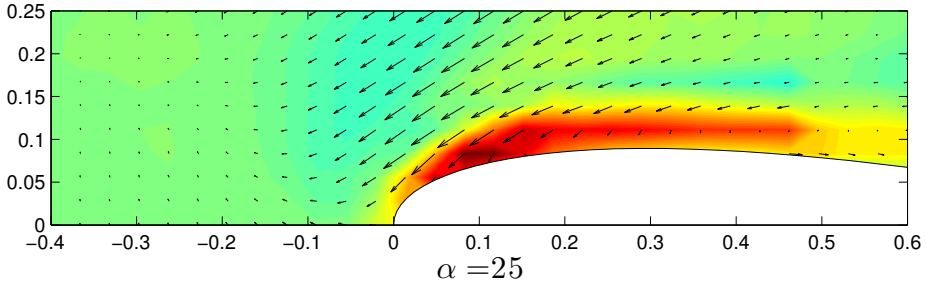

(b) Second and third DMD conjugate pairs at $\alpha_+ = 25°$ on pitch up

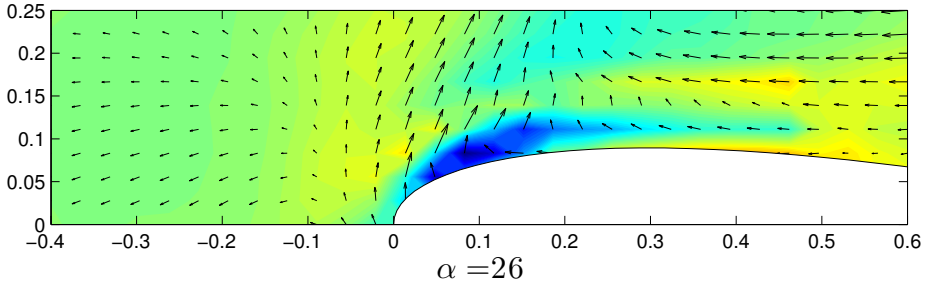

(c) Second and third DMD conjugate pairs at $\alpha_- = 26°$ on pitch down

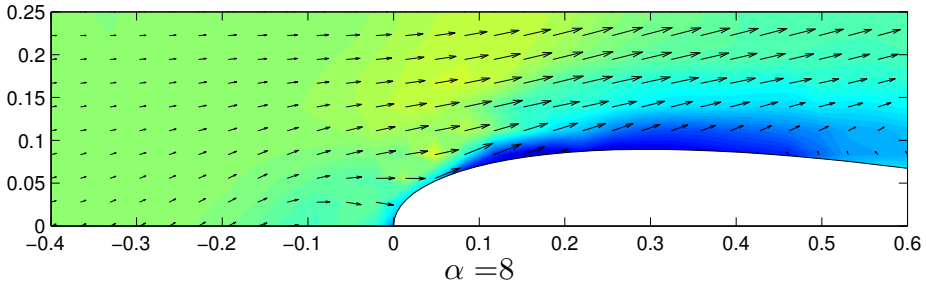

(d) Second and third DMD conjugate pairs at $\alpha_+ = 16°$ on pitch up

Figure 5.12: Velocity (vectors) and vorticity (contour), scaled by maximum modal vorticity, plots of the secondary separation mode ($\lambda_i = \pm 2\Omega$ and $\pm 3\Omega$) during pitch up and pitch down, respectively. Maximum velocity magnitude ($\sqrt{u^2 + v^2} \sim 27\%$ of freestream velocity $\bar{U}$).

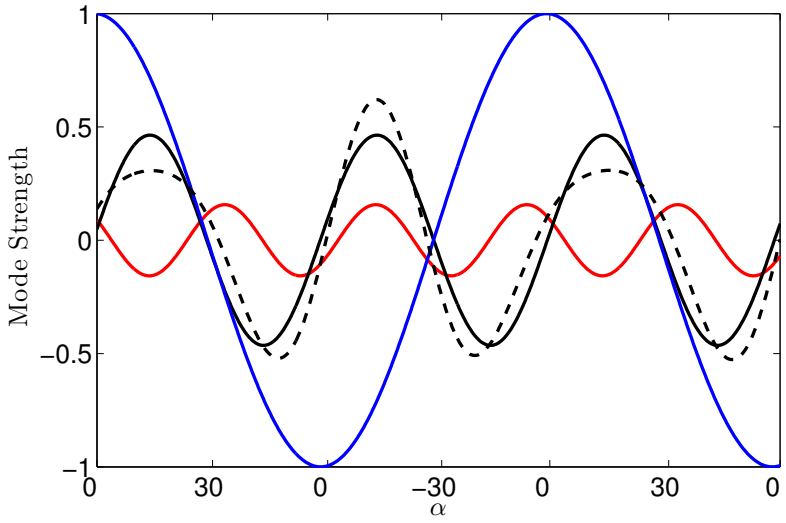

Figure 5.13: Time varying strengths of the mode pairs at the first three harmonics of the pitch frequency used in figure 5.7. $\lambda_i = \pm\Omega$ in blue $\lambda_i = \pm 2\Omega$ in black, and $\lambda_i = \pm 3\Omega$ in red. Combined second and third pair ($\lambda_i = \pm 2\Omega$ and $\pm 3\Omega$) plotted in dashed lines.

The phase relationship between the first two mode pairs shown in figure 5.13 is similar to that of the pitch/surge combined case. The first two pairs are approximately 90° out of phase with the mode at the pitch frequency maximum at $\alpha_+ = 0°$ and the modes at twice the pitch frequency just above zero. The additional mode pair required to represent the pitch-only flow at three times the pitch frequency begins initially out of phase with the pair at $\lambda_i = \pm 2\Omega$, acting in opposite directions during pitch up $\alpha_+ \geq 0°$. On pitch down, this pair lags the $\lambda_i = \pm 2\Omega$ modes, resulting in constructive interference late in the pitch down cycle $15° \gtrsim \alpha_- \gtrsim 0°$. The interaction of these two mode pairs causes a phase delay in the composite mode of the combined second and third pars moving the modal peak to $\alpha_- = 23.5°$ from $\alpha_- = 11.1°$ for the second mode only (dashed line in figure 5.13). This increased phase lag allows the model using three harmonics of the pitch/surge frequency to capture the reattachment point correctly (figure 5.7 and 5.8(a)) while the two-frequency model in figure 5.6 reattaches at too high an angle of attack. Therefore, the combination of the second and third mode pairs corresponds to the secondary dynamic stall mode, identified in Chapter 3, that drives reattachment.

5.3 Flow over surging airfoils

To analyze the surging motion isocontours at fixed angles of attack of $\alpha = 15°$ and $\alpha = 20°$ are shown in figure 5.14, where white lines represent the location of the experimental field of view, as

it moves around the airfoil. Points ζ and ϵ show the maximum forward and aft positions where the airfoil begins to move backward or forward, respectively, corresponding to maximum backward and forward flow acceleration in the airfoil reference frame. At the higher angle of attack ($\alpha = 20°$, figure 5.14(a)) the flow is fully separated over the entire period, and the vorticity isocontour highlights the shear layer between the recirculation region behind the airfoil and the freestream. Therefore, in this extreme case, surge motion has little effect on the flow other than the change in the freestream velocity, and corresponding strength of the shear layer.

At the lower angle of attack ($\alpha = 15$, figure 5.14(b)) there is significantly more variation in the flow field over the motion cycle. At maximum velocity (point A, turbine angle $\theta = 0°$) the isocontour follows the initial curvature of the airfoil and separates at about 50% chord. At this angle of attack, higher than the static stall angle $\alpha_{ss} \sim 11°$, the vorticity isocontour appears less smooth as vorticity is shed from the boundary layer. Furthermore, unlike the $\alpha = 20°$ case, the flow field is dictated by the direction of the airfoil motion. At point ζ, when the airfoil begins to move back, the isocontour smooths out somewhat and the separation point moves farther back toward the airfoil trailing edge. At point ϵ, when the airfoil begins to move forward, the opposite occurs, and the separation point moves forward. Figure 5.15 shows more detail, focusing on the portion of figure 5.14(b) after point ζ where the flow is initially attached over the first 75% of the chord, and then separates fully from the leading edge when the airfoil moves forward at ϵ.

5.4 Summary and conclusions

Phase-averaged measurements over independent sinusoidal pitching and surging motions at post-stall angles of attack $\alpha = 15,°$ and 20° were analyzed and compared to the combined sinusoidal motion discussed in Chapter 3. Isocontours of phase-averaged vorticity for all cases were shown over two periods of the airfoil motion to compare the dynamic separation behavior.

The flow over the pitching airfoil was shown to begin to separate somewhat earlier (at a lower angle of attack) than the combined pitch/surge case, while both reattached fully at $\alpha_- \sim 0°$. At a fixed angle of $\alpha = 20°$ the surging motion was seen to have negligible effect on the flow, with full separation from the leading edge present over the entire cycle. At $\alpha = 15°$ however the surge motion had an effect on the separation point, with surge forward causing the separation point to move toward the leading edge, and surge back moving it toward the trailing edge.

A leading edge vortex was identified in the pitch-only flow using the Γ criteria (Graftieaux et al., 2001). The LEV was shown to appear earlier in the pitch-only case as compared to the pitch/surge

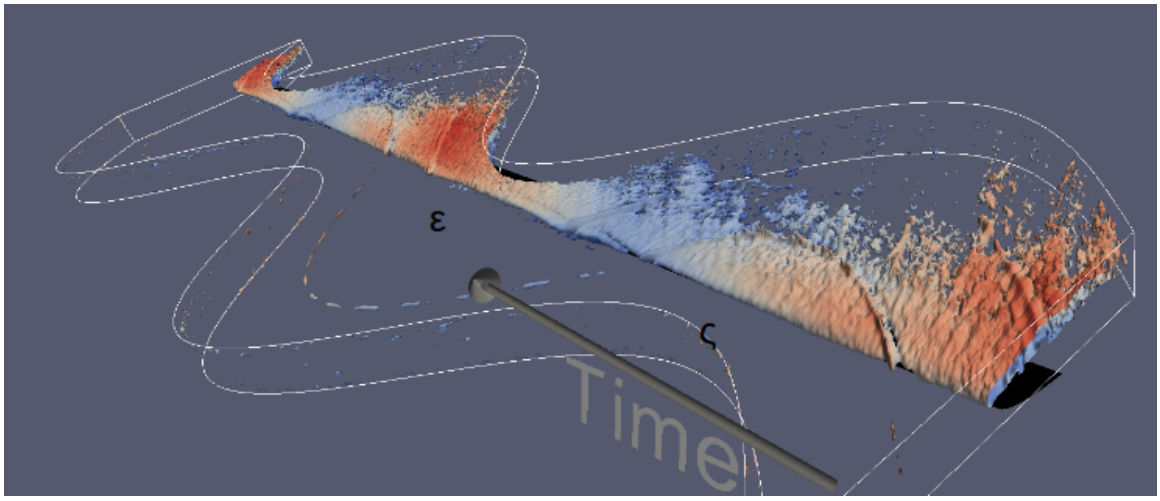

(a) $\alpha = 20°$

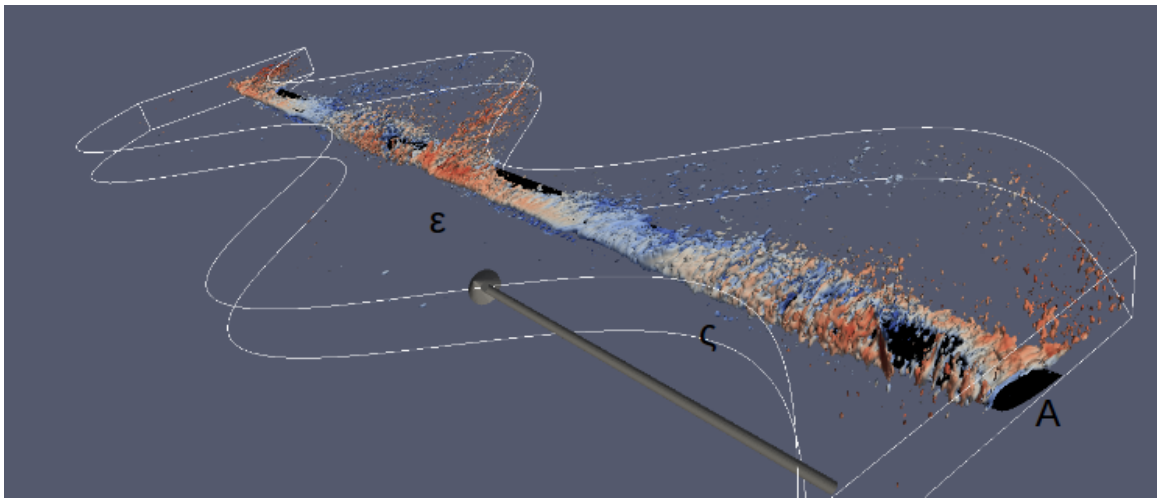

(b) $\alpha = 15°$

Figure 5.14: Vorticity isocontour for surging motion at $\alpha = 20°$ (top) and $\alpha = 15°$ (bottom) colored by velocity magnitude. Two periods shown starting at maximum surge velocity as in figure 5.1(a).

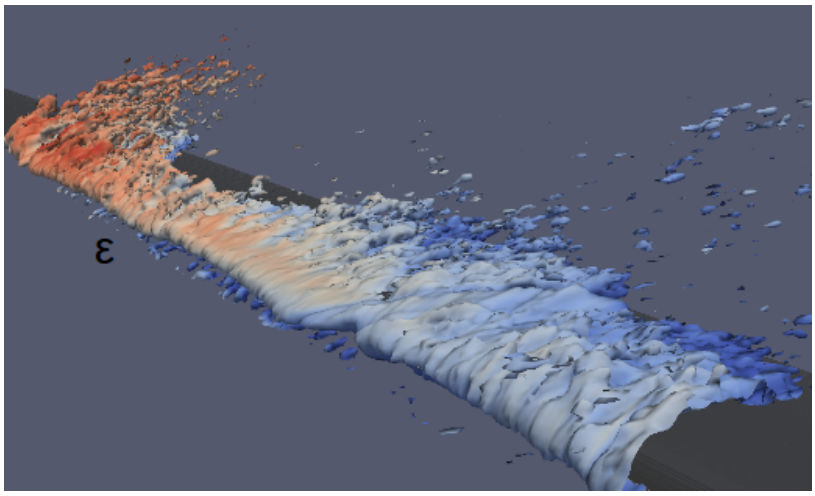

Figure 5.15: Vorticity isocontour for surge motion at $\alpha = 15°$ just after point ζ (figure 5.14(b)). Flow is seen to separate around point ϵ as the airfoil accelerates forward.

case, growing to be slightly stronger, and finally shedding from leading edge earlier, resulting in an earlier stall. The vortex was shown to develop in $\hat{T} \approx 4$ convection times corresponding to the optimal vortex formation time similar to the combined pitch/surge case. In the pitch only case, however, the vortex first appeared much earlier, at $\alpha_+ = 0°$, but the slower velocity relative to the airfoil U resulted in a only slightly earlier separation point. Although the combined pitch/surge flow is much more complicated than a linear combination of the effects from pitch and surge separately, these results suggest that deceleration of the flow (relative to the airfoil) from the surging motion has a stabilizing effect on LEV dynamics in the combined pitch/surge flow. As such the appearance of a coherent vortex is delayed during pitch up, resulting in a delay in dynamic stall in the pitch/surge case relative to the pitch-only.

A low-order model of the flow over the leading edge was assembled using the dynamic mode decomposition. Seven modes, including a time-constant base flow, and the first three harmonics of the pitching frequency Ω, were shown to be sufficient to capture the qualitative behavior of the flow over the pitching wing. This is in contrast to the combined pitch/surge flow, which was amenable to a model using only five modes and three frequencies. Comparing five- and seven-mode representations of the pitch-only flow showed that while the five-mode reconstruction was able to capture the separation point adequately, the shape of the separated region and the reattachment behavior were not accurately captured without the additional mode pair at $\lambda_i = \pm 3\Omega$.

Detailed analysis of the mode pair at the pitch frequency found that a vortical structure appeared at the leading edge and convected toward the trailing edge, leading separation. This mode structure

was in good agreement with the primary separation mode of the pitch/surge combined flow presented in Chapter 3, but the appearance of the structure associated with separation appeared earlier in the pitch cycle, corresponding to the earlier separation observed in the pitch-only flow. The structure associated with the mode pairs at twice and three times the pitch-frequency identified a similar structure to the secondary separation mode developed for the combined pitch/surge flow, resulting in a clockwise vortex that appeared near the leading edge on pitch down that led reattachment. As such the physical basis of this seven-mode model is the same as that of the five-mode combined pitch/surge model; however, it requires a higher frequency mode pair to accurately represent the reattachment behavior provided by the secondary separation mode. This result suggests that similar to the pitch/surge case the pitch frequency dominates the flow development, and the physical mechanisms responsible for separation and reattachment are linked to the motion frequency and dominated by the pitch motion.

Analysis of the phase relationship between the DMD mode pairs at the three harmonic frequencies provided insight into the differences between the pitch and pitch/surge flows, resulting in the requirement of a higher order model to capture the features of the pitch-only flow. Initially during pitch up, ($0^\circ \leq \alpha_+ \leq 30^\circ$) mode pairs at two and three Ω interact destructively, limiting the effect of the secondary separation mode, and allowing the primary separation mode to dominate the separation process. On pitch down the third mode pair adds a phase delay into the combined secondary separation mode. This phase delay pushes the reattachment point to a lower angle of attack than seen with the second mode pair only and is necessary to accurately model the separation region.

The results presented in this chapter show that the deceleration motion caused by the surge, which occurs during pitch up in the VAWT, effectively stabilizes the flow permitting a later LEV formation and corresponding to a delay in dynamic stall. The basic physics of dynamic stall, however, is shown to be similar, and dominated by a primary and secondary separation mode. In the pitch-only case the accelerated separation due to a phase lead of the primary separation mode necessitates a third frequency at three times the pitch frequency to be added to the secondary separation mode to induce a delay in reattachment and accurately capture the flow. Analysis of the effect pitch and surge separately demonstrated that the physics of separation for airfoils undergoing arbitrary unsteady motions including dynamic pitch is associated with the pitch kinematics, while the other motions act to alter the phase relationship between the separation modes.

Chapter 6

Extrapolation of Results to Vertical Axis Wind Turbines

In this chapter results from experiments on the pitching and surging airfoil from both phase-averaged and instantaneous data sets described in section 2.3.1 are compared to simulations performed by Tsai and Colonius (2014) to investigate the effect of the rotating frame and the associated Coriolis force on the flow-fields described here. These computations were performed in both the vertical axis wind turbine frame as well as the linear pitch/surge frame, used in experiments but at a low Reynolds number of 1,500. To distinguish between the experimental dataset and the computational data sets (provided by and published in Tsai and Colonius (2014)) the nomenclature EPM^E and EPM^C are introduced to denote equivalent planar (pitch/surge) motion from experiment and computation, respectively, and VAWT^C to denote the full turbine frame including Coriolis force from computation. The results from the combined pitch/surge experiment (EPM^E) are wrapped back into the vertical axis wind turbine frame and compared to the VAWT^C computations to analyze further the differences in the turbine relative flow field imposed by the change in reference frame used in this thesis. Finally, the implications of the flow measurements on a representative three-bladed VAWT are explored.

The primary contribution of this chapter is the understanding of the reference frame effects imposed in converting between the linear pitch/surge frame and the rotational VAWT frame. This comparison gives indications of how the flow field could be altered to improve the performance of the turbine as a whole. This work was presented as a collaborative effort between the author with advisor Beverley McKeon, and collaborators Hseih-Chen Tsai and Tim Colonius at the International Conference on Wakes, Jets and Separated Flows in June, 2015, Stockholm, Sweden, and is published, in part in the conference proceedings Dunne et al. (2015) and in Dunne and McKeon (2015b).

6.1 Flow field comparison with computational results and the effect of the Coriolis force

To explore the flow field variation between high Reynolds number experimental data (EPM^E) and the lower Reynolds number computations of Tsai and Colonius (2014) in both reference frames (EPM^E and VAWT^C), the vorticity is plotted in the lab frame at various phases of the airfoil motion in figures 6.1 - 6.4. The lower Reynolds numbers in the simulation result in much more coherent vortices appearing at all angles of attack. The coherent vortex shedding apparent in the computations is not exactly coupled to the airfoil phase and therefore is smeared out in phase-averaged experimental results. In instantaneous realizations of the flow at pre-stall angles of attack (figure 6.1), however, such vortex shedding was observed from the trailing edge at the high experimental Reynolds number as discussed in Chapter 4. At very low angles of attack periodic vortex shedding cannot be observed in the instantaneous experimental results since the shedding has not had sufficient time to develop after reattachment, as discussed in Chapter 4. At higher pre-stall angles of attack, however, periodic shedding is observed. These shed vortices convect directly downstream with little interaction between the vortices, while in both computational datasets (EPM^C and VAWT^C) the shed vortices appear to interact and move in the cross-stream y direction somewhat at $\alpha_+ = 19°$. This difference is caused by the increased Reynolds number in the experiments, resulting in much less coherent vortices being shed; as a result, the vortices are weaker than those seen in computation, and do not exhibit significant enough interaction to cause vortex induced motion in the cross-stream direction.

The phase-averaging of the experimental data in figure 6.2 significantly weakens the positive (counter-clockwise) vorticity at the airfoil surface due to the interaction of the recirculation region and the airfoil surface after separation. However, in computation as well as instantaneous measurements (figures 6.2 and 6.4) similar counter-clockwise vorticity is observed at post stall angles of attack ($\alpha = 30°$ and $\alpha_- = 24°$, as well as at high angles of attack prior to stall (figures 6.1 and 6.3). In post-stall flow-fields the wake in the instantaneous experimental data is characterized by much smaller, less organized, structures than the computation as is expected due to the significantly higher Reynolds numbers.

Apart from these Reynolds number and experimental differences the flow evolution is fairly similar between the three cases. Initially at $\alpha_+ = 0°$ the flow is attached and a symmetrical wake can be seen behind the airfoil. At $\alpha_+ = 19°$ a leading edge vortex begins to form, visible as a distinct structure in computation and indicated by increased vorticity intensity in experiment. At this point

the flow remains attached without a large reversed region behind the airfoil. In the experimental results at $\alpha_+ = 27°$ the LEV appears even stronger, having just shed from the leading edge. In computations of both VAWT^C and EPM^C, however, the LEV has moved downstream, indicating that flow separation occurrs slightly later at full-scale Reynolds numbers. At maximum $\alpha = 30°$ the flow is fully separated in both experiment and computation, resulting in a shear layer between stagnant and freestream flow in the experiment and large scale vortex shedding from leading and trailing edge continuing in the computation. In the experiments the larger wake (with cross stream size on the order of the airfoil cross-stream projection, $c \sin \alpha$), indicated by the vorticity caused by the shear between the stagnant wake and the freestream, does not extend as far downstream as in the computation due to the later separation in experiment. Slight differences can be seen in the trajectories of the shed vortices between the EPM^C and VAWT^C frames with a vortex pair moving up away from the airfoil in the linear frame, and two distinct but opposite vortices moving downstream in the rotating frame. In the experiments, the wake remains behind the airfoil with no deviation in the y direction due to the weaker interaction between shed vortices. Finally, on pitch down at $\alpha_- = 24°$ the VAWT computation shows two vortices adjacent to the airfoil, while in the linear frame vortices can be seen to shed from the leading and trailing edges, then convect away from the airfoil. More detail of this wake-capture phenomenon can be found in Tsai and Colonius (2014).

6.2 Extrapolation of experimental results to vertical axis wind turbine frame

Armed with the simple model of the coherent vortex activity associated with VAWT blade motion, results from the simple pitch/surge model can be reinserted into the rotating turbine frame. This extrapolation can be compared to the vertical axis wind turbine computation of Tsai and Colonius (2014) (VAWT^C) to identify relative motion of the flow structure and the blades in a typical VAWT. Such an extrapolation neglects any influence of blockage created by the VAWT, which would enhance apparent bluff body features associated with the VAWT wake as investigated by Araya and Dabiri (2015). Clockwise vorticity contours from EPM^E experiment are superimposed onto a VAWT blade rotating clockwise at $\theta = 70°, 90°, 108°$, and $133°$ based on their apparent angle of attack in the top of figure 6.5 (see figure 1.1 for the exact comparison of VAWT and airfoil motion).

At $70°$ the flow is fully attached, at $90°$, and a strong vorticity peak at the leading edge caused

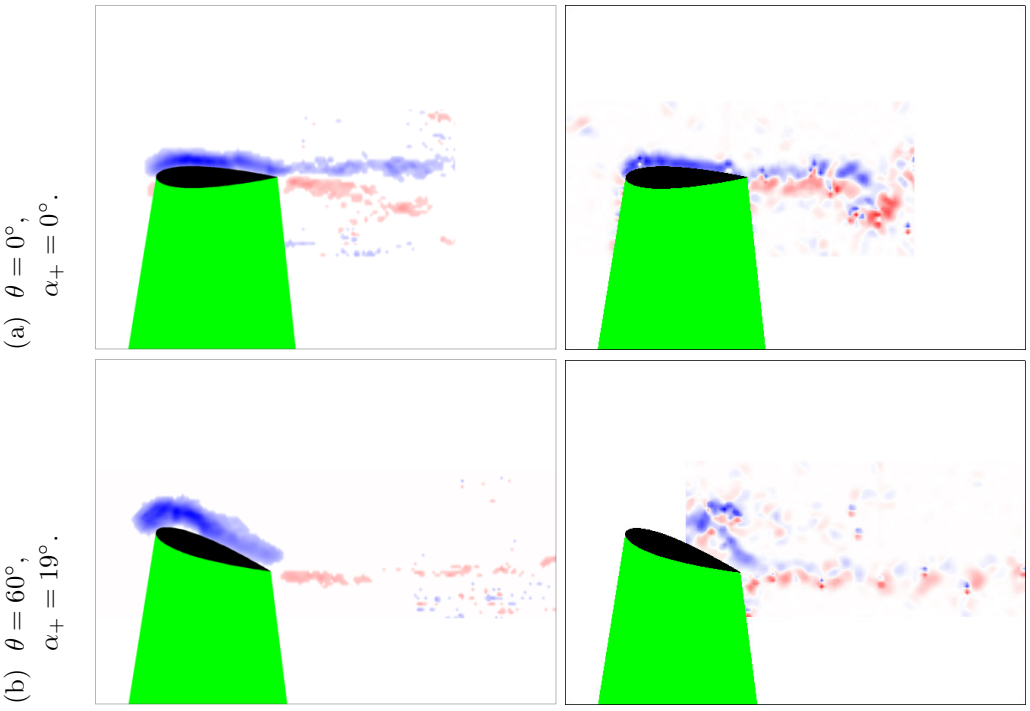

Figure 6.1: Vorticity contours from experiment. Phase-averaged realization (left) and instantaneous (right) from the aft field of view. In the instantaneous realization at $\alpha_+ = 19°$ the measurement is cut off over the leading edge due to the aft field of view. Red and blue contours indicate positive and negative vorticity, respectively. The green area indicates the PIV laser shadow.

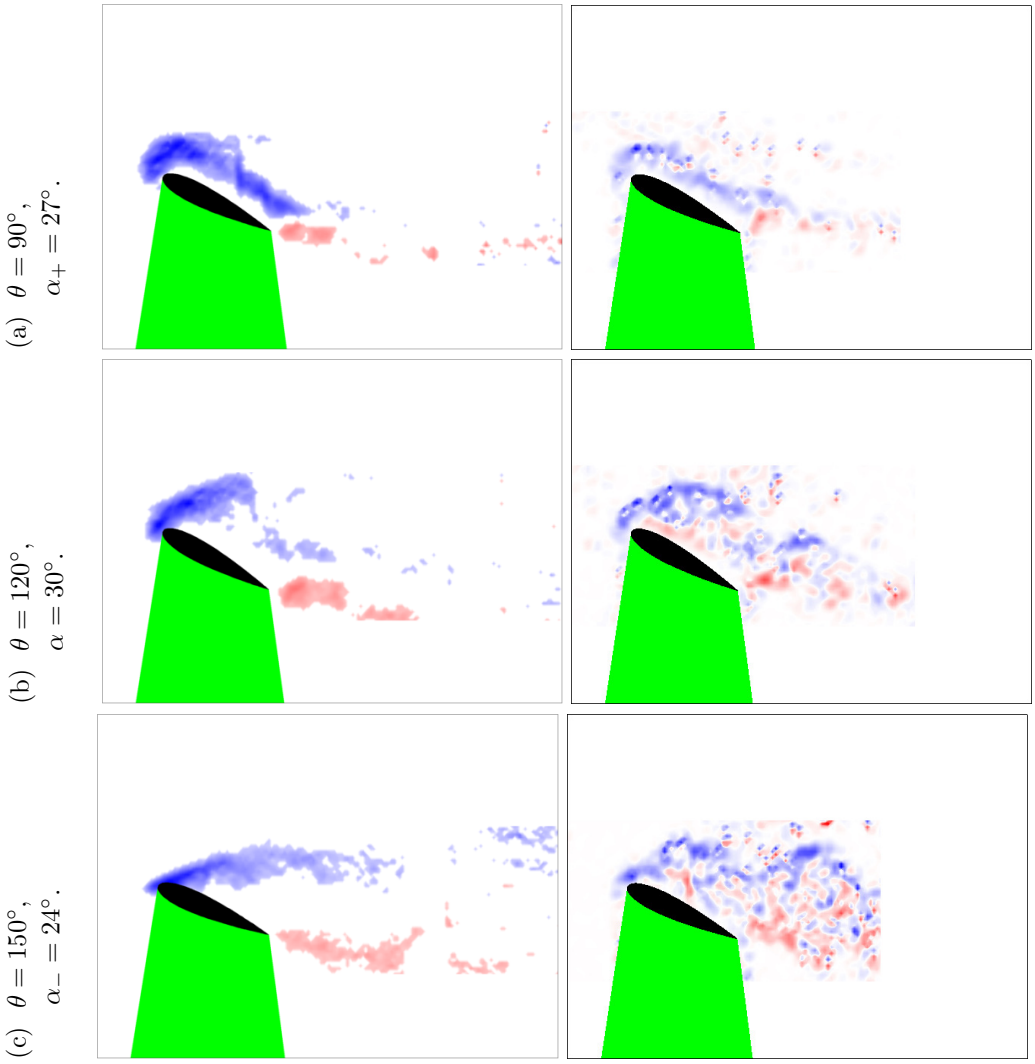

Figure 6.2: Vorticity contours from experiment. Phase-averaged realization (left) and instantaneous (right) from the front field of view. Red and blue contours indicate positive and negative vorticity, respectively. The green area indicates the PIV laser shadow.

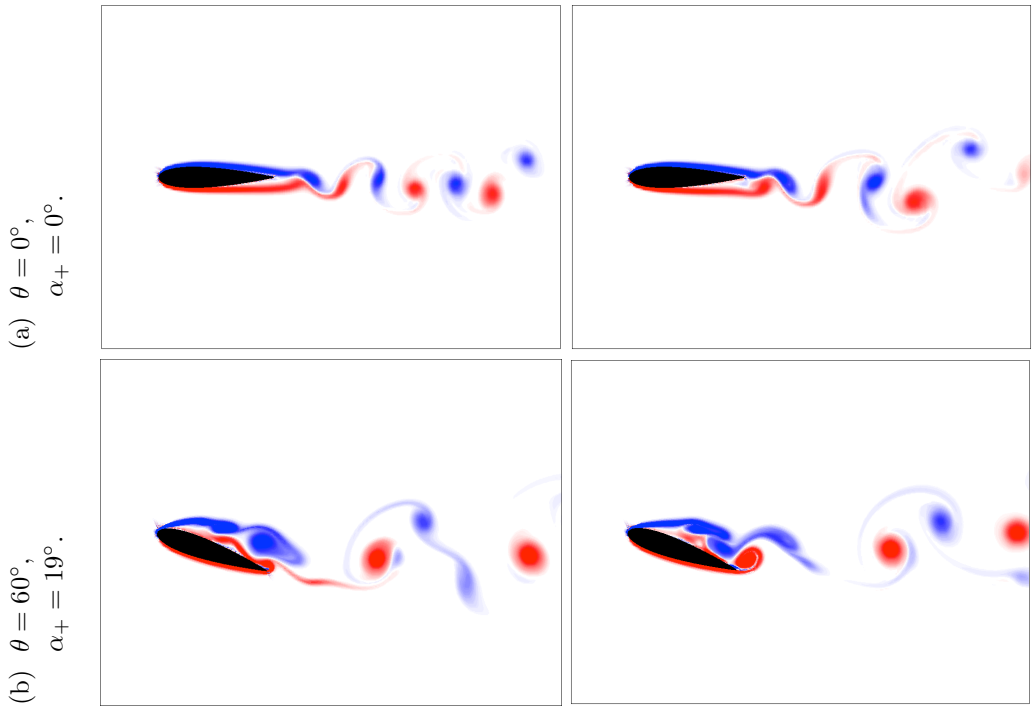

Figure 6.3: Vorticity contours from the computations of Tsai and Colonius (2014) at the same angular location as the experiment in figure 6.1. Planar motion EPM^C (left) and turbine frame VAWT^C (right). Red and blue contours indicate positive and negative vorticity, respectively.

by the interaction of both primary and secondary modes indicates the growth of an LEV. By 108° the LEV has shed and the flow begins to separate, and finally at 133° the flow is fully separated. This suggests maximum lift force (and associated torque on the turbine) between 90° and 108°, followed by lift stall and a significant loss of lift after $\theta \sim 110°$; the direct relationship between LEV development and lift was observed directly by, e.g., Carr et al. (1977) and Jones and Babinsky (2010).

Contours from VAWT^C simulation at the same turbine angle θ (bottom of figure 6.5) show more coherent vortices, as expected due to the lower Reynolds number. In the experimental results some negative vorticity is apparent behind the airfoil (in the airfoil reference frame). This vorticity is shed from the airfoil during the motion; as such, it is no longer connected to the airfoil and convects with the airfoil relative freestream U in the experimental frame, while the shed vortices from VAWT^C computation convect with the turbine relative freestream U_∞, left to right in the turbine frame. The results of the extrapolation of the EPM^C experiments presented in this thesis therefore apply during LEV formation and shedding, but the true shed vortex trajectories and their effect on the downstream blades ($\theta > 180°$) cannot be measured without consideration of the Coriolis effect and the direction of convection. Note, however, that the coherence of the shed vortices observed in the

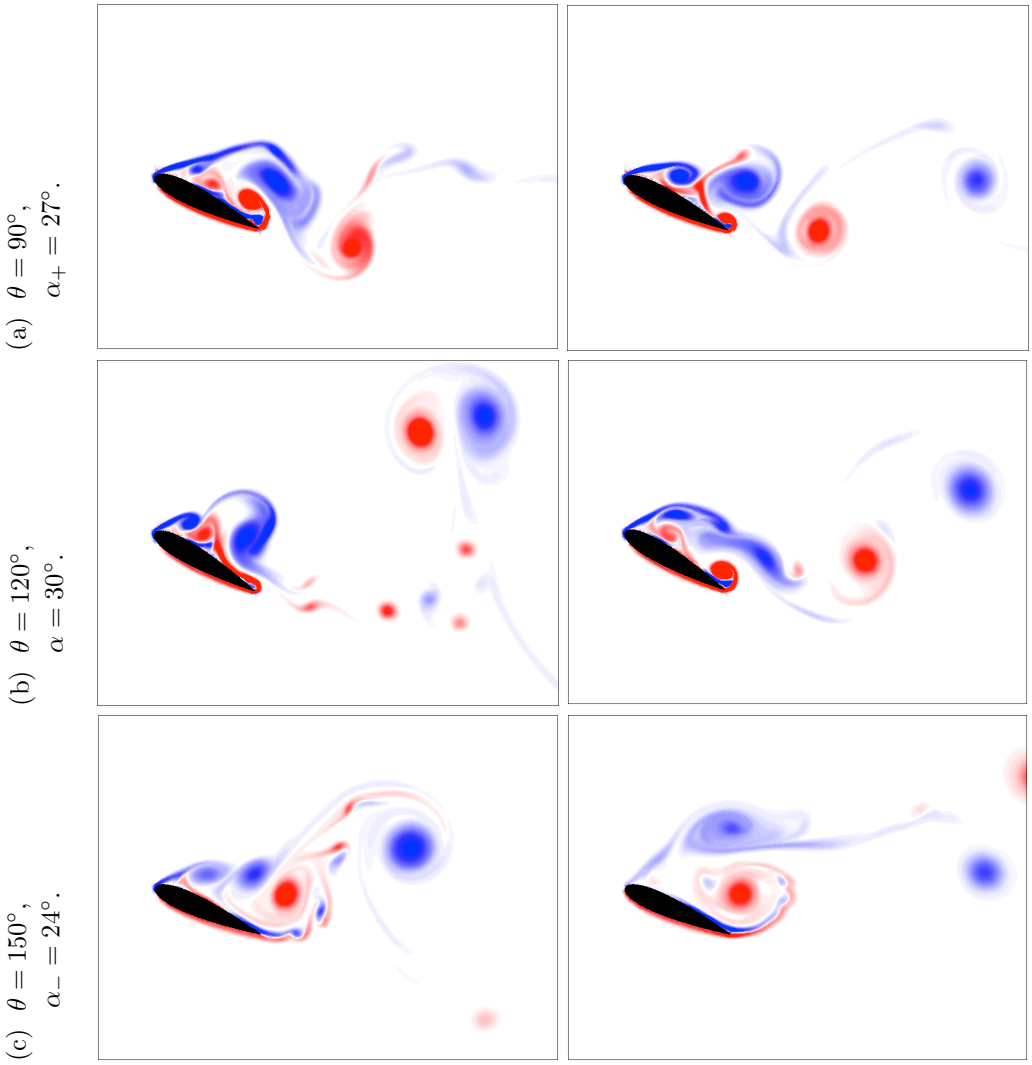

Figure 6.4: Vorticity contours from the computations of Tsai and Colonius (2014) at the same angular location as the experiment in figure 6.2. Planar motion EPM^C (left) and turbine frame VAWT^C (right). Red and blue contours indicate positive and negative vorticity, respectively.

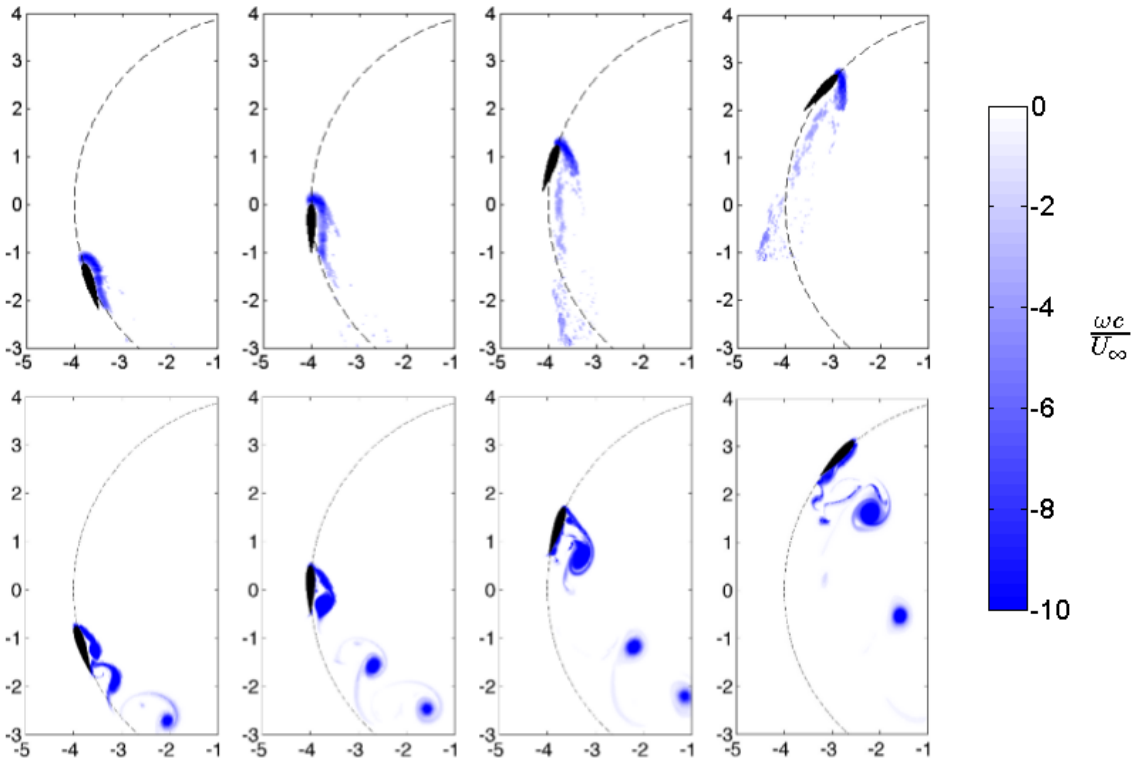

Figure 6.5: Clockwise vorticity contours from experiment (EPM^E) (top) and VAWT computation (VAWT^C) (bottom from Tsai and Colonius (2014)) at $\theta = 70°$, $90°$, $108°$, and $133°$, respectively, from left to right.

computations is not present at the experimental Reynolds numbers, suggesting that the impact of the differing trajectories may be less than expected. Leading edge vortex shedding and subsequent separation between $\theta = 108°$ and $\theta = 133°$ as seen in figures 18 (c and d) may provide some insight into the vortex capture effect seen when the Coriolis effect is included, e.g. Tsai and Colonius (2014b). In the turbine frame, a vortex shed near this angle θ will convect downstream adjacent to the VAWT airfoil path (bottom of figure 6.5) and can be effectively captured by the airfoil. While the pitch/surge experiment cannot fully investigate this behavior, it demonstrates the possibility of such an effect occurring based on trajectory considerations, due to the location (in the turbine frame) of LEV separation. The comparison of the experimental pitch/surge results in this thesis and the computations of Tsai and Colonius (2014) demonstrate that the effect of the reference frame change utilized in the experiment is to alter the trajectory of shed vortices. However, at the blade level and immediately behind it, agreement is good between the EPM^E pitch/surge experiments and the VAWT^C computations.

The multiple physical phenomena and associated time scales developed in Chapter 4 are in effect in specific portions of the VAWT rotational cycle. The simple schematic in figure 6.6 illustrates the influence of dynamic stall for approximately the first two thirds of the upstream cycle, separation for the final third, and trailing edge shedding beginning at $\theta = 0°$ with LEV development during the maximum upstream position. This figure effectively wraps the flow regimes illustrated in the time-extruded frame in figure 4.19 into the VAWT frame. It is clear from this schematic that vortex shedding associated with the third timescale (section 4.3) is in effect while the blade is advancing. As such, there will be high frequency forcing on this half of the turbine as well as potential interaction of the small-scale vortical wake with the turbine structure associated with the following blades. The leading edge vortex development associated with the second, vortex formation timescale is in effect near the maximum upstream position of the blade. Furthermore, the end of this regime associated with LEV and TEV shedding from the airfoil continues significantly past $\theta = 90°$, placing the shed structure in the correct position to convect downstream adjacent to the receding blade, as shown above and in good agreement with the computations of Tsai and Colonius (2014). Finally, the reattachment and fully separated flow appear in the final third of the upstream half of the turbine cycle ($120° \leq \theta < 180°$). This regime is characterized by broadband shedding from the stalled airfoil. In addition, the reattachment behavior associated with the pitch/surge frequency is characterized by the two dynamic separation modes at the first two harmonics of the pitch/surge frequency as developed in Chapter 3.

Referring to figure 2.4 we can relate the rotational velocity $\dot{\alpha}$ and acceleration $\ddot{\alpha}$ to the flow phenomenon. During the vortex shedding regime (magenta in figure 6.6) the angle of attack is increasing; however the rate of change is decreasing. Due to this motion in the linear frame the trailing edge is moving downward relative to the freestream (at decreasing velocity), likely resulting in a decrease in clockwise vorticity in the shed vortices as discussed in section 4.3. In the rotating turbine frame this motion of the trailing edge, caused by the pitch, would not be apparent, and therefore the circulation would be more similar between clockwise and counter-clockwise vortices. During vortex development (red in figure 6.6) the rotational velocity is small and decreasing as the airfoil approaches maximum angle of attack; however, the rotational acceleration of the airfoil is strongly negative as it slows prior to pitch down. In this regime the effect of the airfoil motion is minimal, but instead the LEV is entraining vorticity similar to an airfoil at a fixed angle of attack, as the flow is forced to rotate around the leading edge. In the dynamic stall development regime (green in figure 6.6) the airfoil is initially at zero angle of attack, with rotational velocity that slows down to a near stop when the flow stalls fully prior to maximum α. During the separated flow regime the airfoil is pitching back down (negative $\dot{\alpha}$) and the trailing edge is accelerating back into the separated region behind the airfoil until flow reattachment at $\alpha_{-} = 0°$.

The relative location of blades in a three-bladed VAWT was examined and inferences were made about the effects of dynamic stall on turbine performance on a blade-by-blade basis. The flow field on each blade of a standard three-bladed turbine is shown for two phase angles of $\theta = 30°$ and $60°$ in figure 6.7. At $\theta = 30°$ two of the three blades are in the upstream half of the turbine. One blade at $\theta = 150°$ is fully separated and the other at $\theta = 30°$ is at a low angle of attack $\alpha \sim 10°$. From this projection it is clear that when the unsteady effects of LEV growth and shedding are apparent on any blade, that blade is the only one in the upstream half of the turbine as in figure 6.7(b). Note that performance has only been extrapolated to the upstream half of the turbine cycle, since it has been shown that power production in the downstream half deteriorates severely due to the combined influence of the impact of the unsteady wakes behind other blades and the turbine support and the corresponding reduced effective velocity reaching the downstream blades (Islam et al., 2007).

6.3 Summary

Results from phase-averaged and instantaneous measurements on the combined pitching and surging airfoil developed in Chapters 3 and 4 were extrapolated back to the rotating vertical axis wind turbine frame to investigate the radial location θ where each flow phenomena took place. These sinusoidal

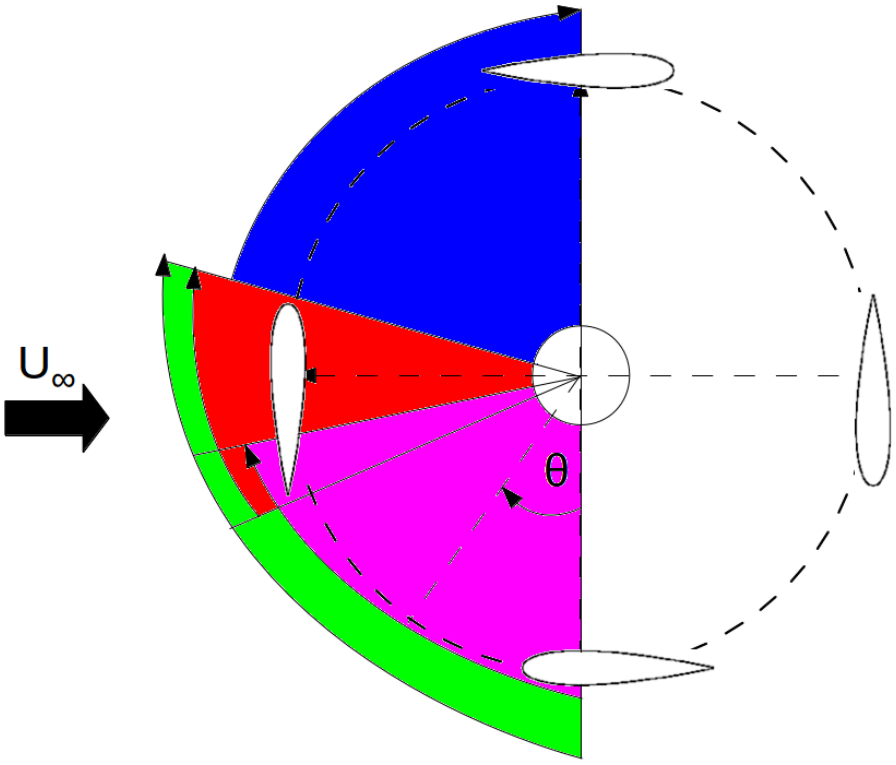

Figure 6.6: Dynamic stall regimes from 4.19 in VAWT frame. Dynamic stall development (green), trailing edge vortex shedding (magenta), leading edge vortex development (red), and separated flow (blue).

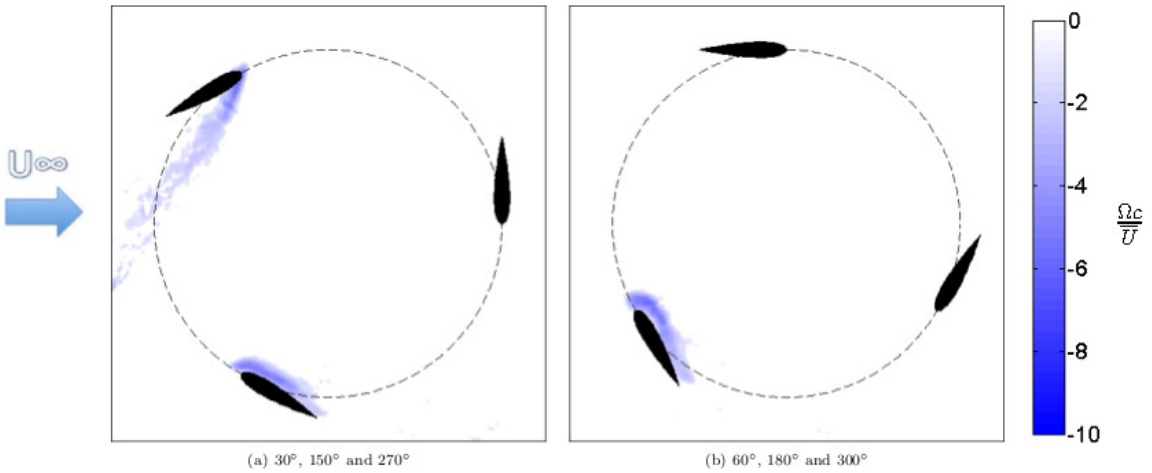

Figure 6.7: Clockwise vorticity contours on the upstream half of a representative three-bladed turbine turbine.

results were fit to the VAWT frame by matching the angle of attack of a VAWT at the same tip speed ratio η. The flow fields were then compared to immersed boundary computations at a low Reynolds number by Tsai and Colonius (2014), who investigated the effect of Coriolis force on the turbine blade not present in the experiments.

Direct comparison of the flow field relative to the airfoil showed that the average flow field developed very similarly between the experiment (EPM^E) and computational results in both the equivalent planer pitch/surge motion (EPM^C) and the turbine frame (VAWT^C) prior to flow separation. In this regime the most significant differences were much smaller, less coherent structure shed from the airfoil in experiment due to the significantly higher Reynolds number. After separation the direction of convection of the shed vortices differed somewhat; however, the flow development at the blade level had good agreement across the entire airfoil motion cycle.

Analysis of the results in the rotating VAWT frame demonstrated a clear difference in the trajectory of shed vortices in the pitch/surge and turbine reference frame due to the differing freestream velocity relative to structures that are no longer affected by the airfoil. In the experiments the shed vorticity convected downstream in the airfoil relative frame, while in the VAWT computation vortices were shown to convect downstream in the turbine frame. The location in the VAWT cycle where the LEV is shed causes the vortex to move downstream near the airfoil in the wind turbine frame, allowing for the vortex-capture effect noted by Tsai and Colonius (2014). Finally, the location of each timescale regime demonstrated in Chapter 4 was investigated. This analysis was consistent with the LEV shedding in a location where it would interact with the blade on the receding side of the turbine rotation $\theta \geq 90°$, as discussed in section 4.3. Periodic vortex shedding dominated by classical Strouhal scaling occurred on the advancing blade $0° \leq \theta < 90°$. Finally the flow field was extended to a standard three-bladed turbine to highlight how each flow phenomenon may interact on a full turbine.

6.4 Opportunities for VAWT design

Wrapping the physical phenomena identified in this thesis back into the rotating VAWT frame provides insight into how each of these effects may interact with the full-turbine structure and permits speculation into opportunities to improve the performance of VAWTs. Numerous authors have utilized active flow control or active pitch control to curtail dynamic stall (section 1.2.2) and this work has effectively been applied to VAWTs as discussed in section 1.2.2.1. These active techniques, however, naturally increase the complexity of VAWTs, negating the advantage of the

inherent simplicity of the VAWT design. Instead we suggest the possibility of altering the relationship between the flow timescales developed here to improve performance without altering the base VAWT design.

Perhaps the most attractive of these opportunities is to attempt to delay the lift (and associated torque) drop after the LEV sheds from the airfoil to a higher θ, ie. further around the airfoil cycle. As discussed by Rival et al. (2009), LEV separation will occur at maximum angle of attack, (when the arifoil changes direction) or, as shown in chapter 4, four convective times after the LEV forms. Therefore it is possible that higher overall turbine torque could be achieved if four convection times took place exactly when the airfoil reached maximum angle of attack. In this situation the unsteady lift benefits of the LEV will be applied over the entire cycle, potentially resulting in higher torque. It is likely, however, that any changes in airfoil geometry or kinematics will have other effects on the flow. Therefore, what follows should be considered an outline of the options to alter the flow to take advantage of the optimal vortex formation theory, but it does not provide an exact roadmap for the design of a VAWT.

In general the airfoil convection time for a VAWT blade is given by:

$$\hat{T} = \int \frac{U}{c} dt = \int \frac{U_\infty}{c} \sqrt{1 + 2\eta \cos\theta(t) + \eta^2} dt. \tag{6.1}$$

This equation can be integrated analytically resulting in a complex expression involving the elliptic integral of the second kind. For the conditions presented here, corresponding to a turbine with tip speed ratio $\eta = 2$ and reduced frequency $k = \frac{\omega c}{2\eta U_\infty}$, the convection time during pitch up is:

$$\hat{T}_+ = \int_{\theta(t)=0^\circ}^{\theta(t)=120^\circ} \frac{U}{c} dt = \int_{\theta(t)=0^\circ}^{\theta(t)=120^\circ} \frac{U_\infty}{c} \sqrt{1 + 2\eta \cos\theta(t) + \eta^2} dt = 11.15, \tag{6.2}$$

where $\alpha = \alpha_{max} = 30^\circ$ at $\theta_{max} = 120^\circ$ for the VAWT blade motion. In the experiments presented here the leading edge vortex was shown to appear at $\alpha_+ \sim 15^\circ$ resulting in a total convection time after vortex nucleation of:

$$\hat{T}_{LEV} = \int_{\theta(t)=46^\circ}^{\theta(t)=120^\circ} \frac{U}{c} dt = 6.25. \tag{6.3}$$

Which is in good agreement with the qualitative observation that LEV separation occurred prior to maximum α.

The formation time between LEV initiation and max angle of attack $\hat{T}_{LEV}$ can be decreased by increasing the chord length, resulting in a corresponding increase in Reynolds number and reduced

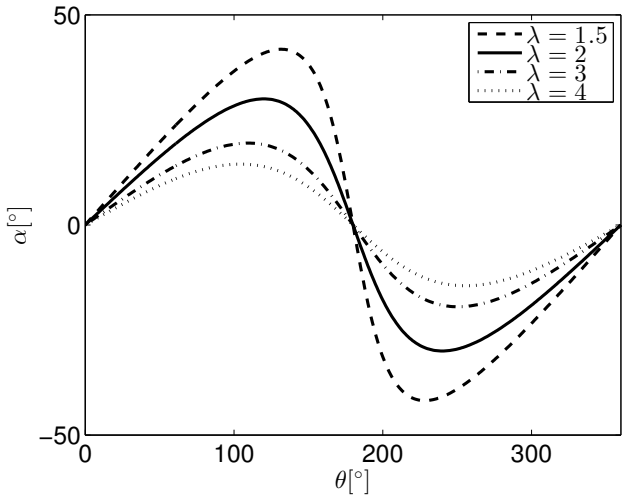

Figure 6.8: Angle of attack of VAWT at various tip speed ratios η.

frequency, or by increasing the tip speed ratio η, resulting in a lower maximum angle of attack that occurs at a lower turbine angle θ as seen in figure 6.8. Such an increase in η would additionally result in a higher Reynolds number, and a decreased reduced frequency k. These results provide a suggestion for possible design improvements for VAWTs for fixed freestream velocity U_∞. While adapting the motion to permit optimal vortex formation does not, in general, guarantee an increase in turbine torque adjusting the turbine in this way should produce a more aerodynamically efficient overall design. The effect of the changes in reduced frequency, Reynolds numbers and other parameters on the inherent dynamic stall and vortex formation behavior must be investigated however to determine their effect on the unsteady flow.

Another option is to improve the performance of of VAWTs by adjusting the basic design, promoting leading edge vortex separation earlier in the rotation cycle. The results of Tsai and Colonius (2014) show that vortex convection adjacent to the airfoil during the receding portion of the cycle decreases the lift provided by the turbine blade. As such, if the vortex could be shed completely from the airfoil near $\theta = 90°$, it would be less likely to interfere further along in the cycle. To cause the LEV to convect away from the airfoil at $\theta = 90°$ both the vortex formation and separation regime must take place. Thus LEV formation and flow separation would need to take place significantly earlier. One option to achieve this, other than decreasing the chord length significantly, as would be suggested by the previous analysis, would be to change the mean angle of attack from $\alpha_0 = 0$ to some positive value. This change would encourage earlier flow separation but may increase overall torque by negating the vortex capture effect.

Chapter 7

Conclusion

Two-dimensional time-resolved particle image velocimetry measurements were performed on airfoils undergoing various unsteady motions corresponding to the flow over vertical axis wind turbine blades. Experiments were performed on a NACA-0018 airfoil in a water channel at a Reynolds number of 10^5 and reduced frequency $k = 0.12$ corresponding to the parameters of a typical full-scale VAWT at tip speed ratio $\eta = 2$. The airfoil motions studied included pitching between $-30^\circ \leq \alpha \leq 30^\circ$ to match the angle of attack variation, surging at $\pm 45\%$ of the freestream velocity to match the velocity variation, and a combined pitch/surge motion implemented with the same phase relationship as dictated by the airfoil motion in the turbine. In order to implement these motions independently, the airfoil motion was removed from the rotating frame of the VAWT, allowing for independent time-resolved measurements at the expense of a change of reference frame and the loss of the Coriolis force.

Critical structure and physical phenomena that give rise to the dynamic stall behavior inherent due to the airfoil motion were identified using multiple mathematical techniques. Low-order representations of the complex flow fields were developed using the dynamic mode decomposition to highlight flow behaviour associated with the driving frequency of the airfoil motion. Such models provided insight into the physics inherent in the flow fields studied. Leading edge vortex structure was identified and tracked in time, and its effect on the flow structure was analyzed. Finally, DMD was used to investigate the frequency content of the flow and to develop an understanding of the forcing frequencies inherent in the flow over VAWT blades.

7.1 Summary and major findings

The flow over the phase-averaged sinusoidal pitching and surging airfoil motion, used as a surrogate for the flow over a VAWT blade, was shown to exhibit full dynamic stall behaviour including complete leading edge separation prior to the maximum angle of attack but after the static stall angle, as well as gradual reattachment, from the leading edge to trailing edge. This flow evolution shared similar features to measurements made at limited angles of attack on a rotating turbine by Simão Ferreira et al. (2009), including the shedding of a leading and trailing edge vortex prior to full stall. Furthermore, the flow was found to be in good qualitative agreement with the computations of Tsai and Colonius (2014), indicating the validity of the pitch/surge approximation. Due to the periodic motion of the airfoil, the dynamic mode decomposition was appropriate to develop a low-order model utilizing modes with fixed temporal frequencies. Excellent qualitative agreement between the full, time-resolved, velocity field was achieved with a model utilizing only five modes, including a time-constant flow and modes at the first two harmonics of the pitch/surge frequency. In addition to qualitatively matching the shape of the vortex and shear activity, this model was also shown to capture the circulation within the leading edge vortex that is a dominant component of dynamic stall.

Analyzing the structure of each mode associated with each frequency provided insight into the physics responsible for the dynamic stall. The spatial mode associated with the pitch/surge frequency was shown to account for the velocity variation due to surge, as well as to consist of a vortical structure that convects downstream along the airfoil causing separation. The mode corresponding to twice the pitch/surge frequency included a similar vortex with an opposite sense of rotation on pitch down that led the reattachment process. The phase relationship between these primary and secondary separation modes was shown to account for both the hysteresis, inherent in dynamic stall, and the differences between the pressure and suction sides of the airfoil. The applicability of such a simple model highlighted that the basic physics of dynamic separation and reattachment were inherently linked to a timescale dependent on the frequency of the motion.

The leading edge vortex was identified in the phase-averaged flow during pitch up and the evolution of separation was broken down into several regimes based on the dynamics of the LEV. Initially, as the airfoil passed $\alpha_+ = 0°$, no true LEV was present, but the flow rotated around the contour of the airfoil similar to a steady airfoil. As the airfoil pitched up to higher angles of attack $\alpha_+ \sim 15°$, the dynamic behavior took over and a true vortex appeared at the leading edge. This vortex grew linearly in strength until it was seen to shed from the leading edge, convecting downstream until it

reached the trailing edge and full stall took place. The LEV was shown to develop for approximately four convection times before shedding from the leading edge. This corresponds with the optimal formation time of Gharib et al. (1998) and Dabiri (2009) and co-workers, and suggests that the timescale of vortex formation dominates the LEV separation and subsequent stall that occurs before maximum angle of attack.

Prior to flow separation, analysis of the instantaneous pitch/surge measurements indicated periodic shedding that did not appear in phase-averaged results, and as such is not directly coupled to the airfoil motion. This vortex shedding was identified by performing a spectral decomposition on the full instantaneous flow field with DMD. This periodic shedding was shown to occur at a frequency corresponding to the Strouhal shedding frequency, based on the airfoil thickness and instantaneous airfoil relative freestream velocity. The examination of frequency bands not including the pitch/surge frequency indicated similar vortex strength in both the clockwise and counter-clockwise directions. In the full dataset, however, counter-clockwise vortices were shown to be significantly stronger. Inclusion of the pitch/surge frequency accounted for this discrepancy, suggesting that the rotation of the airfoil caused a decrease in clockwise vorticity but otherwise had little effect on the vortex shedding. Periodic vortex shedding was shown to continue until the LEV shed from the leading edge and the Strouhal scaling was no longer valid due to flow separation.

The phase-averaged flow over the pitching-only wing was shown to develop similarly to the pitch/surge case, exhibiting dynamic stall and reattachment. Separation in the pitch-only case, however, was shown to occur at a lower angle of attack, somewhat earlier in the pitch cycle. Analysis of the leading edge vortex demonstrated that, in contrast to the pitch/surge case, a small leading edge vortex is present beginning at $\alpha_+ = 0°$, indicating that dynamic behavior dominates somewhat earlier. Furthermore, this vortex grows to be stronger before its eventual shedding prior to full-scale flow separation. For the surging-only motion at a fixed angle of attack of $\alpha = 15°$, forward acceleration was shown to have a destabilizing effect, causing the separation point to move toward the leading edge, while backward acceleration caused the flow to attach further along the wing. This stabilization effect during deceleration may account for the differences between pitching and pitch/surge flow, since the LEV is limited and the flow is stabilized in the combined case while the airfoil is decelerating.

A similar model to the combined pitch/surge flow was developed for the pitch-only case; however, an extra mode pair at three-times the pitch frequency was required to model the dynamic separation and reattachment behavior, as opposed to five as in the pitch/surge case. The mode pair at the

pitch frequency was similar to the primary separation mode for the pitch/surge case, including a vortex that convects downstream and leads to separation approximately two degrees earlier than the combined case, corresponding to the earlier separation. The phase relationship between the mode pairs at two and three times the pitch frequency induced a phase lag on the combined mode that allowed the three-frequency model to capture the reattachment that occurred too early in the two-frequency, five mode model. The structure of this composite mode was similar to the secondary separation mode for the pitch/surge flow and included a vortex that convected downstream leading reattachment. As such, the physics behind both the pitch and pitch/surge flows can be modeled using the same mechanisms; however, an additional frequency is required for the pitch-only flow to accurately reproduce the time history.

The results from the pitch/surge experiments were extrapolated into the VAWT frame and compared to simulations of Tsai and Colonius (2014). The flow was shown to develop similarly with and without Coriolis forces, especially near the airfoil. After separation, however, the shed LEV convected differently, in both reference frames. The location of LEV shedding and subsequent separation results in the LEV remaining very close to the airfoil in the turbine reference frame. This corresponded well with the vortex-capture effect developed by Tsai and Colonius (2014).

In this study flow phenomena on the blades of vertical axis wind turbines were investigated by measureing the flow over a pitching and surging wing in a water channel. Using this approximation time resolved measurements could be made at full scale Reynolds numbers, however some limitations exist in applying these results directly to a VAWT in the field. The effect of the rotating frame of reference and the Coriolis effect was addressed in Chapter 6 and as well as the results of the acceleration of the trailing edge due to the pitch motion. In addition turbines in the field experience variation in incoming velocity U_∞ and have somewhat varying tip speed ratios, implying that the exact angle of attack variation explored here, will not seen exactly. Furthermore the freestream will exhibit some shear in the spanwise direction, due to the atmospheric boundary layer incoming to the turbine, which may result in spanwise flow. This incoming boundary layer will also be fully turbulent, resulting in random variation in velocity and angle of attack along the span of the blade. Finally this research does not address the startup process of the VAWT, which requires the turbine to accelerate from tip speed ratio $\eta = 0$ to the operating tip speed ratio $\eta \sim 2$, nor the interaction between multiple blades in the turbine and the wake discussed by Araya and Dabiri (2015).

7.2 Future work

This thesis provides the basic understanding of the flow field on a single blade of a VAWT at $\eta = 2$, while the previous Chapter suggests changes that could be applied to improve turbine performance. Further investigation into the parameter space suggested would be of interest. Adapting the airfoil geometry, or the tip speed ratio, has opposite effects on the reduced frequency k. As such, developing a design manifold, measuring the beginning of LEV development as well as the frequency-dependent separation point, could provide the design criteria necessary to optimize the location of LEV shedding, either to increase lift with optimal vortex formation, or to reduce the negative effects of vortex capture on the receding blades. Furthermore, adjusting the test motion to the exact VAWT motion rather than the sinusoidal approximation of the present study would provide insight into the effect of the skewed sinusoidal airfoil motion that results in a slower overall pitch up.

Of further interest to both the VAWT and the general unsteady aerodynamics community would be to extend the simple model developed with DMD for the combined pitch/surge motion in Chapter 3 and for pitch in Chapter 5. In both of these cases a primary and secondary separation mode were identified; however, a second frequency was necessary in the pitch-only model to adjust the phase relationship between the modes that account for separation and reattachment, respectively. Applying this model to different motions and different frequencies could provide insight into the parameter space where it is inherently applicable. Furthermore, extending the model beyond fixed-frequency sinusoidal motions to more general periodic motions (such as that experienced by a VAWT blade) would be of interest but may require more advanced techniques than a simple dynamic mode decomposition that inherently finds modes with a Fourier basis.

The next step of interest is to construct full rotating turbines that are capable of free-spinning to generate power. While a blade motion profile may be developed that utilizes optimal vortex growth and optimizes the unsteady aerodynamics, this profile will require a specific tip speed ratio. Therefore, to use such a turbine it must be insured that it is capable of reaching and maintaining that rotational velocity. More importantly, this motion must be coupled to an electrical generator that produces power in such a range. Additionally, the full turbine will incorporate the effects of the Coriolis force and turbine structure necessary to hold the blades, not considered in these simple models. Additionally, to design an effective turbine, the efficiency at non-design conditions must be considered, and as such, blade motions that are insensitive to changes in reduced frequency will be necessary, such that the final VAWT will produce significant power over a range of incoming wind speed.

The interaction of multiple blades in the turbine should be investigated. The most obvious effects of interest are the interaction of vortices shed from the upstream blades on the downstream blades. While the freestream velocity is so low in the downstream region that power production is negligible (Islam et al., 2007), the interaction between shed vortices and downstream blades could induce loading with further frequency content onto the turbine structure. These frequencies must be understood to design a robust turbine.

Additionally, the interaction between leading and following blades is of both scientific and engineering interest. As the solidity of the turbine, defined as the percentage of swept area taken up by blades, increases, potentially due to increased chord length (section 6.4), or by including increased number of blades, the two blades may affect each other. If the following blade lies in the wake of the upstream blade, it will experience decreased freestream velocity, resulting in decreased lift. Conversely, with correct orientation it is possible that constructive interference could take place, increasing overall lift or driving power, as is the case with leading edge slats on aircraft, or the interaction of multiple sails on many sail boats.

Finally, further investigation of the three-dimensional effects on VAWT blades would be of interest, such as the effect of stall cells suggested by the results in Chapter 2. Additionally, the effect of non-straight bladed helical turbines could be measured. Spanwise flow that may be induced by such a design has been shown (Garmann et al., 2013) to stabilize the LEV on rotating blades and, as such, these turbines may be able to maintain LEV attachment somewhat longer. Furthermore, since the angle of attack will not be constant along the blade span in a helical turbine, the extreme loss in lift at LEV separation (Jones and Babinsky, 2010) that causes unsteady loading on the turbine may be less intense as the separation will occur gradually over the span of the blade.

The results developed in this thesis have identified the primary physical mechanisms responsible for dynamic stall on VAWT blades and detailed the interaction between the multiple timescales that affect the flow. The overall dynamics of the flow are, at their core, determined by a phase relationship between these physical phenomena, as well as the identified modes that give rise to the separation behavior. Analysis of the pitching and surging motion independently found that the surge motion added a phase delay into the dynamic-stall modes, delaying separation on the airfoil. Manipulation of the phase relationships between timescales and identified modes provides an opportunity to improve the performance of VAWTs. Additionally, the forcing frequencies inherent in this flow are identified, providing design requirements to build more robust turbines. Significant work remains in order to extend the physical understanding provided here to even more complex

problems. Furthermore, the design suggestions derived from this work must be tested to develop and produce more effective and robust vertical axis wind turbines.

Bibliography

American Wind Energy Association (2013). U . S . Wind Industry Market Update 2012. Technical Report May, American Wind Energy Association. 1

Araya, D. B. and Dabiri, J. O. (2015). A comparison of wake measurements in motor-driven and flow-driven turbine experiments. *Exp. Fluids*, 56(7):150. ISSN 0723-4864. doi:10.1007/s00348-015-2022-7. 5, 97, 112

Baik, Y. S. and Bernal, L. P. (2012). Experimental study of pitching and plunging airfoils at low Reynolds numbers. *Exp. Fluids*, 53(6):1979–1992. ISSN 0723-4864. doi:10.1007/s00348-012-1401-6. 8

Baik, Y. S., Bernal, L. P., Granlund, K., and Ol, M. V. (2012). Unsteady force generation and vortex dynamics of pitching and plunging aerofoils. *J. Fluid Mech.*, 709:37–68. ISSN 0022-1120. doi:10.1017/jfm.2012.318. 7, 11, 54

Bearman, P. (1967). On vortex street wakes. *J. Fluid Mech.*, 28:625–641. 11

Bearman, P. W. (1984). Vortex shedding from oscillating bluff bodies. *Annu. Rev. Fluid Mech*, 16:195–222. 11

Beckwith, R. M. H. and Babinsky, H. (2009). Impulsively started flat plate flow. *J. Aircr.*, 46(6):2186–2189. ISSN 0021-8669. doi:10.2514/1.46382. 10

Beri, H. and Yao, Y. (2011). Effect of camber airfoil on self starting of vertical axis wind turbine. *Environ. Sci.and Tech.*, 4(9). 5

Blevins, R. (1974). *Flow Induced Vibration of Bluff Structures*. Ph.D. thesis, California Institute of Technology. 11

Bobba, K. M. (2004). *Robust Flow Stability : Theory, Computations and Experiments in Near Wall Turbulence*. Ph.D. thesis, California Institute of Technolgoy. 14

Brent, S. (2009). AWEA standard update. *2009 Small Wind Turbine Testing Workshop*. National Wind Technology Center (NWTC). 16

Buchner, A. J., Soria, J., and Smits, A. J. (2015). Circulation production and shedding from vertical axis wind turbine blades undergoing dynamic stall. *Int. Symp. Turbul. Shear Flow Phenom.* Melbourne, AUS. 9

Carr, L., McAlister, K., and McCroskey, W. (1977). Analysis of the development of dynamic stall based on oscillating airfoil experiments. Technical Report January, NASA. 7, 59, 72, 100

Carr, L. W. (1988). Progress in analysis and prediction of dynamic stall. *J. Aircr.*, 25(1):6–17. 6

Chakraborty, P., Balachandar, S., and Adrian, R. J. (2005). On the relationships between local vortex identification schemes. *J. Fluid Mech.*, 535:189–214. ISSN 0022-1120. doi: 10.1017/S0022112005004726. 25

Chen, K. K., Tu, J. H., and Rowley, C. W. (2012). Variants of Dynamic Mode Decomposition: Boundary Condition, Koopman, and Fourier Analyses. *J. Nonlinear Sci.*, 22(6):887–915. ISSN 0938-8974. doi:10.1007/s00332-012-9130-9. 27

Choi, J., Colonius, T., and Williams, D. R. (2015). Surging and plunging oscillations of an airfoil at low Reynolds number. *J. Fluid Mech.*, 763:237–253. ISSN 0022-1120. doi:10.1017/jfm.2014.674. 8, 54

Colonius, T. and Taira, K. (2008). A fast immersed boundary method using a nullspace approach and multi-domain far-field boundary conditions. *Comput. Methods Appl. Mech. Eng.*, 197(25-28):2131–2146. ISSN 00457825. 9

Cossé, J. T. (2014). *On the Behavior of Pliable Plate Dynamics in Wind : Application to Vertical Axis Wind Turbines*. Ph.D. thesis, California Institute of Technology. 2

Dabiri, J. O. (2009). Optimal Vortex Formation as a Unifying Principle in Biological Propulsion. *Annu. Rev. Fluid Mech.*, 41(1):17–33. ISSN 0066-4189. doi:10.1146/annurev.fluid.010908.165232. 10, 11, 69, 72, 111

Dabiri, J. O. (2011). Potential order-of-magnitude enhancement of wind farm power density via counter-rotating vertical-axis wind turbine arrays. *J. Renew. Sustain. Energy*, 3(4). ISSN 19417012. doi:10.1063/1.3608170. 1, 16

Dabiri, J. O. and Gharib, M. (2005). Starting flow through nozzles with temporally variable exit diameter. *J. Fluid Mech.*, 538:111. ISSN 0022-1120. doi:10.1017/S002211200500515X. 10, 60, 79

Dabiri, J. O., Greer, J. R., Koseff, J. R., Moin, P., and Peng, J. (2015). A new approach to wind energy: Opportunities and challenges. *AIP Conf. Proc.*, volume 57, pages 51–57. ISBN 9780735412941. doi:10.1063/1.4916168. 2

Dunne, R. and McKeon, B. J. (2014). Dynamic separation on a pitching and surging airfoil as a model for flow over vertical axis wind turbine blades. *32nd AIAA Appl. Aerodyn. Conf.*, # 3142. Atlanta, GA. doi:10.2514/6.2014-3142. 13

Dunne, R. and McKeon, B. J. (2015a). A study of separation on airfoils undergoing combined pitch, surge and combined motions. *33rd AIAA Appl. Aerodyn. Conf.*, # 2882. Dallas, Tx. doi: 10.2514/6.2015-2882. 13, 74

Dunne, R. and McKeon, B. J. (2015b). Dynamic stall on a pitching and surging airfoil. *Exp. Fluids*, 56(8):157. ISSN 0723-4864. doi:10.1007/s00348-015-2028-1. 13, 38, 95

Dunne, R., Tsai, H. C., Colonius, T., and Mckeon, B. J. (2015). Leading edge vortex development on pitching and surging airfoils : A study of vertical axis wind turbines. *Int. Conf. Wakes Jets Separated Flows*. Stockholm, Sweden. 13, 95

Environmental Protection Agency (2015). Inventory of U . S . Greenhouse Gas Emissions and Sinks:. Technical report, U.S. Envrionmental Protection Agency. 1

Garmann, D. J., Visbal, M. R., and Orkwis, P. D. (2013). Investigation of aspect ratio and dynamic effects due to rotation for a revolving wing using high-fidelity simulation. *51st AIAA Aerosp. Sci. Meet.*, # 86. Grapevine, TX. doi:10.2514/6.2013-86. 114

Gerakopulos, R. (2010). Aerodynamic characterization of a NACA 0018 airfoil at low Reynolds numbers. *40th AIAA Fluid Dyn. Conf.*, # 4629. Chicago, IL. doi:10.2514/6.2010-4629. 15

Gharib, M., Rambod, E., and Shariff, K. (1998). A universal time scale for vortex ring formation. *J. Fluid Mech.*, 360:121–140. ISSN 00221120. doi:10.1017/S0022112097008410. 10, 60, 69, 72, 79, 111

Graftieaux, L., Michard, M., and Grosjean, N. (2001). Combining PIV, POD and vortex identification algorithms for the study of unsteady turbulent swirling flows. *Meas. Sci. Technol.*, 12(9):1422–1429. doi:10.1088/0957-0233/12/9/307. 25, 26, 46, 91

Greenblatt, D., Harav, A. B., and Mueller-Vahl, H. (2013). Mechanism of Dynamic Stall Control on a Vertical Axis Wind Turbine. *51st AIAA Aerosp. Sci. Meet.*, # 851. doi:10.2514/6.2013-851. 2, 6, 10

Greenblatt, D., Nishri, B., Darabi, A., and Wygnanski, I. (2001). Dynamic stall control by periodic excitation part 2: mechanisms. *J. Aircraft*, 38(3). 8

Greenblatt, D. and Wygnanski, I. (2001). Dynamic stall control by periodic excitation part 1: Naca 0015 parametric study. *J. Aircraft*, 38(3). 6, 8

Hau, E. (2013). *Wind Turbines: Fundamentals, Technologies, Application, Economics*. Springer. viii, 1, 2, 4, 5

Heine, B., Mulleners, K., Joubert, G., and Raffel, M. (2013). Dynamic Stall Control by Passive Disturbance Generators. *AIAA J.*, 51(9):2086–2097. ISSN 0001-1452. doi:10.2514/1.J051525. 8

Hemati, M. S. and Rowley, C. W. (2015). De-biasing the dynamic mode decomposition for applied Koopman spectral analysis. *arXiv:1502.03854*. 27, 44

Islam, M., Ting, D. S.-K., and Fartaj, A. (2007). Desirable airfoil features for smaller-capacity straight-bladed VAWT. *Wind Eng.*, 31(3):165–196. 2, 4, 15, 39, 104, 114

Joe, W., Colonius, T., and MacMynowski, D. (2011). Feedback control of vortex shedding from an inclined flat plate. *Theor. Comput. Fluid Dyn.*, 25(1-4):221–232. ISSN 0935-4964. doi:10.1007/s00162-010-0204-8. 11

Jones, A. R. and Babinsky, H. (2010). Unsteady lift generation on rotating wings at low Reynolds number. *J. Aircraft*, 47(3):1013–1021. 10, 100, 114

Jones, a. R. and Babinsky, H. (2011). Reynolds number effects on leading edge vortex development on a waving wing. *Exp. Fluids*, 51(1):197–210. ISSN 0723-4864. doi:10.1007/s00348-010-1037-3. 10

Jung, Y. and Park, S. (2005). Vortex-shedding characteristics in the wake of an oscillating airfoil at low Reynolds number. *J. Fluids Struct.*, 20(3):451–464. ISSN 08899746. doi:10.1016/j.jfluidstructs.2004.11.002. 12, 68

Kang, C.-k., Aono, H., Sik Baik, Y., Bernal, L. P., and Shyy, W. (2013). Fluid dynamics of pitching and plunging flat plate at intermediate Reynolds numbers. *AIAA J.*, 51(2):315–329. ISSN 0001-1452. doi:10.2514/1.J051593. 8

Karim, M. A. and Acharya, M. (1994). Suppression of dynamic-stall vortices of pitching airfoils by leading-edge suction. *AIAA Journal*, 32(8). 9

Kinzel, M., Mulligan, Q., and Dabiri, J. O. (2012). Energy exchange in an array of vertical-axis wind turbines. *J. Turb.*, 13(38):1–13. 2, 4, 16

Koochesfahani, M. M. (1989). Vortical patterns in the wake of an oscillating airfoil. *AIAA J.*, 27(9):1200–1205. 11, 12, 68

Lehew, J. A. (2012). *Spatio-temporal analysis of the turbulent boundary layer and an investigation of the effects of periodic disturbances*. Ph.D. thesis, California Institute of Technology. viii, 14, 15, 21

MacKay, D. (2009). *Sustainable Energy–without the Hot Air*. Without the Hot Air Series. UIT. ISBN 9780954452933. 1

Milano, M. and Gharib, M. (2005). Uncovering the physics of flapping flat plates with artificial evolution. *J. Fluid Mech.*, 534:403–409. ISSN 0022-1120. doi:10.1017/S0022112005004842. 11

Mulleners, K. and Raffel, M. (2012). The onset of dynamic stall revisited. *Exp. Fluids*, 52(3):779–793. ISSN 0723-4864. doi:10.1007/s00348-011-1118-y. 7

Mulleners, K. and Raffel, M. (2013). Dynamic Stall Development. *Exp. Fluids*, 54(3):353–375. doi:10.1007/s00348-014-1669-9. 7

Müller-Vahl, H. F., Strangfeld, C., Nayeri, C. N., Paschereit, C. O., and Greenblatt, D. (2015). Control of Thick Airfoil, Deep Dynamic Stall Using Steady Blowing. *AIAA J.*, 53(2):277–295. ISSN 0001-1452. doi:10.2514/1.J053090. 9, 41

Panda, J. and Zaman, K. B. M. Q. (1994). Experimental investigation of the flow field of an oscillating airfoil and estimation of lift from wake surveys. *J. Fluid Mech.*, 265:65–95. ISSN 0022-1120. doi:10.1017/S0022112094000765. 8

Prangemeier, T., Rival, D., and Tropea, C. (2010). The manipulation of trailing-edge vortices for an airfoil in plunging motion. *J. Fluids Struct.*, 26(2):193–204. ISSN 08899746. doi:10.1016/j.jfluidstructs.2009.10.003. 8

Ringuette, M. J., Milano, M., and Gharib, M. (2007). Role of the tip vortex in the force generation of low-aspect-ratio normal flat plates. *J. Fluid Mech.*, 581:453. ISSN 0022-1120. doi:10.1017/S0022112007005976. 11

Rival, D., Prangemeier, T., and Tropea, C. (2009). The influence of airfoil kinematics on the formation of leading-edge vortices in bio-inspired flight. *Exp. Fluids*, 46(5):823–833. ISSN 0723-4864. doi:10.1007/s00348-008-0586-1. 6, 8, 10, 11, 54, 59, 61, 73, 107

Roshko, A. (1952). *On The Development of Turbulent Wakes from Vortex Streets*. Ph.D. thesis, California Institute of Technology. 11

Roshko, A. (1961). Experiments on the flow past a circular cylinder at very high Reynolds number. *J. Fluid Mech.*, 10(03):345–356. 11

Rowley, C. W., Mezić, I., Bagheri, S., Schlatter, P., and Henningson, D. S. (2009). Spectral analysis of nonlinear flows. *J. Fluid Mech.*, 641:115–127. ISSN 0022-1120. doi:10.1017/S0022112009992059. 27

Schmid, P. J. (2010). Dynamic mode decomposition of numerical and experimental data. *J. Fluid Mech.*, 656:5–28. ISSN 0022-1120. doi:10.1017/S0022112010001217. 27, 38

Simão Ferreira, C., Bijl, H., van Bussel, G., and van Kuik, G. (2007a). Simulating dynamic stall in a 2D VAWT: Modeling strategy, verification and validation with particicle image velocimetry data. *J. Phys. Conf. Ser.*, 73. 9, 15

Simão Ferreira, C., van Bussel, G., Scarano, F., and van Kuik, G. (2007b). 2D PIV visualization of dynamic stall on a vertical axis wind turbine. *45th AIAA Aerosp. Sci. Meet.*, # 1336. doi: 10.2514/6.2007-1366. 9, 15

Simão Ferreira, C., van Kuik, G., van Bussel, G., and Scarano, F. (2009). Visualization by PIV of dynamic stall on a vertical axis wind turbine. *Exp. Fluids*, 46(1):97–108. ISSN 0723-4864. 9, 15, 42, 60, 110

Simão Ferreira, C. J., A, V. Z., Bijl, H., van Bussel, G., and van Kuik, G. (2010). Simulating dynamic stall in a two-dimensional vertical axis wind turbine: verification and validation with particle image velocimetry data. *Wind Energ.*, 13:1–17. 9, 15

Tsai, H.-C. and Colonius, T. (2014). Coriolis effect on dynamic stall in vertical axis wind turbine at moderate Reynolds number. *32nd AIAA Appl. Aerodyn. Conf.*, # 3140. Atlanta, GA. doi: 10.2514/6.2014-3140. xiv, xv, 3, 9, 13, 25, 95, 96, 97, 100, 101, 102, 103, 106, 108, 110, 112

Untaroiu, A., Wood, H. G., Raval, A., and Allaire, P. E. (2011). Boundary layer control for a vertical axis wind turbine using a secondary-flow path system. *Proceedings of ASME Turbo Expo*. 10

US Energy Information Administration (2015). Monthly Energy Review. Technical report, Energy Information Administration. 1

Vanek, F. and Albright, L. (2008). *Energy Systems Engineering: Evaluation and Implementation: Evaluation and Implementation*. McGraw-Hill Education. ISBN 9780071640947. 1

Vestas (2015). V126-3.3/3.45 MW at a glance. http://www.vestas.com. Accessed: 2015-05-18. 1

Weihs, D. and Katz, J. (1983). Cellular patterns in poststall flow over unswept wings. *AIAA J.*, 21(12):1757–1759. 31

Whittlesey, R. W., Liska, S., and Dabiri, J. O. (2010). Fish schooling as a basis for vertical axis wind turbine farm design. *Bioinspir. Biomim.*, 5(3). ISSN 1748-3190. doi:10.1088/1748-3182/5/3/035005. 1

Windspire (2013). Standard wind unit 1.2kw. Accessed 11/2013. 3, 4